SENSORLESS DIRECT FIELD ORIENTED CONTROL OF INDUCTION MACHINE BY FLUX AND SPEED ESTIMATION USING MODEL REFERENCE ADAPTIVE SYSTEM

A THESIS SUBMITTED TO
THE GRADUATE SCHOOL OF NATURAL AND APPLIED SCIENCES
OF
THE MIDDLE EAST TECHNICAL UNIVERSITY

BY

GÜNAY ŞİMŞEK

IN PARTIAL FULLFILMENT OF THE REQUIREMENTS FOR THE DEGREE OF
MASTER OF SCIENCE
IN
THE DEPARTMENT OF ELECTRICAL AND ELECTRONICS ENGINEERING

APRIL-2004

Approval of the Graduate School of Natural and Applied Sciences.

_____

Prof. Dr. Canan ÖZGEN
Director

I certify that this thesis satisfies all the requirements as a thesis for the degree of Master of Science.

_____

Prof. Dr. Mübeccel DEMİREKLER
Chairman of the Department

This is to certify that we have read this thesis and that in our opinion it is fully adequate, in scope and quality, as a thesis for the degree of Master of Science.

_____

Prof. Dr. Aydın ERSAK
Supervisor

Examining Committee Members

Prof. Dr. Yıldırım ÜÇTUĞ _____

Prof. Dr. Aydın ERSAK _____

Prof. Dr. Muammer ERMİŞ _____

Assoc. Prof. Dr.Işık ÇADIRCI _____

Asst. Prof. Dr. Ahmet M. HAVA _____

ABSTRACT

SENSORLESS DIRECT FIELD ORIENTED CONTROL OF INDUCTION MACHINE BY FLUX AND SPEED ESTIMATORS USING MODEL REFERENCE ADAPTIVE SYSTEM

Şimşek, Günay
M. Sc. Department of Electrical and Electronics Engineering
Supervisor : Prof. Dr. Aydın Ersak

April, 2004

This work focuses on an observer design which will estimate flux-linkage and speed for induction motors in its entire speed control range. The theoretical base of the algorithm is explained in detail and its both open-loop, and closed-loop performance is tested with experiments, measuring only stator current and voltage.

Theoretically, the field-oriented control for the induction motor drive can be mainly categorized into two types; indirect and direct field oriented. The field to be oriented may be rotor, stator, or airgap flux-linkage. In the indirect field-oriented control, the slip estimation based on the measured or estimated rotor speed is required in order to compute the synchronous speed. There is no need for the flux estimation in such a system. For the direct field oriented case the synchronous speed is computed with the aid of a flux estimator. In DFO, the synchronous speed is

computed from the ratio of dq-axes fluxes. With the combination of a flux estimator and an open-loop speed estimator one can observe stator-rotor fluxes, rotor-flux angle and rotor speed. In this study, the direct (rotor) flux oriented control system with flux and-open-loop speed estimators is described and tested in real-time with the Evaluation Module named TMS320LF21407 and the Embedded Target software named Vissim from Visual Solutions Company.

Keywords : Sensorless direct field oriented, flux estimation, speed estimation.

ÖZ

MODELE DAYANAN UYARLAMALI YÖNTEM KULLANARAK AKI VE HIZ KESTİRİMİYLE DUYAÇSIZ DOĞRUDAN ALAN YÖNLENDİRMELİ ENDÜKSİYON MOTOR DENETİMİ

Şimşek, Günay
Yüksek Lisans, Elektrik ve Elektronik Mühendsliği Bölümü
Tez Danışmanı : Prof. Dr. Aydın Ersak

Nisan, 2004

Bu çalışmada endüksiyon motorunun tüm çalışma hızı aralıklarındaki akı ve hızının tahmin edilemesine odaklaşılmıştır. Sunulan yöntemin tüm kuramsal içeriği ayrıntılı olarak anlatılmış ve bu yöntemin açık ve kapalı döngü başarımları sadece stator akım ve gerilimlerinin ölçülmesi ile test edilmiştir.

Teorik olarak alan yönlendirmeli endüksiyon motor denetimi iki ana grupta incelenir; dolaylı ve doğrudan alan yönlendirmeli denetim. Yönlendirilecek alan rotor, stator veya motor havaboşluğu akısı olabilir. Dolaylı alan yönlendirmeli denetimde senkron hızın hesaplanması için rotor hızının ölçülmesine veya tahmin edilmesine gerek duyulmaktadır. Bu denetimde akı tahmin edilmesi söz konusu değildir. Doğrudan alan yönlendirmeli denetimde akı tahmin yöntemi ile senkron hız hesaplanmaktadır. Doğrudan alan yönlendirmeli denetimde dq eksenlerindeki akıların oranından senkron hız hesaplanmaktadır. Akı tahmin ve açık-döngü hız

tahmin yöntemleri yardımıyla stator ve rotor akıları, rotor akı açısı ve rotor hızı gözlenebilmektedir. Bu çalışmada, doğrudan alan (rotor) yönlendirmeli denetimi, akı ve açık-döngü hız tahmin methodları kullanılarak anlatılmış ve gerçek zamanlı olarak da TMS320LF2407 deneme kartı ve Vissim yazılımı kullanılarak test edilmiştir.

Anahtar Kelimeler: Sensörsüz alan yönlendirmeli denetim, akı tahmin methodu, hız tahmin methodu.

ACKNOWLEDGMENTS

I would like to express my sincere gratitude to my supervisor Prof. Dr. Aydın Ersak for his encouragement and guidance throughout the study. I also thank him not only for his technical assists but for his friendship in due course of development of the thesis.

I would also like to thank everybody at the Department of Electronic Hardware in Aselsan for helping me with all kinds of practical problems.

Mr. Bilal Akın made significant contributions from the beginning of the study by his technical advice, and his support always continued up to now. Mr. Eray Özçelik helped during the experimental stage of this work. To my both dear friends I say thank you.

The last but not least acknowledgment is to my wife, who was willing to give up many other activities so that the study could be carried out. Her support will always be appreciated.

TABLE OF CONTENTS

LIST OF FIGURES

LIST OF SYMBOLS

SYMBOL

e_{md}	back emf d axis component
e_{mq}	back emf q axis component
i^{e}_{ds}	d axis stator current in synchronous frame
i^{e}_{qs}	q axis stator current in synchronous frame
i^{s}_{ds}	d axis stator current in stationary frame
i^{s}_{qs}	q axis stator current in stationary frame
i_{ar}	Phase-a rotor current
i_{br}	Phase-b rotor current
i_{cr}	Phase-c rotor current
i_{as}	Phase-a stator current
i_{bs}	Phase-b stator current
i_{cs}	Phase-c stator current
L_m	Magnetizing inductance
L_{ls}	Stator leakage inductance
L_{lr}	Rotor leakage inductance
L_s	Stator self inductance
L_r	Rotor self inductance
R_s	Stator resistance
R_r	Referred rotor resistance
q_{md}	reactive power d axis component
q_{mq}	reactive power q axis component
T_{em}	Electromechanical torque
T_r	Rotor time-constant
V_{as}	Phase-a stator voltage
V_{bs}	Phase-b stator voltage
V_{cs}	Phase-c stator voltage

V_{ar} Phase-a rotor voltage

V_{br} Phase-b rotor voltage

V_{cr} Phase-c rotor voltage

V^{s}_{ds} d axis stator voltage in stationary frame

V^{s}_{qs} q axis stator voltage in stationary frame

V^{e}_{ds} d axis stator voltage in synchronous frame

V^{e}_{qs} q axis stator voltage in synchronous frame

V_{dc} Dc-link voltage

X_{m} Stator magnetizing reactance

X_{ls} Stator leakage reactance

X_{lr} Rotor leakage reactance

X_{s} Stator self reactance

X_{r} Rotor self reactance

w_{e} Angular synchronous speed

w_{r} Angular rotor speed

w_{sl} Angular slip speed

θ_{e} Angle between the synchronous frame and the stationary frame

θ_{d} Angle between the synchronous frame and the stationary frame when d axis is leading

θ_{q} Angle between the synchronous frame and the stationary frame when q axis is leading

$\theta_{\psi r}$ Rotor flux angle

ψ^{s}_{ds} d axis stator flux in stationary frame

ψ^{s}_{qs} q axis stator flux in stationary frame

ψ^{e}_{ds} d axis stator flux in synchronous frame

ψ^{e}_{qs} q axis stator flux in synchronous frame

ψ_{as} Phase-a stator flux

ψ_{bs} Phase-b stator flux

ψ_{cs} Phase-c stator flux

ψ_{ar} Phase-a rotor flux

ψ_{br} Phase-b rotor flux

ψ_{cr} Phase-c rotor flux

1 INTRODUCTION

Induction machines provide a definite advantage with respect to cost and reliability when compared to other motors. It has rugged structure and insensitive to dusty and explosive environment and they do not require periodic maintenance. Besides these it is cheaper than the other types of electrical motors. Although the induction motor has many advantages, for many years it has been controlled by means of scalar V/f method or it has been plugged directly into the network. It is, however, difficult to control due to its complex mathematical model, its non-linear behavior during saturation effect and the electrical parameter oscillation, which depends on, the physical influence of the temperature. During the last decade technological improvements have enabled the development of effective AC drive control with ever lower power dissipation hardware and ever more accurate control structures. Therefore, the use of induction machines in industrial applications is becoming more practical, thanks to both improved field-oriented control techniques and improvements in the control strategies, power semiconductors, and digital signal processors.

The field-oriented control, FOC method takes into consideration both successive steady-states and real mathematical equations that describe the motor itself. The control thus obtained has a better dynamic for torque variations in a wider speed range. FOC approach needs more computational power than a standard V/f control scheme. This need can be overcome by the use of Digital Signal processors. As a result FOC provides the advantages of full motor torque capability at low speed, better dynamic behaviour, higher efficiency for each operation point in a wide speed range, decoupled control of torque and flux, short term overload capability, and four quadrant operation.

All those properties are obtained with vector controlled induction machines. The drawback of FOC is that the rotor speed of the induction machine must be measured through a speed sensor of some kind, for example a resolver or an incremental encoder. Due to the cost of these sensors recent trend is towards the use of sensorless algorithms in FOC. Estimated speed instead of the measured one essentially reduces the cost and the complexity of the drive system. The term sensorless refers to the absence of a speed sensor on the motor shaft, but the motor currents and the voltages must still be measured. The vector control method requires also estimation of the flux linkage of the machine whether the speed is estimated or not.

This work is mainly focused on estimating rotor flux angle and speed by using model reference adaptive system. A combination of well-known open-loop observers, voltage model and current model is used to estimate the rotor flux angle and speed which are employed in direct field orientation. It is shown that the rotor flux angle and speed estimation performance of these schemes is quite satisfactory in both simulations and experimental results.

1.1 Induction Machine Control

An induction machine, a power converter and a controller are the three major components of an induction motor drive system. Some of the disciplines related to these components are electric machine design, electric machine modeling, sensing and measurement techniques, signal processing, power electronic design and electric machine control. It is beyond the scope of this research to address all of these areas: it will primarily focus on the issue related to the induction machine control.

A conventional low cost volts per hertz or a high performance field oriented controller can be used to control the machine. This chapter reviews the principles of the field orientation control of the induction machines and outline major problems in its design and implementation. The controllers required for induction motor drives can be divided into two major types: a conventional low cost volts per hertz v/f controller and torque controller [1]-[4]. In v/f control, the magnitudes of the voltage

and frequency are kept in proportion. The performance of the v/f control is sluggish, because the rate of change of voltage and frequency has to be low. A sudden acceleration or deceleration of the voltage and frequency can cause a transient change in the current, which can result in drastic problems. Some efforts were made to improve v/f control performance, but none of these improvements could yield a v/f torque controlled drive systems and this made DC motors a prominent choice for variable speed applications. This began to change when the theory of field orientation was introduced by Hasse and Blaschke. Field orientation control is considerably more complicated than DC motor control. The most popular class of the successful controllers is the vector controller because it controls both the amplitude and phase of AC excitation. This technique results in an orthogonal spatial orientation of the electromagnetic field and torque, commonly known as Field Oriented Control (FOC).

1.1.1 Field Oriented Control of Induction Machine

The concept of field orientation control is used to accomplish a decoupled control of flux and torque. This concept is copied from dc machine direct torque control that has three requirements [4]:

- an independently controlled armature current to overcome the effects of armature winding resistance, leakage inductance and induced voltage
- an independently controlled constant value of flux
- an independently controlled orthogonal spatial angle between the flux axis and magneto motive force (MMF) axis to avoid interaction of MMF and flux.

If all of these three requirements are met at every instant of time, the torque will follow the current, allowing an immediate torque control and decoupled flux and torque regulation.

Next a two phase d-q model of an induction machine rotating at the synchronous speed is introduced which will help to carry out this decoupled control concept to the induction machine. This model can be summarized by the following equations (see chapter 3 for detail):

$$u^{e}_{ds} = p\psi^{e}_{ds} - w_e\psi^{e}_{qs} + r_s i^{e}_{ds} \quad (1\text{-}1)$$

$$u^{e}_{qs} = p\psi^{e}_{qs} + w_e\psi^{e}_{ds} + r_s i^{e}_{qs} \quad (1\text{-}2)$$

$$0 = p\psi'^{e}_{qr} + (w_e - w_r)\psi'^{e}_{dr} + r'_r i'^{e}_{qr} \quad (1\text{-}3)$$

$$0 = p\psi'^{e}_{dr} - (w_e - w_r)\psi'^{e}_{qr} + r'_r i'^{e}_{dr} \quad (1\text{-}4)$$

$$\psi^{e}_{qs} = L_s i^{e}_{qs} + L_m i'^{e}_{qr} \quad (1\text{-}5)$$

$$\psi^{e}_{ds} = L_s i^{e}_{ds} + L_m i'^{e}_{dr} \quad (1\text{-}6)$$

$$\psi^{e}_{qr} = L_m i^{e}_{qs} + L_r i'^{e}_{qr} \quad (1\text{-}7)$$

$$\psi^{e}_{dr} = L_m i^{e}_{ds} + L_r i'^{e}_{dr} \quad (1\text{-}8)$$

$$T_e = \frac{3P}{2}\frac{L_m}{L_r}\left(\psi'^{e}_{dr}\, i^{e}_{qs} - \psi'^{e}_{qr}\, i^{e}_{ds}\right) \quad (1\text{-}9)$$

$$T_e = Jpw_r + Bw_r + T_L \quad (1\text{-}10)$$

This model is quite significant to synthesize the concept of field-oriented control. In this model it can be seen from the torque expression (1.9) that if the rotor flux along the q-axis is zero, then all the flux is aligned along the d axis and therefore the torque can be instantaneously controlled by controlling the current along q-axis. Then the question will be how it can be guaranteed that all the flux is aligned along the d-axis of the machine. When a three-phase voltage is applied to the machine, it produces a three-phase flux both in the stator and rotor. The three-phase fluxes can be converted into equivalents developed in two-phase stationary (d^s-q^s) frame. If this two phase fluxes along (d^s-q^s) axes are converted into an equivalent single vector then all the machine flux will be considered as aligned along that vector. This vector commonly specifies us d^e-axis which makes an angle θ_e with the stationary frame d^s-axis. The q^e-axis is set perpendicular to the d^e-axis. The flux along the q^e-axis in that case will obviously be zero. The phasor diagram Figure 1-1 shows these axes. The angle θ_e keeps changing as the machine input currents change. Thus the problem is

to know the angle θ_e accurately, so that the d-axis of the d^e-q^e frame is locked with the flux vector.

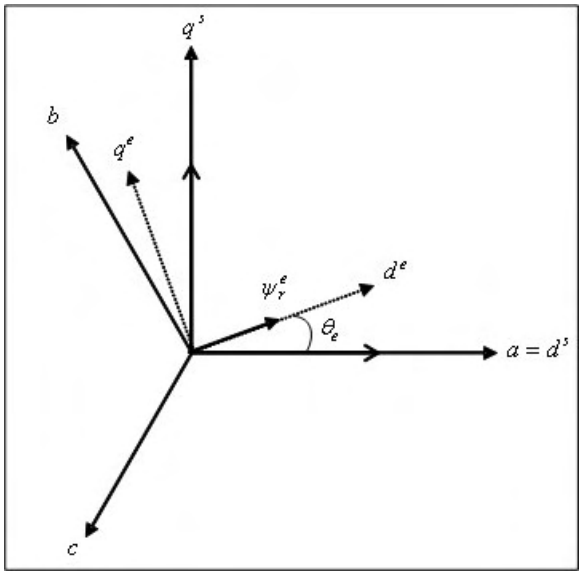

Figure 1-1 Phasor diagram of the field oriented drive system

The control input can be specified in terms of two phase synchronous frame i^e_{ds} and $i^e_{qs.}$ i^e_{ds} is aligned along the d^e-axis i.e. the flux vector, so does i^e_{qs} with the q^e-axis. These two-phase synchronous control inputs are converted into two-phase stationary and then to three- phase stationary control inputs. To accomplish this, the flux angle θ_e must be known precisely. The angle θ_e can be found either by Indirect Field Oriented Control (IFOC) or by Direct Field Oriented Control (DFOC). The controller implemented in this fashion that can achieve a decoupled control of the flux and the torque is known as field oriented controller. The block diagram is shown in Figure 1-2. In the field oriented control the flux can be regulated in the stator, air-gap or in rotor flux orientation [1]-[4].

The angle θ_e can be then calculated by adding the slip angle and the rotor angle. This slip angle includes the necessary and sufficient condition for decoupled control of flux and torque. The rotor speed can either be measured using an encoder or be estimated. In case the rotor speed is estimated the control technique is known as sensorless control.

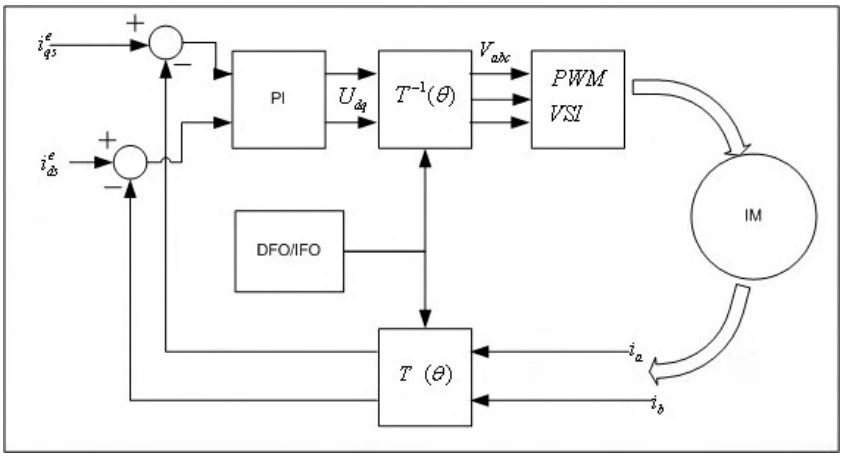

Figure 1-2 Field oriented induction motor drive system

In this technique the flux angle θ_e is classically calculated by means of sensing the air-gap flux using the flux sensing coils, or can be calculated by estimating the flux along the (d^s-q^s) axes using the voltage and current signals.

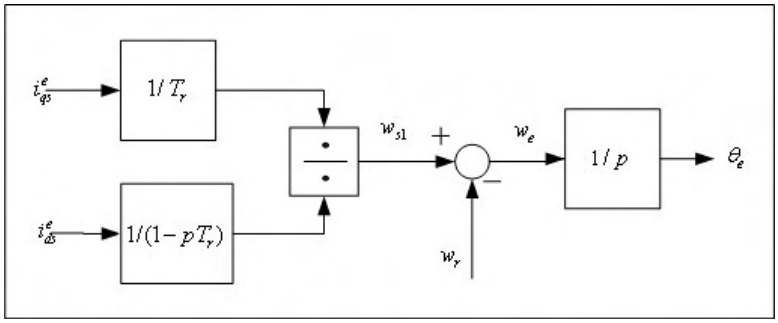

Figure 1-3 Indirect field oriented drive system

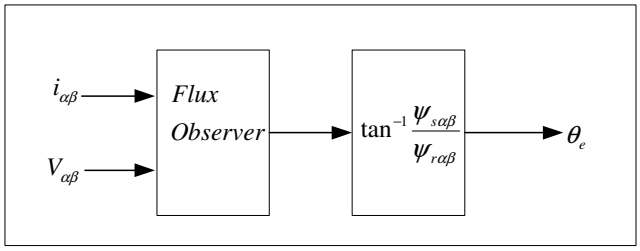

Figure 1-4 Direct field oriented drive system

1.1.2 Indirect Field Oriented Control

The indirect field oriented control is based on the determination of the slip frequency, which is a necessary and sufficient condition to guarantee the field orientation. When the field is once oriented the synchronous speed w_e is the same as the instantaneous speed of the rotor flux vector ψ^e_{dr} and d^e-axis of the d^e-q^e coordinate system is exactly locked on the rotor flux vector (rotor flux vector orientation). This facilities the flux control through the magnetizing current i^e_{ds} by aligning all the flux along the d^e-axis while applying the torque-producing component of the current along the q^e-axis. After decoupling the rotor flux and torque-producing component of the current components, the torque can be instantaneously controlled by controlling the current i^e_{qs}. The requirement to align the rotor flux along the d^e-axis of the d^e-q^e coordinate system means that the flux along the q^e-axis must be zero. This means that (1.7) becomes $i^e_{qs} = -(L_r i^e_{qr})/L_m$ and the current going through the q^e-axis of the mutual inductance is zero. Based on this restriction w_{sl} is:

$$w_{sl} = \frac{\frac{1}{T_r} i^e_{qs}}{\frac{1}{1 - pT_r} i^e_{ds}} \qquad (1\text{-}11)$$

This relation suggests that flux and torque can be controlled independently by specifying d^e-q^e axes currents provided that the slip frequency satisfies (1.11) all the time.

The concept of indirect field oriented control was developed in the history of AC machine control and has been widely studied by researchers during the last two decades. Rotor flux orientation is the original and usual choice for the indirect oriented control. Also the IFOC can be implemented in the stator and air-gap flux orientation as well. De Doncker introduced this concept in his universal field oriented controller[5]. In an air-gap flux the slip and flux relations are coupled equations and the d-axis current does not independently control the flux as it does in

the rotor flux orientation. For the constant air-gap flux orientation maximum produced torque is %20 less than the other two methods[3]. In the stator flux orientation, the transient reactance is a coupling factor and it varies with the operating conditions of the machine. In addition, among these methods Nasar shows that the rotor flux oriented control has linear torque curve[3]. Therefore, the most commonly used choice for IFO is the rotor flux orientation.

The IFOC is an open-loop feed-forward control in which the slip frequency is fed-forward guaranteeing the field orientation. This feed-forward control is very sensitive to the rotor open-circuit time-constant. Therefore, T_r must be known in order to achieve a decoupled control of torque and flux components by controlling i_{qs}^{e} and i_{ds}^{e}, respectively. When T_r is not set correctly the machine is said to be de-tuned and the performance will become sluggish due to loss of decoupled control of torque and flux. The rotor time-constant measurement, its effects of the system and its tuning to adapt the variations when the machine is operating, has been studied extensively in the area of IFOC [6-8]. Lorenz, Krishnan and Novotny studied the effect of temperature and saturation level on the rotor time-constant and stated that it can reduce the torque capability of the machine and torque/amps of the machine [6-8]. The de-tuning effect becomes more severe in the field-weakening region. Also, it results in a steady-state error and, transient oscillations in the rotor flux and torque. Some of the advanced control techniques such as estimation theory tools and adaptive control tools are also studied to estimate rotor time-constant and other motor parameters[11-14-21].

1.1.3 Direct Field Oriented Control

The DFOC and sensorless control relies heavily on accurate flux estimation. DFOC is most often used for sensorless control, because the flux observer used to estimate the synchronous speed or angle can also be used to estimate the machine speed. Investigation of ways to estimate the flux and speed of the induction machine has been extensively studied in the past two decades. Classically, the rotor flux was measured by using a special sensing element, such as Hall-effect sensors placed in the air-gap. An advantage of this method is that additional required parameters, L_{lr},

L_m, and L_r are not significantly affected by changes in temperature and flux level. However, the disadvantage of this method is that a flux sensor is expensive and needs special installation and maintenance. Another flux and speed estimation technique is saliency based with fundamental or high frequency signal injection. One advantage of saliency technique is that the saliency is not sensitive to actual motor parameters, but this method fails at low and zero speed level. When applied with high frequency signal injection, the method may cause torque ripples, vibration and audible noise [9].

Gabriel avoided the special flux sensors and coils by estimating the rotor flux from the terminal quantities (stator voltages and currents)[10]. This technique requires the knowledge of the stator resistance along with the stator-leakage, and rotor-leakage inductances and the magnetizing inductance. This method is commonly known as the Voltage Model Flux Observer (VMFO). The stator flux in the stationary reference frame can be estimated by the equations:

$$\dot{\psi}^s_{ds} = v^s_{ds} - r_s i^s_{ds} \tag{1-12}$$

$$\dot{\psi}^s_{qs} = v^s_{qs} - r_s i^s_{qs} \tag{1-13}$$

Then the rotor flux can be expressed as:

$$\psi^s_{dr} = \frac{L_r}{L_m}(\psi^s_{ds} - L_\sigma i^s_{ds}) \tag{1-14}$$

$$\psi^s_{qr} = \frac{L_r}{L_m}(\psi^s_{qs} - L_\sigma i^s_{qs}) \tag{1-15}$$

where $L_\sigma = (L_s - L_m^2 / L_r)$ is the transient leakage inductance.

In this model, integration of the low frequency signals, dominance of stator IR drop at low speed and leakage inductance variation result in a less precise flux estimation. Integration at low frequency has been studied and there are three different alternatives[11]. Estimation of rotor flux from the terminal quantities depends on parameters such as stator resistance and leakage inductance. The study of parameter sensitivity shows that the leakage inductance can significantly affect the system

performance regarding to stability, dynamic response and utilization of the machine and the inverter.

The Current Model Flux Observer (CMFO) is an alternative approach to overcome the problems caused by the changes in leakage inductance and stator resistance at low speed. In this model flux can be estimated as:

$$\dot{\psi}_{dr}^{s} = -\frac{1}{T_r}\psi_{dr}^{s} - w_r\psi_{qr}^{s} + \frac{L_m}{T_r}i_{ds}^{s} \tag{1-16}$$

$$\dot{\psi}_{qr}^{s} = -\frac{1}{T_r}\psi_{qr}^{s} - w_r\psi_{dr}^{s} + \frac{L_m}{T_r}i_{qs}^{s} \tag{1-17}$$

However, CMFO does not work well at high speeds due to its sensitivity against the changes in the rotor resistance. Jansen did an extensive study on both VMFO and CMFO, based on direct field oriented control, discussed the design and accuracy assessment of various flux observers, and compared and analyzed the alternative flux observers[12]. To further improve the observer performance, closed-loop rotor flux observers are proposed which use the estimated stator current error or the estimated stator voltage error to estimate the rotor flux[12-13]. Lennart proposed reduced-order observers for this task[14].

1.2 Variable Speed Control Using Advanced Control Algorithms

There are two issues in motion control of induction machine drives using field orientation. One is to make the resulting drive system and the controller robust against parameter deviations and disturbances. The other is to make the system intelligent e.g. to adjust the control system itself to environment changes and task requirements. Specifically, even though FOC provides a decoupled control of flux and torque, a near-instantaneous control of torque for an induction machine drive, for high performance speed regulation plays an important role, since the command current i_{qs}^{*} is produced by speed-loop, which feeds the induction machine via the current regulation to produce the desired torque response. If the speed regulation loop fails to produce the command current correctly, than the desired torque response

will not be produced by the induction machine. In addition, the failure to produce the correct current command may cause the degradation in slip command as well. As a result a satisfactory speed regulation is extremely important not only to produce desired torque performance from the induction machine but also to guarantee the decoupling between control of torque and flux.

Conventionally, a PI controller has been used for the speed regulation to generate a command current for the last two decades and accepted by industry because of its simplicity. Even though a well-tuned PI controller performs well for a field oriented induction machine during steady-state, the transient speed response of the machine, especially for the variable speed tracking, is sometimes problematic. In the last two decades, alternative control algorithms for the speed regulation are investigated. Among these, fuzzy logic, sliding mode and adaptive nonlinear control algorithms gain much attention, however these controllers are not in the scope of this thesis.

A traditional rotor flux oriented induction machine drive offers a control performance but often requires additional sensors on the machine. This adds to the cost and complexity of the drive system. To avoid these sensors on the machine, many different algorithms are proposed in the last three decades to estimate the rotor flux vector and/or rotor shaft speed. The recent trend in field-oriented control is to avoid sensors and use algorithms to use the terminal quantities of the machine for the estimation of the fluxes and speed and they can easily be applied to any induction machine. Therefore the focus in this study is on these algorithms.

Before looking into individual approaches, the common problems of the speed and flux estimation are discussed briefly for general field orientation and state estimation algorithms.

- Parameter sensitivity: One of the most important problem of the sensorless control algorithms for the field oriented induction machine drives is insufficient information about the machine parameters which yield the estimation of some machine parameters along with the sensorless structure. Among these parameters stator resistance, rotor resistance and rotor time-constant play more important role than the other parameters since they are more sensitive to temperature changes. The

knowledge of the stator resistance r_s, correctly is important to widen the operation region toward the lower speed range. Since at low speeds the induced voltage is low and stator resistance drop becomes dominant, the mismatching of the stator resistance induces instability of the system. On the other hand errors in determining the actual value of the rotor resistance r_r, may cause both instability of the system and speed estimation error proportional to r_r[15]. Also correct T_r value is vital for the decoupling factor in IFOC.

- Integration issue: The other important issue regarding to many of the topologies is the integration process inherited from the induction machine dynamics. To calculate the state variables of the system, integration process is needed. However, it is difficult to decide on the initial value which will not cause the drift of a pure integrator. Usually, to overcome this problem an integrator is replaced by a low-pass filter.
- Overlapping-loop issues: In a sensorless control system, the control loop and the speed estimation loop may overlap and these loops influence each other. As a result, outputs of both of these loops may not be designed independently; in some bad cases this dependency may influence the stability or performance of the overall system.

The algorithms, where terminal quantities of the machine are used to estimate the fluxes and speed of the machine, are categorized in two basic groups. First one is "the open-loop observer". In a sense it is an on-line model of the machine, which do not use the feedback correction. Second one is "the closed-loop observer" where the feedback correction is used along with the machine model itself to improve the estimation accuracy. These two basic groups can also be subdivided based on the control method used. These can be summarized as:

- Open-loop observers;
  - Current model
  - Voltage model
  - Cancellation method
  - Full-order observer
- Closed-loop observers;

- Model Referenced Adaptive Systems (MRAS)
- Kalman filter techniques
- Adaptive observers based on both voltage and current model
- Neural network flux and speed estimators
- Sliding mode flux and speed estimators

Open-loop observers in general use different forms of the induction machine differential equations. Current model based open-loop observers use the measured stator currents and rotor velocity[12-14]. The velocity dependency of the current model is very important since this means that even though using the estimated flux eliminates the need for the use of a flux sensor, the need for the use of the position sensor is still there. On the other hand voltage model based open-loop observers use the measured stator voltage and current as inputs. These types of estimators require a pure integration that is difficult to implement for low excitation frequencies due to the offset and initial condition problems. Cancellation method open-loop observers can be formed by using measured stator voltage, stator current and rotor velocity as inputs. They use the differentiation to cancel the effect of the integration. However it suffers from two main drawbacks. One is the need for the derivation which makes the method more susceptible to noise than the other methods. The other drawback is the need for the accurate knowledge of the rotor velocity similar to the current model. A full-order open-loop observer on the other hand can be formed using only the measured stator voltage and rotor velocity as inputs where the stator current appears as an estimated quantity. Because of its dependency on the stator current estimation, the full-order observer will not exhibit better performance than the current model. Furthermore, parameter sensitivity and observer gain are the problems to be tuned in a full-order observer design[16]. These open-loop observer structures are all based on the induction machine model and they do not employ any feedback. Therefore, they are quite sensitive to parameter variations, which yield the estimation of some machine parameters along with the sensorless structure.

On the other hand some kind of feedback may be helpful to produce more robust structures against parameter variations. For this purpose many closed-loop topologies are proposed using different induction machine models and control

methods. Among these MRAS attracts attention and several different algorithms are produced. In MRAS, in general a comparison is made between the outputs of two estimators. The estimator which does not contain the quantity to be estimated can be considered as a reference model of the induction machine. The other one, which contains the estimated quantity, is considered as an adjustable model. The error between these two estimators is used as an input to an adaptation mechanism. For sensorless control algorithms most of the times the quantity which differs the reference model from the adjustable model is the rotor speed. When the estimated rotor speed in the adjustable model is changed in such a way that the difference between two estimators converges to zero asymptotically, the estimated rotor speed will be equal to the actual rotor speed. The basics of the analysis and design of MRAS are discussed by Vas, and Trzynadlowski [2, 17]. The voltage model here is assumed as reference model, the current model, however, is assumed as the adjustable model and the estimated rotor flux is assumed as the reference parameter to be compared[15, 18, and 19]. Similarly speed estimators, proposed here, are based on the MRAS, and a secondary variable is introduced as the reference quantity by putting the rotor flux through a first-order delay instead of a pure integration to nullify the offset by Robyns and Frederique[16]. However, their algorithm produces inaccurate estimated speed when the excitation frequency goes below a certain level. In addition these algorithms suffer from the machine parameter uncertainties because of the reference model since the parameter variation in the reference model cannot be corrected. An alternative MRAS based on the electromotive force rather than rotor flux as reference quantity for speed estimation is suggested in order to overcome the integration problem[19, 21]. Further, another new auxiliary variable is introduced which represents the instantaneous reactive power for maintaining the magnetizing current. In this MRAS algorithm stator resistance disappear from equations making the algorithm robust against that parameter. Zhen proposed an interesting MRAS structure that is built with two mutual MRAS schemes[22]. In this structure, the reference model and the adjustable models are interchangeable. For rotor speed estimation, one model is used as reference model and other model is used as adjustable model. The pure integration is removed from reference model. For stator resistance estimation, however, these models switch their roles.

1.3 Overview of the Chapters

This thesis is organized as follows:

Chapter 1 is devoted to vector control fundamentals. Indirect and direct control methods are introduced and sensorless direct field oriented control using flux and open-loop speed estimators are discussed briefly.

In Chapter 2, generalized dynamic mathematical model of the induction motor in different reference frames are presented.

Chapter 3 presents the theoretical background of Space Vector Pulse Width Modulation (SVPWM) in detail. The results of simulation and the DSP implementation of this theory are illustrated.

Chapter 4 includes the detailed description of the flux estimation with the assumption that the rotor current is zero. The method of the flux estimation is given when the measured speed signal is no longer available. The speed estimation method based upon the mathematical model of the induction motor is also given in this chapter.

Chapter 5 presents the obtained simulated and experimental results of the drive system for both open-loop and closed-loop cases.

In Chapter 6 implementation method for vector control is introduced. The experimental setup used for testing the proposed sensorless drive system is described.

Chapter 7 summarizes the thesis and concludes the performance of the vector controlled induction motor.

2 INDUCTION MACHINE MODELLING

2.1 The Induction Motor

The two names for the same type of motor, *Induction motor* and *Asynchronous motor*, describe the two characteristics in which this type of motor differs from DC motors and synchronous motors. Induction refers to the fact that the field in the rotor is induced by the stator currents, and asynchronous refers to the fact that the rotor speed is not equal to the stator frequency. No sliding contacts and permanent magnets are needed to make an induction motor work, which makes it very simple and cheap to manufacture. As motors, they are rugged and require very little maintenance. However, their speeds are not as easily controlled as with DC motors. They draw large starting currents, and operate with a poor lagging factor when lightly loaded.

2.2 Circuit Model of a Three Phase Induction Motor

Voltage Equations: Using the coupled circuit approach the voltage equations of the magnetically coupled stator a rotor circuit for an induction motor can be written as follows:

Stator Voltage Equations:

$$V_{as} = i_{as} r_s + \frac{d\psi_{as}}{dt} \; V \tag{2-1}$$

$$V_{bs} = i_{bs} r_s + \frac{d\psi_{bs}}{dt} \; V \tag{2-2}$$

$$V_{cs} = i_{cs} r_s + \frac{d\psi_{cs}}{dt} \ V \tag{2-3}$$

Rotor Voltage Equations:

$$V_{ar} = i_{ar} r_r + \frac{d\psi_{ar}}{dt} \ V \tag{2-4}$$

$$V_{br} = i_{br} r_r + \frac{d\psi_{br}}{dt} \ V \tag{2-5}$$

$$V_{cr} = i_{cr} r_{rs} + \frac{d\psi_{cr}}{dt} \ V \tag{2-6}$$

Flux Linkage Equations: In matrix notation, the flux linkages of the stator and rotor windings, in terms of the winding inductances and currents, may be written compactly as

$$\begin{bmatrix} \psi_s^{abc} \\ \psi_r^{abc} \end{bmatrix} = \begin{bmatrix} L_{ss}^{abc} & L_{sr}^{abc} \\ L_{rs}^{abc} & L_{rr}^{abc} \end{bmatrix} \begin{bmatrix} i_s^{abc} \\ i_r^{abc} \end{bmatrix} \ Wb.turns \tag{2-7}$$

where

$$\begin{aligned} \psi_s^{abc} &= (\psi_{as}, \psi_{bs}, \psi_{cs})^t \\ \psi_r^{abc} &= (\psi_{ar}, \psi_{br}, \psi_{cr})^t \\ i_s^{abc} &= (i_{as}, i_{bs}, i_{cs})^t \\ i_r^{abc} &= (i_{ar}, i_{br}, i_{cr})^t \end{aligned} \tag{2-8}$$

and the superscript (t) denotes the transpose of the array.

The sub-matrices of the stator-to-rotor and rotor-to-rotor winding inductances are of the form:

$$\begin{aligned} L_{ss}^{abc} &= \begin{bmatrix} L_{ls} + L_{ss} & L_{sm} & L_{sm} \\ L_{sm} & L_{ls} + L_{ss} & L_{sm} \\ L_{sm} & L_{sm} & L_{ls} + L_{ss} \end{bmatrix} \ H \\ L_{rr}^{abc} &= \begin{bmatrix} L_r + L_{rr} & L_{rm} & L_{rm} \\ L_{rm} & L_r + L_{rr} & L_{rm} \\ L_{rm} & L_{rm} & L_r + L_{rr} \end{bmatrix} \ H \end{aligned} \tag{2-9}$$

Those of the stator to rotor mutual inductances are dependent on the rotor angle, that is:

$$L_{sr}^{abc} = [L_{rs}^{abc}]^t = L_{sr}\begin{bmatrix} \cos\theta_r & \cos\left(\theta_r + \frac{2\pi}{3}\right) & \cos\left(\theta_r - \frac{2\pi}{3}\right) \\ \cos\left(\theta_r - \frac{2\pi}{3}\right) & \cos\theta_r & \cos\left(\theta_r + \frac{2\pi}{3}\right) \\ \cos\left(\theta_r + \frac{2\pi}{3}\right) & \cos\left(\theta_r - \frac{2\pi}{3}\right) & \cos\theta_r \end{bmatrix} \quad H \text{ (2-10)}$$

where L_{ls} is the per phase stator winding leakage inductance, L_{lr} is the per phase rotor winding leakage inductance, L_{ss} is the self inductance of the stator winding, L_{rr} is the self inductance of the rotor winding, L_{sm} is the mutual inductance between stator windings, L_{rm} is the mutual inductance between rotor windings, and L_{sr} is the peak value of the stator to rotor mutual inductance.

Note that the idealized machine is described by six first-order differential equations, one for each winding. These differential equations are coupled to one another through the mutual inductance between the windings. In particular, the stator to rotor coupling terms vary with time. Mathematical transformations like the dq or αβ can facilitate the computation of the transient solution of the above induction motor model by transforming the differential equations with time-varying inductances to differential equations with constant inductances.

2.2.1 Machine Model in Arbitrary dq0 Reference Frame

The idealized three-phase induction machine is assumed to have symmetrical air-gap. The dq0 reference frames are usually selected on the basis of conveniences or computational reduction. The two commonly used reference frames in the analysis of induction machine are the stationary and synchronously rotating frames. Each has an advantage for some purpose. In the stationary rotating reference, the dq variables of the machine are in the same frame as those normally used for the supply network. In the synchronously rotating frame, the dq variables are steady in steady state. Here,

firstly the equations of the induction machine in the arbitrary reference frame which is rotating at a speed of (w) in the direction of the rotor rotation will be derived. Those if the induction machine in the stationary frame can then be obtained by setting w=0, and those for the synchronously rotating frame are obtained by setting $w=w_e$. The relationship between the abc quantities and dq0 quantities of a reference frame rotating at an angular speed, w, is shown in Figure 2-1.

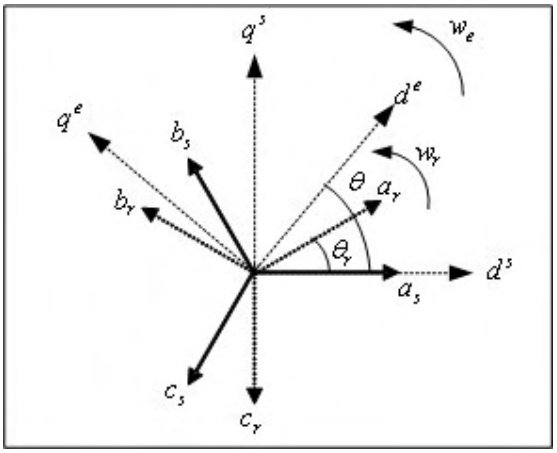

Figure 2-1 Relationship between abc and arbitrary dq0

The transformation equation from abc to this qd0 reference frame is given by:

$$\begin{bmatrix} f_q \\ f_d \\ f_0 \end{bmatrix} = \left[T_{qd0}(\theta)\right] \begin{bmatrix} f_a \\ f_b \\ f_0 \end{bmatrix} \tag{2-11}$$

where the variable f can be the phase voltages, current, or flux linkages of the machine. The transformation angle, θ(t), between the q-axis of the reference frame rotating at a speed of w and the a-axis of the stationary stator winding may be expressed as:

$$\theta(t) = \int_0^t w(t)dt + \theta(0) \qquad elec.rad. \tag{2-12}$$

Likewise, the rotor angle, $\theta_r(t)$, between the axes of the stator and rotor a-phases for a rotor rotating with speed $w_r(t)$ may be expressed as:

$$\theta_r(t) = \int_0^t w_r(t)dt + \theta_r(0) \qquad elec.rad. \tag{2-13}$$

2.2.1.1 qd0 Voltage Equations

In matrix notation, the stator winding abc voltage equations can be expressed as:

$$v_s^{abc} = p\psi_s^{abc} + r_s^{abc} i_s^{abc} \tag{2-14}$$

Applying the transformations (Clarke and Park) to the voltage, current and flux linkages (2.14) becomes

$$v_s^{qd0} = \left[T_{qd0}(\theta)\right] p \left[T_{qd0}(\theta)\right]^{-1} \left[\psi_s^{qd0}\right] + \left[T_{qd0}(\theta)\right] r_s \left[T_{qd0}(\theta)\right]^{-1} \left[i_s^{qd0}\right] \tag{2-15}$$

solving the equation above it becomes:

$$v_s^{qd0} = w \begin{bmatrix} 0 & 1 & 0 \\ -1 & 0 & 0 \\ 0 & 0 & 0 \end{bmatrix} \psi_s^{qd0} + p\psi_s^{qd0} + r_s^{qd0} i_s^{qd0} \tag{2-16}$$

where

$$w = \frac{d\theta}{dt} \qquad and \qquad r_s^{qd0} = r_s \begin{bmatrix} 1 & 0 & 0 \\ 0 & 1 & 0 \\ 0 & 0 & 1 \end{bmatrix} \tag{2-17}$$

Likewise, the rotor voltage equation becomes:

$$v_r^{qd0} = (w - w_r) \begin{bmatrix} 0 & 1 & 0 \\ -1 & 0 & 0 \\ 0 & 0 & 0 \end{bmatrix} \psi_r^{qds} + p\psi_r^{qd0} + r_r^{qd0} i_r^{qd0} \tag{2-18}$$

2.2.1.2 qd0 Flux Linkage Relation

The stator qd0 flux linkages are obtained by applying $T_{qd0}(\theta)$ to the stator abc flux linkages in (2.7).

$$\psi_s^{qd0} = [T_{qd0}(\theta)]\ (L_{ss}^{abc}\ i_{ss}^{abc} + L_{sr}^{abc}\ i_{sr}^{abc}) \tag{2-19}$$

skipping the transformation steps the stator and the rotor flux linkage relationships can be expressed compactly:

$$\begin{bmatrix} \psi_{qs} \\ \psi_{ds} \\ \psi_{0s} \\ \psi_{qr} \\ \psi_{dr} \\ \psi_{0r} \end{bmatrix} = \begin{bmatrix} L_{sl}+L_m & 0 & 0 & L_m & 0 & 0 \\ 0 & L_{sl}+L_m & 0 & 0 & L_m & 0 \\ 0 & 0 & L_{ls} & 0 & 0 & 0 \\ L_m & 0 & 0 & L'_{lr}+L_m & 0 & 0 \\ 0 & L_m & 0 & 0 & L'_{lr}+L_m & 0 \\ 0 & 0 & 0 & 0 & 0 & L_m \end{bmatrix} \begin{bmatrix} i_{qs} \\ i_{ds} \\ i_{0s} \\ i_{qr} \\ i_{dr} \\ i_{0r} \end{bmatrix} \tag{2-20}$$

Substituting (2.20) into voltage equations and then grouping q, d, 0, and θ terms in the resulting voltage equations, we obtain the voltage equations that suggest the equivalent circuit shown in Figure 2-2.

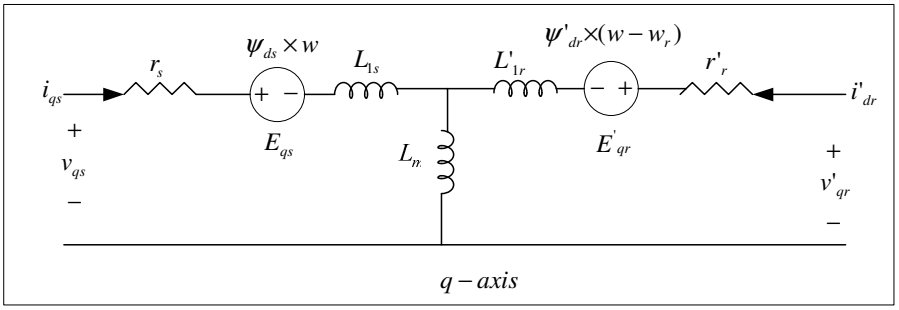

Figure 2-2 Model of an induction machine in the arbitrary reference frame

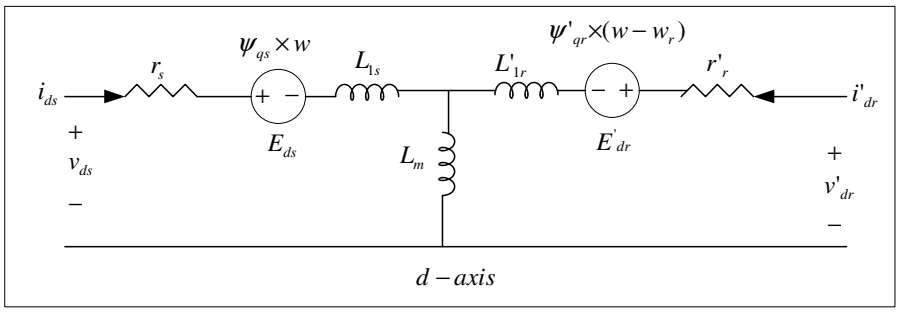

Figure 2-3 Model of an induction machine in the arbitrary reference frame

2.2.1.3 qd0 Torque Equations

The sum of the instantaneous input power to all six windings of the stator and rotor is given by :

$$p_{in} = v_{as}i_{as} + v_{bs}i_{bs} + v_{cs}i_{cs} + v'_{ar}i'_{ar} + v'_{br}i'_{br} + v'_{cr}i'_{cr} \quad W \qquad (2\text{-}21)$$

in terms of dq quantities

$$p_{in} = \frac{3}{2}(v_{qs}i_{qs} + v_{ds}i_{ds} + 2v_{0s}i_{0s} + v'_{qr}i'_{qr} + v'_{dr}i'_{dr} + 2v'_{0r}i'_{0r})W \qquad (2\text{-}22)$$

Using stator and rotor voltages to substitute for the voltages on the right hand side of (2.22), we obtain three kinds of terms: i^2r, $i\,p\psi$, *and* $w\psi i$. (i^2r) terms are the cupper losses. The ($ip\psi$) terms represent the rate of exchange of magnetic field energy between windings. The electromechanical torque developed by the machine is given by the sum of the ($w\psi i$) terms divided by mechanical speed, that is:

$$T_{em} = \frac{3}{2}\frac{p}{2w_r}\left[w(\psi_{ds}i_{qs} - \psi_{qs}i_{ds}) + (w - w_r)(\psi'_{dr}i'_{qr} - \psi'_{qr}i'_{dr})\right] \quad Nm \quad (2\text{-}23)$$

using the flux linkage relationships, T_{em} can also be expressed as follows:

$$T_{em} = \frac{3}{2}\frac{P}{2w_r}\left[w(\psi_{ds}i_{qs} - \psi_{qs}i_{ds}) + (w - w_r)(\psi'_{dr}i'_{qr} - \psi'_{qr}i'_{dr})\right] \quad Nm \quad (2\text{-}24)$$

Using the flux linkage relationships, one can show that

$$
\begin{aligned}
T_{em} &= \frac{3}{2}\frac{P}{2}(\psi'_{qr} i'_{dr} - \psi'_{dr} i'_{qr}) \quad Nm \\
&= \frac{3}{2}\frac{P}{2}(\psi_{ds} i_{qs} - \psi_{qs} i_{ds}) \quad Nm \\
&= \frac{3}{2}\frac{P}{2} L_m (i'_{dr} i_{qs} - i'_{qr} i_{ds}) \quad Nm
\end{aligned}
\tag{2-25}
$$

One can rearrange the torque equations by inserting the speed voltage terms given below:

$$
\begin{aligned}
E_{qs} &= w\psi_{ds} & E_{ds} &= -w\psi_{qs} \\
E'_{qr} &= (w - w_r)\psi'_{dr} & E'_{dr} &= -(w - w_r)\psi'_{qr}
\end{aligned}
\tag{2-26}
$$

Stator qd0 voltage equations:

$$
\begin{aligned}
v_{qs} &= p\psi_{qs} + w\psi_{ds} + r_s i_{qs} \\
v_{ds} &= p\psi_{ds} - w\psi_{qs} + r_s i_{ds} \\
v_{0s} &= p\psi_{0s} + r_s i_{0s}
\end{aligned}
\tag{2-27}
$$

Rotor qd0 voltage equations:

$$
\begin{aligned}
v'_{qr} &= p\psi'_{qr} + (w - w_r)\psi'_{dr} + r'_r i'_{qr} \\
v'_{dr} &= p\psi'_{dr} - (w - w_r)\psi'_{qr} + r'_r i'_{dr} \\
v'_{0r} &= p\psi'_{0r} + r'_r i'_{0r}
\end{aligned}
\tag{2-28}
$$

where

$$
\begin{bmatrix} \psi_{qs} \\ \psi_{ds} \\ \psi_{0s} \\ \psi_{qr} \\ \psi_{dr} \\ \psi_{0r} \end{bmatrix} = \begin{bmatrix} L_{sl} + L_m & 0 & 0 & L_m & 0 & 0 \\ 0 & L_{sl} + L_m & 0 & 0 & L_m & 0 \\ 0 & 0 & L_{ls} & 0 & 0 & 0 \\ L_m & 0 & 0 & L'_{lr} + L_m & 0 & 0 \\ 0 & L_m & 0 & 0 & L'_{lr} + L_m & 0 \\ 0 & 0 & 0 & 0 & 0 & L_m \end{bmatrix} \begin{bmatrix} i_{qs} \\ i_{ds} \\ i_{0s} \\ i_{qr} \\ i_{dr} \\ i_{0r} \end{bmatrix}
\tag{2-29}
$$

Torque Equation:

$$T_{em} = \frac{3}{2}\frac{P}{2w_r}\left[w(\psi_{ds}i_{qs} - \psi_{qs}i_{ds}) + (w - w_r)(\psi'_{dr}i'_{qr} - \psi'_{qr}i'_{dr})\right] \quad Nm \quad (2\text{-}30)$$

2.2.2 qd0 Stationary and Synchronous Reference Frames

There is seldom a need to simulate an induction machine in the arbitrary rotating reference frame. But it is useful to convert a unified model to other frames. The most commonly used ones are, two marginal cases of the arbitrary rotating frame, stationary reference frame and synchronously rotating frame. For transient studies of adjustable speed drives, it is usually more convenient to simulate an induction machine and its converter on a stationary reference frame. Moreover, calculations with stationary reference frame are less complex due to zero frame speed (some terms cancelled). For small signal stability analysis about some operating condition, a synchronously rotating frame which yields steady values of steady-state voltages and currents under balanced conditions is used.

Since we have derived the equations of the induction machine for the general case, that is in the arbitrary rotating reference frame, the equations of the machine in the stationary and synchronously rotating reference frame, w to zero and w_e, respectively. To distinguish these two frames from each other, an additional superscript will be used, s for stationary frame variables and e for synchronously rotating frame variables.

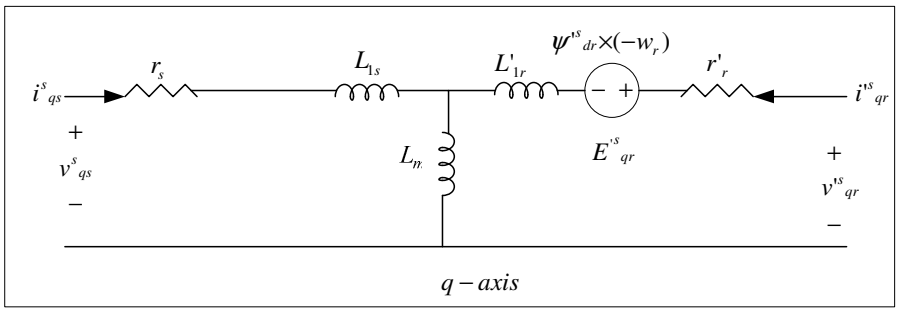

Figure 2-4 Model of an induction machine in the stationary frame

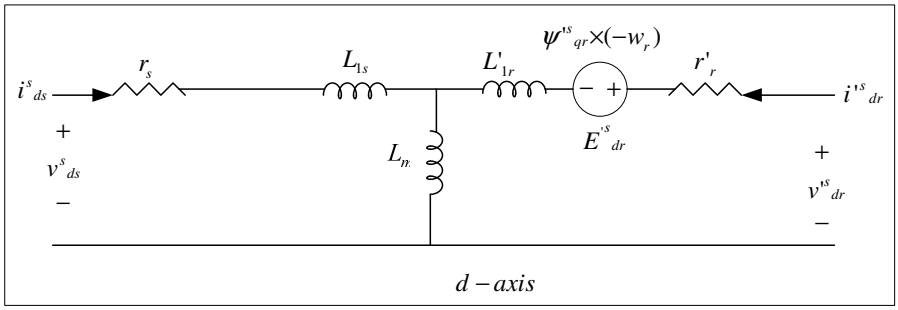

Figure 2-5 Model of an induction machine in the stationary frame

Stator qd0 voltage equations:

$$\begin{aligned} v^s_{qs} &= p\psi^s_{qs} + r_s i^s_{qs} \\ v^s_{ds} &= p\psi^s_{ds} + r_s i^s_{ds} \\ v_{0s} &= p\psi^s_{0s} + r_s i_{0s} \end{aligned} \tag{2-31}$$

Rotor qd0 voltage equations:

$$\begin{aligned} v'^s_{qr} &= p\psi'^s_{qr} + (-w_r)\psi'^s_{dr} + r'_r i'^s_{qr} \\ v'^s_{dr} &= p\psi'^s_{dr} + (w_r)\psi'^s_{qr} + r'_r i'^s_{dr} \\ v'_{0r} &= p\psi'_{0r} + r'_r i'_{0r} \end{aligned} \tag{2-32}$$

where

$$\begin{bmatrix} \psi^{s}_{qs} \\ \psi^{s}_{ds} \\ \psi_{0s} \\ \psi^{s}_{qr} \\ \psi^{s}_{dr} \\ \psi_{0r} \end{bmatrix} = \begin{bmatrix} L_{sl}+L_m & 0 & 0 & L_m & 0 & 0 \\ 0 & L_{sl}+L_m & 0 & 0 & L_m & 0 \\ 0 & 0 & L_{ls} & 0 & 0 & 0 \\ L_m & 0 & 0 & L'_{lr}+L_m & 0 & 0 \\ 0 & L_m & 0 & 0 & L'_{lr}+L_m & 0 \\ 0 & 0 & 0 & 0 & 0 & L_m \end{bmatrix} \begin{bmatrix} i^{s}_{qs} \\ i^{s}_{ds} \\ i_{0s} \\ i^{s}_{qr} \\ i^{s}_{dr} \\ i_{0r} \end{bmatrix} \quad (2\text{-}33)$$

Torque Equation:

$$\begin{aligned} T_{em} &= \frac{3}{2}\frac{P}{2}(\psi'^{s}_{qr} i'^{s}_{dr} - \psi'^{s}_{dr} i'^{s}_{qr}) \qquad Nm \\ &= \frac{3}{2}\frac{P}{2}(\psi^{s}_{ds} i^{s}_{qs} - \psi^{s}_{qs} i^{s}_{ds}) \qquad Nm \\ &= \frac{3}{2}\frac{P}{2} L_m (i'^{s}_{dr} i^{s}_{qs} - i'^{s}_{qr} i^{s}_{ds}) \qquad Nm \end{aligned} \quad (2\text{-}34)$$

The equivalent induction machine circuit and induction machine equations in the synchronous reference frame are given in (2.35-2.38) and Figure 2-6, Figure 2-7. 3-phase AC quantities are simulated in both stationary frame and synchronously rotating frame.

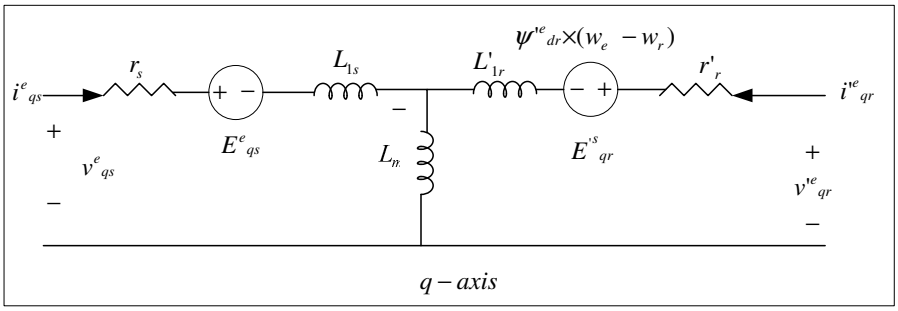

Figure 2-6 Model of an induction machine in the synchronous frame

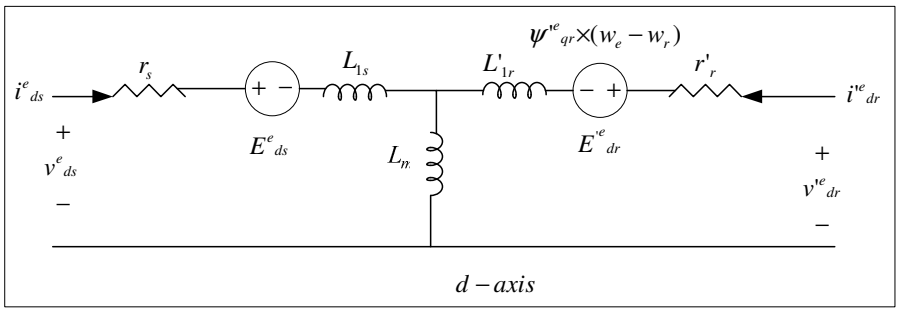

Figure 2-7 Model of an induction machine in the synchronous frame

Stator qd0 voltage equations:

$$\begin{aligned} v^e_{qs} &= p\psi^e_{qs} + w_e\psi^e_{ds} + r_s i^e_{qs} \\ v^e_{ds} &= p\psi^e_{ds} - w_e\psi^e_{qs} + r_s i^e_{ds} \\ v_{0s} &= p\psi_{0s} + r_s i_{0s} \end{aligned} \tag{2-35}$$

Rotor qd0 voltage equations:

$$\begin{aligned} v'^{e}_{qr} &= p\psi'^{e}_{qr} + (w_e - w_r)\psi'^{e}_{dr} + r'_r i'^{e}_{qr} \\ v'^{e}_{dr} &= p\psi'^{e}_{dr} - (w_e - w_r)\psi'^{e}_{qr} + r'_r i'^{e}_{dr} \\ v'_{0r} &= p\psi'_{0r} + r'_r i'_{0r} \end{aligned} \tag{2-36}$$

where

$$\begin{bmatrix} \psi^e_{qs} \\ \psi^e_{ds} \\ \psi_{0s} \\ \psi^e_{qr} \\ \psi^e_{dr} \\ \psi_{0r} \end{bmatrix} = \begin{bmatrix} L_{sl}+L_m & 0 & 0 & L_m & 0 & 0 \\ 0 & L_{sl}+L_m & 0 & 0 & L_m & 0 \\ 0 & 0 & L_{ls} & 0 & 0 & 0 \\ L_m & 0 & 0 & L'_{lr}+L_m & 0 & 0 \\ 0 & L_m & 0 & 0 & L'_{lr}+L_m & 0 \\ 0 & 0 & 0 & 0 & 0 & L_m \end{bmatrix} \begin{bmatrix} i^e_{qs} \\ i^e_{ds} \\ i_{0s} \\ i^e_{qr} \\ i^e_{dr} \\ i_{0r} \end{bmatrix} \tag{2-37}$$

Torque Equations:

$$\begin{aligned} T_{em} &= \frac{3}{2}\frac{P}{2}(\psi'^{e}_{qr} i'^{e}_{dr} - \psi'^{e}_{dr} i'^{e}_{qr}) \qquad Nm \\ &= \frac{3}{2}\frac{P}{2}(\psi^e_{ds} i^e_{qs} - \psi^e_{qs} i^e_{ds}) \qquad Nm \\ &= \frac{3}{2}\frac{P}{2} L_m (i'^{e}_{dr} i^e_{qs} - i'^{e}_{qr} i^e_{ds}) \qquad Nm \end{aligned} \tag{2-38}$$

3 PULSE WIDTH MODULATION with SPACE VECTOR THEORY

3.1 Inverters

Three phase inverters, supplying voltages and currents of adjustable frequency and magnitude to the stator, are important elements of adjustable speed induction motor drive systems. Inverters with semiconductor power switches are d.c. to a.c. static power converters. Depending on the type of d.c. source supplying the inverter, they can be classified as voltage fed inverters (VFI) or current fed inverters (CFI). In practice, the d.c. source is usually a rectifier, typically of the three phase bridge configuration, with d.c. link connected between the rectifier and the inverter. The d.c. link is a simple inductive, capacitive, or inductive-capacitive low-pass filter, since neither the voltage across a capacitor nor the current through an inductor can change instantaneously. A capacitive-output d.c. link is used for a VFI and an inductive-output link is employed in CFI. VFIs can be either voltage or current controlled. In a voltage-controlled inverter, it is the frequency and magnitude of the fundamental of the output voltage that is adjusted. Feed-forward voltage control is employed, since the inverter voltage is dependent only on the supply voltage and the states of the inverter switches, and, therefore, accurately predictable. Current controlled VFIs require sensors of the output currents which provide the necessary control feedback. The type of semiconductor power switch used in an inverter depends on the volt-ampere rating of the inverter, as well as on other operating and economic considerations, such as switching frequency or cost of the system. Taking into account the transient and steady state requirements, we have used 1200V, 40A IGBT switches. With appropriate heat sink, we can rise to 20 KHz, however at 10 KHz, switching losses and conduction losses become equal moreover, complex

mathematical algorithms require much time. Thus 10 KHz is selected as the switching frequency in our algorithms.

3.1.1 Voltage Source Inverter (VFI)

A diagram of the power circuit of a three phase VFI is shown in the Figure 3-1. The circuit has bridge topology with three branches (phases), each consisting of two power switches and two freewheeling diodes. The inverter here is supplied from an uncontrolled, diode-based rectifier, via d.c. link which contains an LC filter in the inverted configuration. It allows the power flow from the supply to the load only. Power flow cannot be reversed, if the load is to feed the power back to the supply due to the diode rectifier structure at the input side of the dc link. Therefore, in drive systems where the VFI-fed motor may not operate as a generator, a more complex supply system must be used. These involve either a braking resistance connected across the d.c. link or replacement of the uncontrolled rectifier by a dual converter. The inverter may be supported with braking resistance connected across the d.c. link via a free wheeling diode and a transistor. When the power flow is reversed it is dissipated in the braking resistor putting the system into dynamic braking mode of operation.

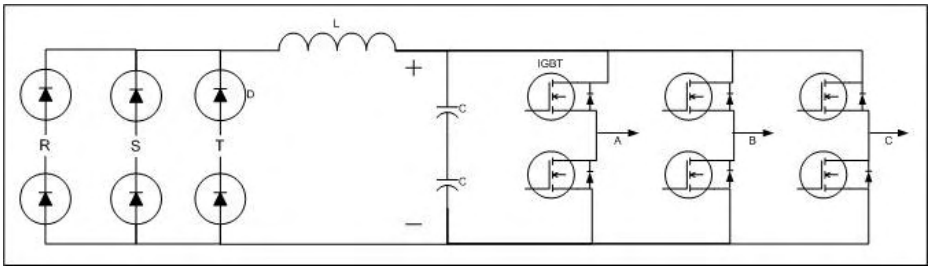

Figure 3-1 Circuit diagram of VFI

Because of the constraint that the input lines must never be shorted and the output current must be continuous a voltage fed inverter can assume in operation only eight distinct topologies. They are shown in Figure 3-2 and Figure 3-3. Six out of these eight topologies produce a non zero output voltage and are known as non-zero switching states and the remaining two topologies produce zero output and are known as zero switching state.

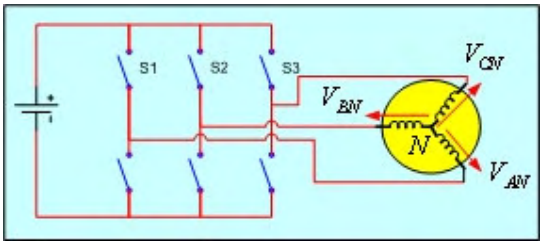

Figure 3-2 Three phase inverter with switching states

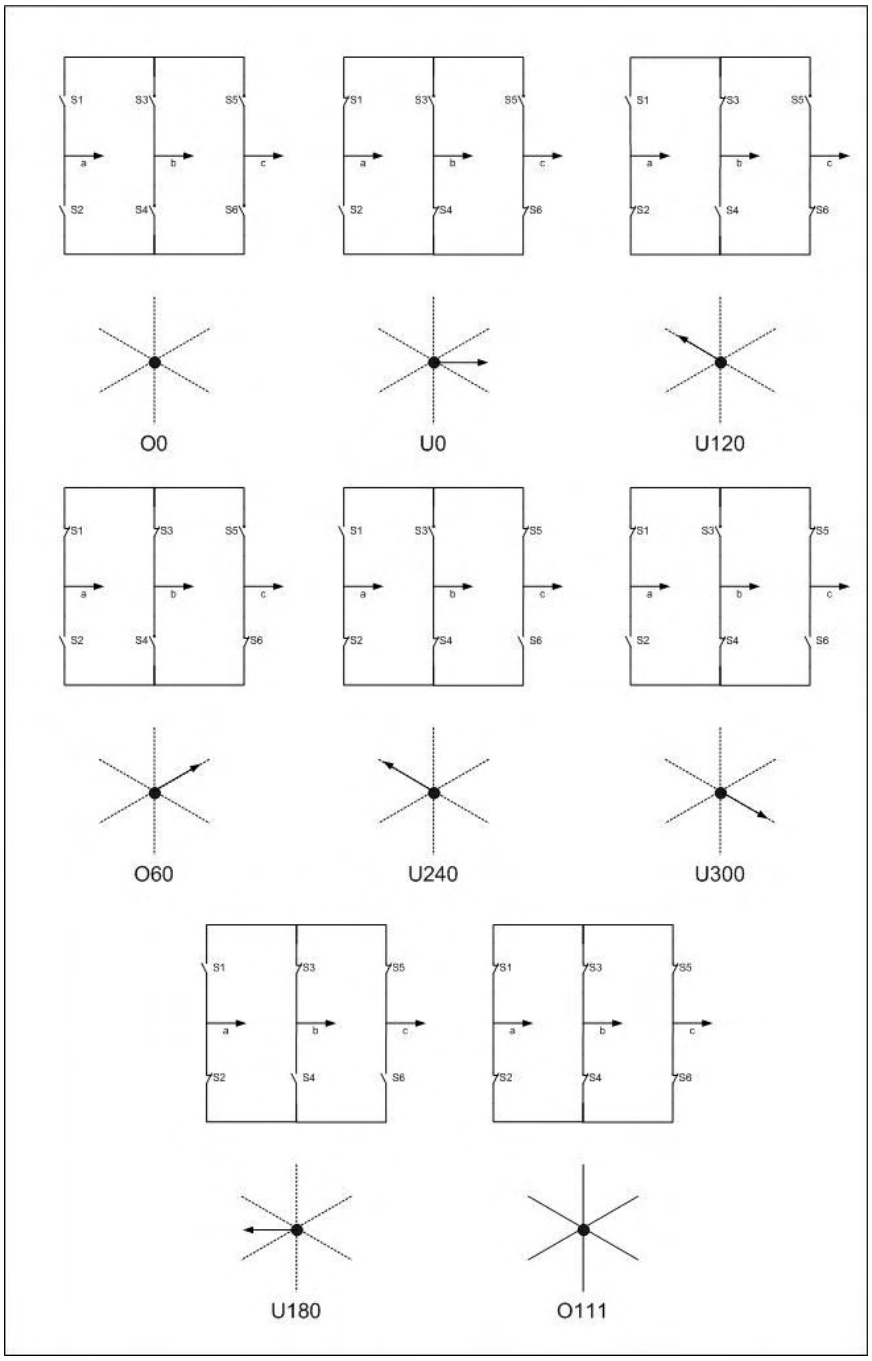

Figure 3-3 Eight switching state topologies of a voltage source inverter

3.2 Voltage Space Vectors

Space vector modulation for three leg VFI is based on the representation of the three phase quantities as vectors in two-dimensional (d^s-q^s) plane. Considering the first switching state in Figure 3-4, line-to-line voltages are given by:

Vab = Vs
Vbc = 0
Vca = -Vs

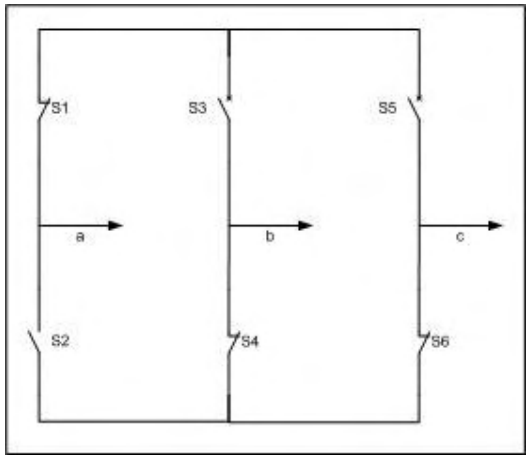

Figure 3-4 First switching state –V1

This can be represented in (d^s-q^s) plane as shown in Figure 3-5 where Vab, Vbc and Vca are the three line voltage vectors displaced 120° in space. The effective voltage vector generated by this topology is represented as V1 (pnn) in Figure 3-5. Here (pnn) refers to the three leg /phases a, b, c being either connected to the positive dc rail (p) or to the negative dc rail (n). For the first switching state V1, phase a connected to positive dc rail and phases b and c are connected to negative dc rail. Similar to the V1, six non zero voltage vectors can be shown as in Figure 3-6. The tips of these vectors form a regular hexagon. We define the area enclosed by two adjacent vectors, within the hexagon, as a sector.

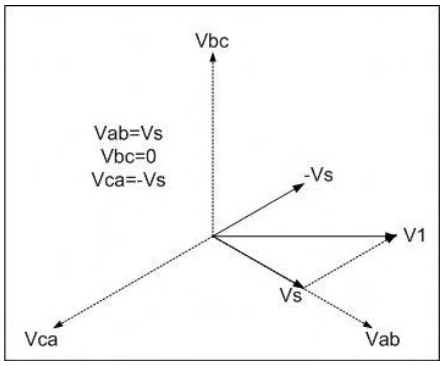

Figure 3-5 Representation of topology 1 in (d^s-q^s) plane

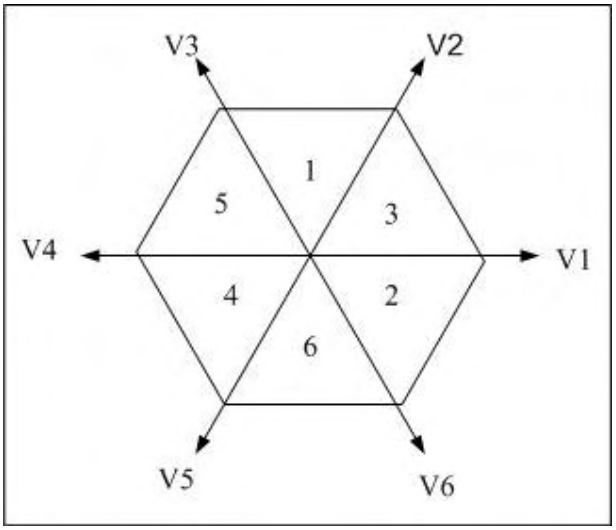

Figure 3-6 Non-zero voltage vectors in (d^s-q^s) plane

The first and the last two topologies of Figure 3-3 are zero state vectors. The output line voltages in these topologies are zero.

Vab=0

Vbc=0

Vca=0

These are represented as vectors which have zero magnitude and hence are referred as zero switching state vectors. They are represented with dot at the origin instead of vectors as shown in Figure 3-7.

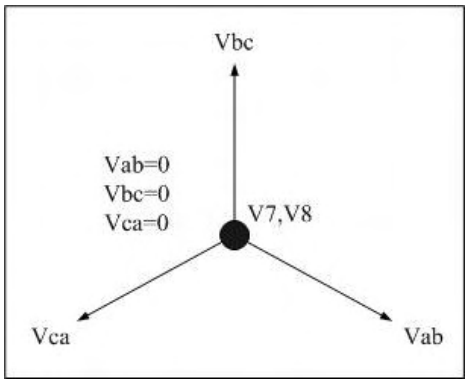

Figure 3-7 Representation of the zero voltage vectors in (d^s-q^s) plane

3.2.1 SVPWM Application to the Static Power Bridge and Implementation Using DSP Platform

In the case of AC drive applications, sinusoidal voltage sources are not used as explained before. Instead, they are replaced by 6 power IGBTs which act as on/off switches to the rectified DC bus voltage. The aim is to create sinusoidal current in the windings to generate rotating field. Owing to the inductive nature of the phases, a pseudo sinusoidal current is created by modulating the duty-cycle of the power switches. The switches (IGBT) shown in the Figure 3-2 are activated by signals (a, b, c) and their complement values. Eight different combinations are available with this three phase VFI including two zero states. It is possible to express each phase to neutral voltages, for every switching combinations of IGBT's as listed in Table 3-1.

Table 3-1 Power Bridge Output Voltages (V_{AN}, V_{BN}, V_{CN})

Switch Positions			Phase Voltages		
S1	**S2**	**S3**	**V_{AN}**	**V_{BN}**	**V_{CN}**
0	0	0	0	0	0
0	0	1	-Vdc/3	-Vdc/3	2Vdc/3
0	1	0	-Vdc/3	2Vdc/3	-Vdc/3
0	1	1	-2Vdc/3	Vdc/3	Vdc/3
1	0	0	2Vdc/3	-Vdc/3	-Vdc/3
1	0	1	Vdc/3	-2Vdc/3	Vdc/3
1	1	0	Vdc/3	Vdc/3	-2Vdc/3
1	1	1	0	0	0

In field oriented control algorithm, the control variables are expressed in rotating frame. The current vector Isref that directly controls the torque is transformed in a voltage vector by the inverse Park transform. This voltage reference is expressed in the (d^s-q^s) frame. Using this transformation three phase voltages (V_{AN}, V_{BN}, V_{CN}) and the reference voltage vector are projected in the (d^s-q^s) frame. The expression of the three phase voltages in the (d^s-q^s) frame are given by general Clarke transformation:

$$\begin{bmatrix} V_{sd}^{s} \\ V_{sq}^{s} \end{bmatrix} = \frac{2}{3}\begin{bmatrix} 1 & -\frac{1}{2} & -\frac{1}{2} \\ 0 & \frac{\sqrt{3}}{2} & -\frac{\sqrt{3}}{2} \end{bmatrix}\begin{bmatrix} V_{AN} \\ V_{BN} \\ V_{CN} \end{bmatrix} \tag{3.1}$$

Since only 8 combinations are possible for the power switches, V^s_{sd}, V^s_{sq} can also take finite number of values in the (d^s-q^s) frame (Table 3-2) according to the IGBT command signals (a, b, c).

Table 3-2 Stator Voltages in (d^s-q^s) frame and related Voltage Vector

Switch Positions			(d^s-q^s) frame Voltages		
S1	S2	S3	V^s_{sd}	V^s_{qs}	Vectors
0	0	0	0	0	V0
0	0	1	-Vdc/3	-Vdc/√3	V1
0	1	0	-Vdc/3	Vdc/√3	V2
0	1	1	-2Vdc/3	0	V3
1	0	0	2Vdc/3	0	V4
1	0	1	Vdc/3	-Vdc/√3	V5
1	1	0	Vdc/3	Vdc/√3	V6
1	1	1	0	0	V7

The eight voltage vectors re-defined by the combination of the switches are represented in Figure 3-8.

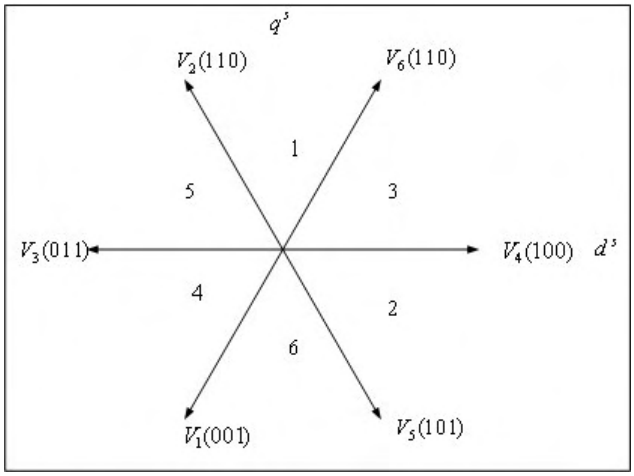

Figure 3-8 Voltage vectors

Given a reference voltage (coming from the inv. Park transform), the following step is used to approximate this reference voltage by the above defined eight vectors. The method used to approximate the desired stator reference voltage with only eight possible states of switches combines adjacent vectors of the reference voltage and modulates the time of application of each adjacent vector. In Figure 3-9, the reference voltage V_{sref} is in the third sector and the application time of each adjacent vector is given by:

$$T = T_4 + T_6 + T_0 \tag{3.2}$$

$$V_{sref} = \frac{T_4}{T}\vec{V}_4 + \frac{T_6}{T}\vec{V}_6$$

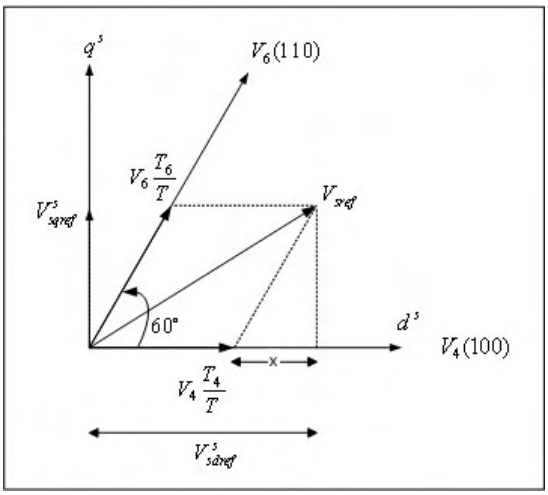

Figure 3-9 Projection of the reference voltage vector

The determination of the amount of times T_4 and T_6 is given by simple projections:

$$V_{sq}^{s} = \frac{T_6}{T}\left\|\vec{V}_6\right\|\cos(30^0)$$
$$V_{sd}^{s} = \frac{T_4}{T}\left\|\vec{V}_4\right\| + x \qquad (3.3)$$
$$x = \frac{V_{sq}^{s}}{tg(60^0)}$$

Finally, with the (d^s-q^s) component values of the vectors given in Table 3-2, the duration periods of application of each adjacent vector is:

$$T_4 = \frac{T}{2V_{dc}}(3V_{sd}^{s}\sqrt{3}V_{sq}^{s}) \qquad (3.4)$$

$$T_6 = \frac{T}{V_{dc}}\sqrt{3}V_{sq}^{s}) \qquad (3.5)$$

The rest of the period spent in applying the null vector (T_0=T-T_6-T_4). For every sector, commutation duration is calculated. The amount of times of vector application can all be related to the following variables:

$$X = \sqrt{3}V_{sq}^{s}$$
$$Y = \frac{\sqrt{3}}{2}V_{sq}^{s} + \frac{3}{2}V_{sd}^{s} \qquad (3.6)$$
$$Z = \frac{\sqrt{3}}{2}V_{sq}^{s} - \frac{3}{2}V_{sd}^{s}$$

In the previous example for sector 3, T4 = -Z and T_6 = X. Extending this logic, one can easily calculate the sector number belonging to the related reference voltage vector. The following basic algorithm helps to determine the sector systematically.

If X > 0 then A=1 else A=0

If Y > 0 then B=1 else B=0

If Z > 0 then C=1 else C=0

Sector = A+2B+4C

The duration of the sector boundary vectors application can be determined as follows:

sector

1: $t_1 = Z$ $t_2 = Y$

2: $t_1 = Y$ $t_2 = -X$

3: $t_1 = -Z$ $t_2 = X$

4: $t_1 = -X$ $t_2 = Z$

5: $t_1 = X$ $t_2 = -Y$

6: $t_1 = -Y$ $t_2 = -Z$

Saturations

If $(t_1 + t_2) > PWMPRD$ then

$t_{1sat} = (t_1 / t_1 + t_2) * PWMPRD$

$t_{2sat} = (t_2 / t_1 + t_2) * PWMPRD$

The third step is to compute the three necessary duty-cycles. This is shown below:

$$t_{aon} = \frac{PWMPRD - t_1 - t_2}{2}$$
$$t_{bon} = t_{aon} + t_1$$
$$t_{con} = t_{bon} + t_2$$

The last step is to assign the right duty-cycle (txon) to the right motor phase (in other words, to the right CMPRx) according to the sector. Table 3-3 below depicts this determination.

Table 3-3 Assigned duty cycles to the PWM outputs

	1	2	3	4	5	6
CMPR1	t_{bon}	t_{aon}	t_{aon}	t_{con}	t_{bon}	t_{con}
CMPR2	t_{aon}	t_{con}	t_{bon}	t_{bon}	t_{con}	t_{aon}
CMPR3	t_{con}	t_{bon}	t_{con}	t_{aon}	t_{aon}	t_{bon}

3.3 Simulation and Experimental Results of SVPWM

The SVPWM algorithm implemented in this thesis by DSP is simulated before proceeding through the experimental works to verify its results. In the first simulation, SVPWM algorithm is simulated step-by-step and all the software variables in the algorithm are compared with the experimental DSP program outputs. It is shown that both of the results are the same, and correct.

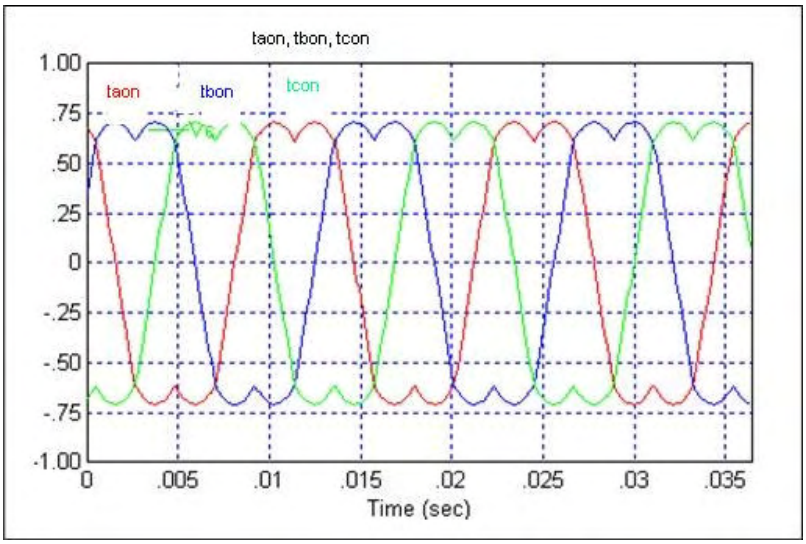

Figure 3-10 Simulated waveforms of duty cycles, (t_{aon}, t_{bon},t_{con})

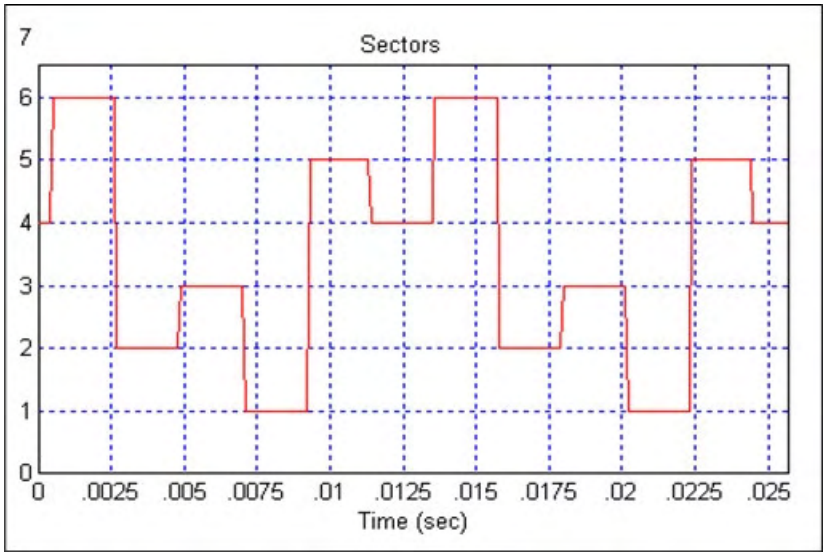

Figure 3-11 Sector numbers of voltage vector

In Figure 3-10 duty cycles of two PWM switches are shown (t_{aon}, t_{bon},t_{con}). In Figure 3-11 sector numbers of the rotating reference voltage vector is given. Note that the order of the sectors is the same as in Figure 3-11 of a vector rotating in counterclockwise direction in Figure 3-8 (sectors 3-1-5-4-6-2).

The experimental outputs confirm the theoretical and simulation outputs. Given two reference voltage vectors associated with the reference currents and

torque requirement, SVPWM software parameters are observed and compared with the simulated ones. The Figure 3-12 shows two phases outputs of SVPWM in a large time scale. When zoomed into Figure 3-12 as seen in Figure 3-13 one can see the symmetrical SVPWM in a small timescale. A SVPWM designer must check the correctness of the six PWM outputs generated by this SVPWM module. A simple low–pass filter RC circuit may be used to filter out the high frequency components. The R and C values (or the time-constant) are chosen for a desired cut–off frequency (fc) using the following equation:

Time-constant = RC = $1/2\pi f_c$

For example, R = 1.8 k. and C = 100 nF, gives fc = 884.2 Hz. This cut–off frequency has to be lower than the PWM frequency. This low–pass filter is connected to the PWM pins of the LF2407 EVM, the filtered version of the PWM signals are monitored by oscilloscope. The waveforms shown on the oscilloscope (Figure 3-14, Figure 3-15) should be the same as the one shown in Figure 3-10.

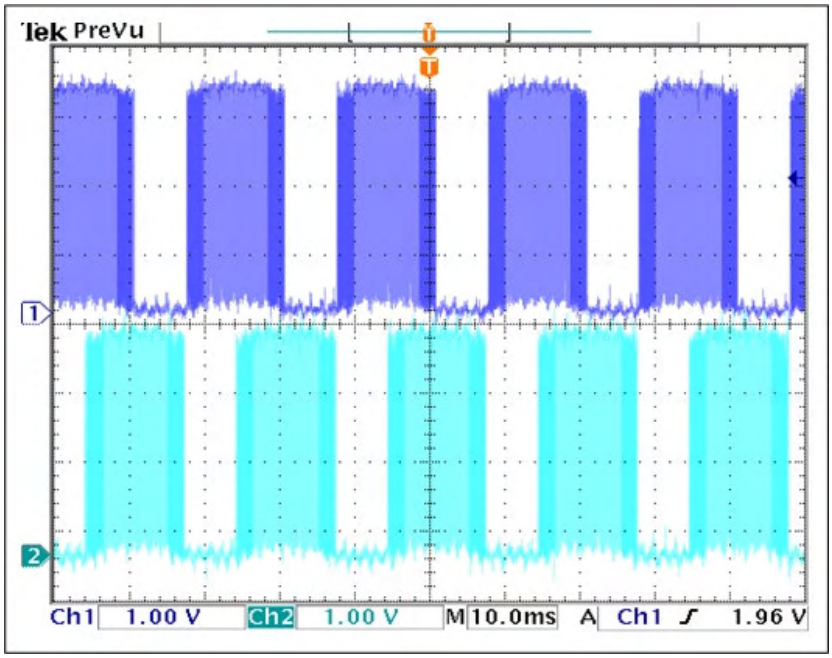

Figure 3-12 SVPWM outputs of two phases

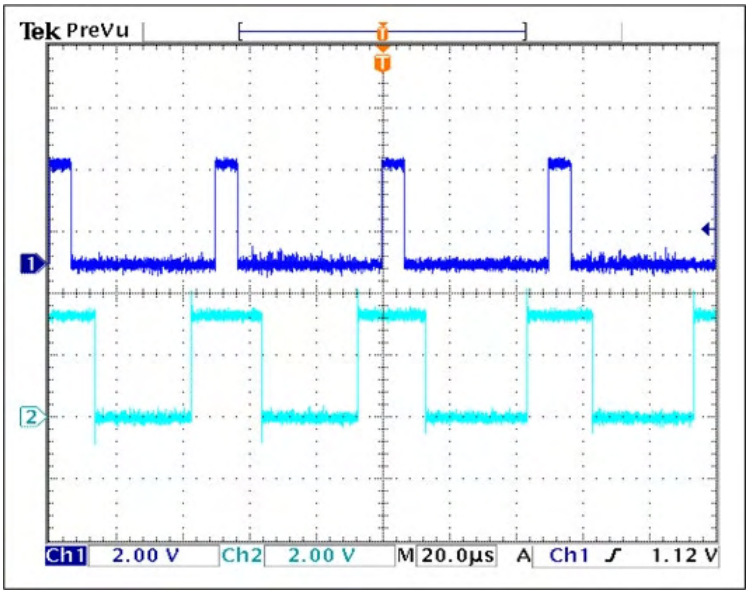

Figure 3-13 SVPWM outputs of two phases in small timescale

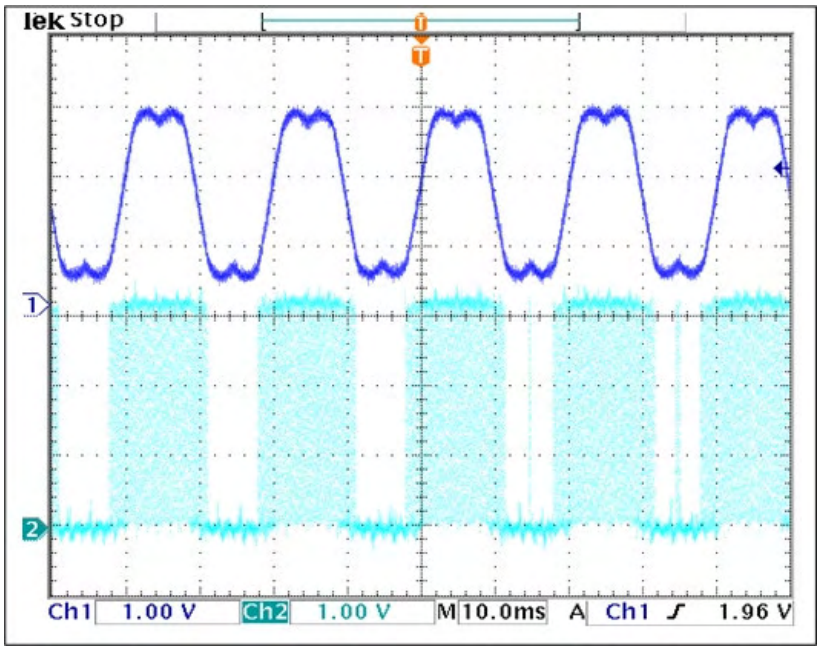

Figure 3-14 Low-pass filtered form of PWM1 pulses

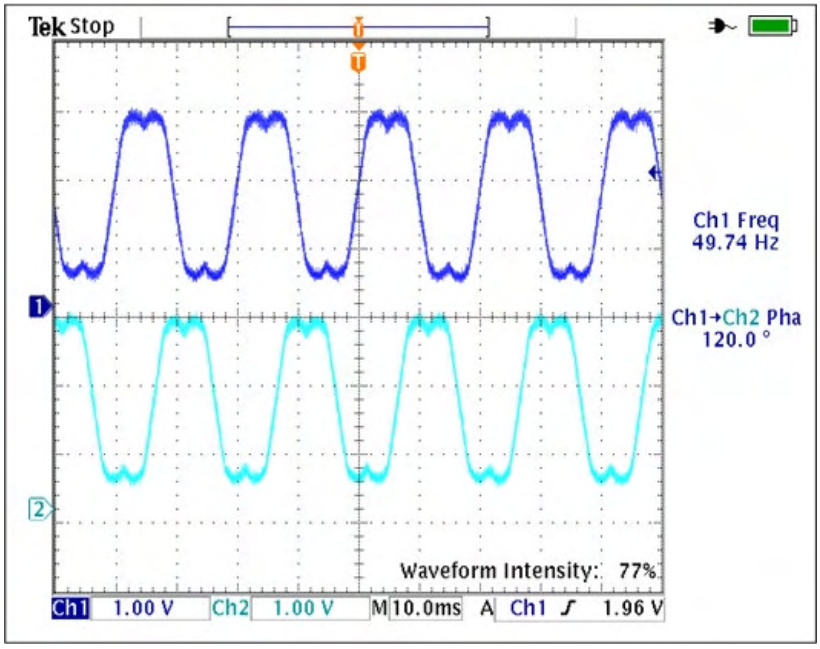

Figure 3-15 Low-pass filtered form of PWM1 and PWM5 pulses

4 FLUX AND SPEED ESTIMATION FOR SENSORLESS DIRECT FIELD ORIENTED CONTROL OF INDUCTION MACHINE

In this chapter, observers configured for direct field-orientation (DFO) are investigated. The field orientation is implemented in two ways as Direct Field Orientation and Indirect Field Orientation. The basic difference of these methods underlies in the manner of detecting the synchronous speed. In IFO, the slip angle is computed and added to the rotor speed to find the synchronous speed. One must calculate, therefore, the slip-angle and estimate the rotor angle. In the current model employed in the IFO, d-q axes stator currents and precise rotor time-constants are needed to find the slip angle. On the other hand, in DFO, the synchronous speed is computed from the ratio of dq-axes fluxes.

4.1 Flux Estimation

Flux estimator used in this chapter can compute both the synchronous speed and the rotor speed. The logic underlying this flux observer is basically an advanced voltage model approach in which integration of the back-emf is calculated and compensated for the errors associated with pure integrator and stator resistance R_s measurement at low speeds. At high speeds, the voltage model provides an accurate stator flux estimate because the machine back emf dominates the measured terminal voltage. However, at low speeds, the stator IR drop becomes significant, causing the accuracy of the flux estimate to be sensitive to the estimated stator resistance. Due to this effect, at low excitation frequencies flux estimation based upon voltage model are generally not capable of achieving high dynamic performance at low speeds [12]. Consequences of these problems are compensated with the addition of a closed-loop in the flux observer. Basically, the fluxes obtained by current model are compared

with those obtained by the voltage model with reference to the current model, or the current model with reference to the voltage model according to the range in which one of these models is superior to other [23]. In this flux observer the voltage model is corrected by the current model through a basic PI block. In the end, the stator fluxes are used to obtain rotor fluxes and rotor flux angle. The overall observer structure is given below.

4.1.1 Estimation of the Flux Linkage Vector

Most of the sensorless control schemes rely directly or indirectly on the estimation of the stator flux linkage vector, ψ_s being defined as the time integral of the induced voltage,

$$\frac{d\psi^{s,v}}{dt} = u_s - R_s i_s + u_{off}, \psi_s(0) = \psi_{s0} \qquad (4\text{-}1)$$

where, u_{off} represents all disturbances such as offsets, unbalances and other errors present in the estimated induced emf. A major source of error in the emf is due to the changes in the model parameter R_s. The estimation of the flux vectors requires the integration of (4.1) in real-time. The integrator, however, will have an infinite gain at zero frequency, and the unavoidable offsets contained in the integrator input then make its output gradually drift away beyond limits.

4.1.1.1 Flux Estimation in Continuous Time

The rotor flux linkage dynamics in synchronously rotating reference frame ($w=w_e=w_{\psi r}$) being as;

$$\frac{d\psi_{dr}^{e,i}}{dt} = \frac{L_m}{\tau_r} i_{ds}^e - \frac{1}{\tau_r}\psi_{dr}^{e,i} + (w_e - w_r)\psi_{qr}^{e,i} \qquad (4\text{-}2)$$

$$\frac{d\psi_{qr}^{e,i}}{dt} = \frac{L_m}{\tau_r} i_{qs}^{e} - \frac{1}{\tau_r}\psi_{qr}^{e,i} + (w_e - w_r)\psi_{dr}^{e,i} \qquad (4\text{-}3)$$

where L_m is the magnetizing inductance (H), $\tau_r = L_r/R_r$ is the rotor time-constant (sec), and w_r is the electrical angular velocity of the rotor (rad/sec). In the current model, the total rotor flux-linkage is aligned with the d-axis component, and hence;

$$\psi_r^{e,i} = \psi_{dr}^{e,i}$$
$$\psi_{qr}^{e,i} = 0$$

Substitution of $\psi_{qr}=0$ into (4-2) and (4-3) yields the oriented rotor flux dynamics as;

$$\frac{d\psi_{dr}^{e,i}}{dt} = \frac{L_m}{\tau_r} i_{ds}^{e} - \frac{1}{\tau_r}\psi_{dr}^{e,i} \qquad (4\text{-}4)$$

$$\psi_{qr}^{e,i} = 0 \qquad (4\text{-}5)$$

Note that (4-4) and (4-5) are the commonly recognized forms of the rotor flux vector equations. When, the rotor flux linkages in (4-4) and (4-5) undergoes the inverse park transformation in the stationary reference frame the result becomes.

$$\psi_{dr}^{s,i} = \psi_{dr}^{e,i}\cos(\theta_{\psi_r}) - \psi_{qr}^{e,i}\sin(\theta_{\psi_r}) = \psi_{dr}^{e,i}\cos(\theta_{\psi_r}) \qquad (4\text{-}6)$$

$$\psi_{qr}^{s,i} = \psi_{qr}^{e,i}\cos(\theta_{\psi_r}) + \psi_{dr}^{e,i}\sin(\theta_{\psi_r}) = \psi_{dr}^{e,i}\sin(\theta_{\psi_r}) \qquad (4\text{-}7)$$

where $\theta\psi_r$ is the rotor flux angle (rad). The stator flux linkages in stationary reference frame are then computed using (4-6) and (4-7) as;

$$\psi_{ds}^{s,i} = L_s i_{ds}^{s} + L_m i_{dr}^{s} = \left(\frac{L_s L_r - L_m^2}{L_r}\right) i_{ds}^{s} + \frac{L_m}{L_r}\psi_{dr}^{s,i} \qquad (4\text{-}8)$$

$$\psi_{qs}^{s,i} = L\, i_{qs}^{s} + L_m i_{qr}^{s} = \left(\frac{L_s L_r - L_m^2}{L_r}\right) i_{qs}^{s} + \frac{L_m}{L_r}\psi_{qr}^{s,i} \qquad (4\text{-}9)$$

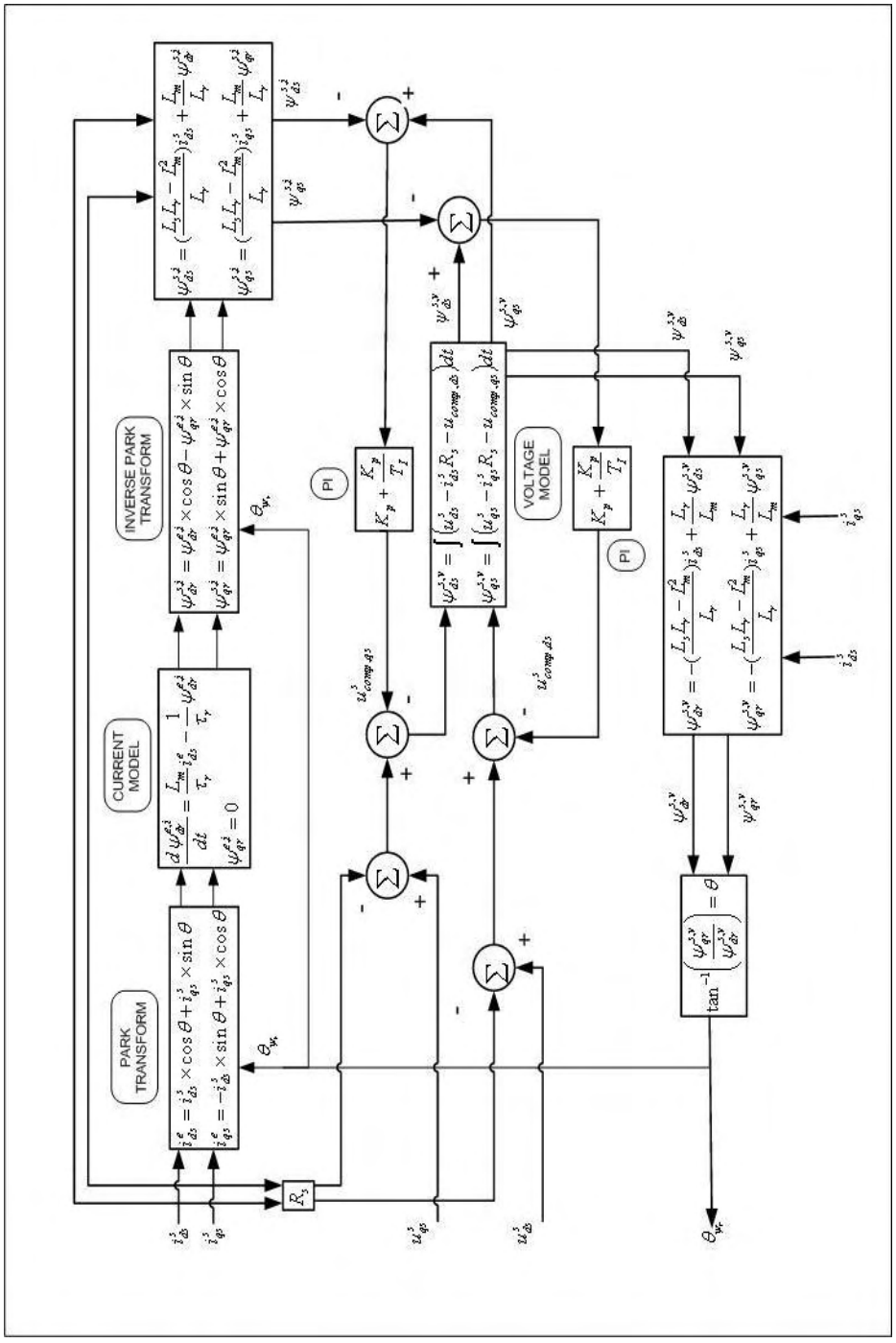

Figure 4-1 Flux estimation

The stator flux linkages in the voltage model, however, are computed by integrating the back emf's and compensated voltages taken into account.

$$\psi_{ds}^{s,v} = \int \left(u_{ds}^{s} - i_{ds}^{s} R_s - u_{comp,ds} \right) dt \tag{4-10}$$

$$\psi_{qs}^{s,v} = \int \left(u_{qs}^{s} - i_{qs}^{s} R_s - u_{comp,qs} \right) dt \tag{4-11}$$

The compensated voltages, on the otherhand, are computed by the PI control law as follows:

$$u_{comp,ds} = K_p \left(\psi_{ds}^{s,v} - \psi_{ds}^{s,i} \right) + \frac{K_p}{T_I} \int \left(\psi_{ds}^{s,v} - \psi_{ds}^{s,i} \right) dt \tag{4-12}$$

$$u_{comp,qs} = K_p \left(\psi_{qs}^{s,v} - \psi_{qs}^{s,i} \right) + \frac{K_p}{T_I} \int \left(\psi_{qs}^{s,v} - \psi_{qs}^{s,i} \right) dt \tag{4-13}$$

The proportional gain K_p and the reset time T_I are chosen such that the flux linkages computed by the current model becomes dominant at low speed. The reason for that is the back emfs computed by the voltage model result to be extremely low at this speed range (even zero for back emfs at zero speed). While the motor is running at high speed range, the flux linkages computed by voltage model becomes dominant over the flux linkage components computed through the current model.

Once the stator flux linkages in (4-10) and (4-11) are calculated, the rotor flux linkages based on the voltage model are computed once more through (4-14) and (4-15) which are only rearranged forms of (4-8) and (4-9), as

$$\psi_{dr}^{s,v} = -\left(\frac{L_s L_r - L_m^2}{L_m} \right) i_{ds}^{s} + \frac{L_r}{L_m} \psi_{ds}^{s,v} \tag{4-14}$$

$$\psi_{qr}^{s,v} = -\left(\frac{L_s L_r - L_m^2}{L_m}\right) i_{qs}^{s} + \frac{L_r}{L_m}\psi_{qs}^{s,v} \tag{4-15}$$

It is then a straight process to compute the rotor flux angle based on the voltage model as;

$$\theta_{\psi_r} = \tan^{-1}\left(\frac{\psi_{qr}^{s,v}}{\psi_{dr}^{s,v}}\right) \tag{4-16}$$

4.1.1.2 Flux Estimation in Discrete Time

The oriented rotor flux dynamics in (4-4) is discretized by using backward approximation as:

$$\frac{\psi_{dr}^{e,i}(k) - \psi_{dr}^{e,i}(k-1)}{T} = \frac{L_m}{\tau_r} i_{ds}^{e}(k) - \frac{1}{\tau_r}\psi_{dr}^{e,i}(k) \tag{4-17}$$

where T being the sampling period (sec). When rearranged (4-17) gives

$$\psi_{dr}^{e,i}(k) = \frac{\tau_r}{\tau_r + T}\psi_{dr}^{e,i}(k-1) - \frac{L_m \times T}{\tau_r + T} i_{ds}^{e}(k) \tag{4-18}$$

The stator flux linkages in (4-10) and (4-11)) are discretized by using trapezoidal approximation as;

$$\psi_{ds}^{s,v}(k) = \psi_{ds}^{s,v}(k-1) + \frac{T}{2}(e_{ds}^{s}(k) - e_{ds}^{s}(k-1)) \tag{4-19}$$

$$\psi_{qs}^{s,v}(k) = \psi_{qs}^{s,v}(k-1) + \frac{T}{2}(e_{qs}^{s}(k) - e_{qs}^{s}(k-1)) \tag{4-20}$$

where the back emf's are computed as;

$$e_{ds}^{s}(k) = u_{ds}^{s}(k) - i_{ds}^{s}(k)R_s - u_{comp,ds}^{s}(k) \tag{4-21}$$

$$e_{qs}^{s}(k) = u_{qs}^{s}(k) - i_{qs}^{s}(k)R_s - u_{comp,qs}^{s}(k) \tag{4-22}$$

Similarly, the PI control laws in (4-12) and (4-13) are also discretized by using trapezoidal approximation as

$$u_{comp,ds}(k) = K_p(\psi_{ds}^{s,v}(k) - \psi_{ds}^{s,i}(k)) + u_{comp,ds,i}(k-1) \tag{4-23}$$

$$u_{comp,qs}(k) = K_p(\psi_{qs}^{s,v}(k) - \psi_{qs}^{s,i}(k)) + u_{comp,qs,i}(k-1) \tag{4-24}$$

where the accumulating integral terms are;

$$\begin{aligned} u_{comp,ds,i}(k) &= u_{comp,ds,i}(k-1) + \frac{K_p T}{T_I}(\psi_{ds}^{s,v}(k) - \psi_{ds}^{s,i}(k)) \\ &= u_{comp,ds,i}(k-1) + K_p K_I(\psi_{ds}^{s,v}(k) - \psi_{ds}^{s,i}(k) \end{aligned} \tag{4-25}$$

$$\begin{aligned} u_{comp,qs,i}(k) &= u_{comp,qs,i}(k-1) + \frac{K_p T}{T_I}(\psi_{qs}^{s,v}(k) - \psi_{qs}^{s,i}(k)) \\ &= u_{comp,qs,i}(k-1) + K_p K_I(\psi_{qs}^{s,v}(k) - \psi_{qs}^{s,i}(k) \end{aligned} \tag{4-26}$$

with $K_I=T/T_I$.

4.1.1.3 Flux Estimation in Discrete Time and Per-Unit

All equations are needed to be normalized into per-unit by the specified base quantities. Firstly, the rotor flux linkage in current model (4-18) is normalized by dividing the base flux linkage as

$$\psi_{dr,pu}^{e,i}(k) = \frac{\tau_r}{\tau_r + T}\psi_{dr,pu}^{e,i}(k-1) - \frac{T}{\tau_r + T} i_{ds,pu}^{e}(k) \qquad (4\text{-}27)$$

where $\psi_B = L_m I_B$ is the base flux linkage (volt.sec) and I_b is the base current (amp). Next, the stator flux linkages in the current model (4-8) and (4-9) are similarly normalized by dividing the base flux linkage as

$$\psi_{ds,pu}^{s,i}(k) = \frac{L_s L_r - L_m^2}{L_s L_r} i_{ds,pu}^{s}(k) + \frac{L_m}{L_r}\psi_{dr,pu}^{s,i}(k) \qquad (4\text{-}28)$$

$$\psi_{qs,pu}^{s,i}(k) = \frac{L_s L_r - L_m^2}{L_s L_r} i_{qs,pu}^{s}(k) + \frac{L_m}{L_r}\psi_{qr,pu}^{s,i}(k) \qquad (4\text{-}29)$$

Then, the back emf's in (4-21) and (4-22) are normalized by dividing the base phase voltage V_B.

$$e_{ds,pu}^{s}(k) = u_{ds,pu}^{s}(k) - \frac{I_b R_s}{V_b} i_{ds,pu}^{s}(k) - u_{comp,ds,pu}^{s}(k) \qquad (4\text{-}30)$$

$$e_{qs,pu}^{s}(k) = u_{qs,pu}^{s}(k) - \frac{I_b R_s}{V_b} i_{qs,pu}^{s}(k) - u_{comp,qs,pu}^{s}(k) \qquad (4\text{-}31)$$

Next, the stator flux linkages in the voltage model (4-19) and (4-20) are divided by the base flux linkage.

$$\psi_{ds,pu}^{s,v}(k) = \psi_{ds,pu}^{s,v}(k-1) + \frac{V_b T}{L_m I_b}\left(\frac{e_{ds,pu}^{s}(k) + e_{ds,pu}^{s}(k-1)}{2}\right) \qquad (4\text{-}32)$$

$$\psi_{qs,pu}^{s,v}(k) = \psi_{qs,pu}^{s,v}(k-1) + \frac{V_b T}{L_m I_b}\left(\frac{e_{qs,pu}^{s}(k) + e_{qs,pu}^{s}(k-1)}{2}\right) \qquad (4\text{-}33)$$

Similar to (4-28) and (4-29) the normalized rotor flux linkages in the voltage model are:

$$\psi_{dr,pu}^{s,v}(k) = -\frac{L_s L_r - L_m^2}{L_m L_m} i_{ds,pu}^{s}(k) + \frac{L_r}{L_m} \psi_{ds,pu}^{s,v}(k) \qquad (4\text{-}34)$$

$$\psi_{qr,pu}^{s,v}(k) = -\frac{L_s L_r - L_m^2}{L_m L_m} i_{qs,pu}^{s}(k) + \frac{L_r}{L_m} \psi_{qs,pu}^{s,v}(k) \qquad (4\text{-}35)$$

In conclusion, the discrete-time, per-unit equations are rewritten in terms of constants.

The rotor flux linkages developed by the current model in synchronously rotating reference frame ($w=w_{\psi r}$) are:

$$\psi_{dr,pu}^{e,i}(k) = K_1 \psi_{dr,pu}^{e,i}(k-1) - K_2 i_{ds,pu}^{e}(k) \qquad (4\text{-}36)$$

where

$$K_1 = \frac{\tau_r}{\tau_r + T} \qquad (4\text{-}37)$$
$$K_2 = \frac{T}{\tau_r + T}$$

The rotor flux linkages developed by the current model in the stationary reference frame ($w=0$) are:

$$\psi_{ds,pu}^{s,i}(k) = K_4 i_{ds,pu}^{s}(k) + K_3 \psi_{dr,pu}^{s,i}(k) \qquad (4\text{-}38)$$

$$\psi_{qs,pu}^{s,i}(k) = K_4 i_{qs,pu}^{s}(k) + K_3 \psi_{qr,pu}^{s,i}(k) \qquad (4\text{-}39)$$

$$K_4 = \frac{L_s L_r - L_m^2}{L_s L_r} \qquad (4\text{-}40)$$
$$K_3 = \frac{L_m}{L_r}$$

The back emf's developed by the voltage model in the stationary reference frame (w=0) is

$$e^{s}_{ds,pu}(k) = u^{s}_{ds,pu}(k) - K_5 i^{s}_{ds,pu}(k) - u^{s}_{comp,ds,pu}(k) \qquad (4\text{-}41)$$

$$e^{s}_{qs,pu}(k) = u^{s}_{qs,pu}(k) - K_5 i^{s}_{qs,pu}(k) - u^{s}_{comp,qs,pu}(k) \qquad (4\text{-}42)$$

$$K_5 = \frac{I_b R_s}{V_b} \qquad (4\text{-}43)$$

The stator flux linkages developed by the voltage model in the stationary reference frame (w=0) are:

$$\psi^{s,v}_{ds,pu}(k) = \psi^{s,v}_{ds,pu}(k-1) + K_6\left(\frac{e^{s}_{ds,pu}(k) + e^{s}_{ds,pu}(k-1)}{2}\right) \qquad (4\text{-}44)$$

$$\psi^{s,v}_{qs,pu}(k) = \psi^{s,v}_{qs,pu}(k-1) + K_6\left(\frac{e^{s}_{qs,pu}(k) + e^{s}_{qs,pu}(k-1)}{2}\right) \qquad (4\text{-}45)$$

$$K_6 = \frac{V_b T}{L_m I_b} \qquad (4\text{-}46)$$

The rotor flux linkages developed by the voltage model in the stationary reference frame (w=0) are:

$$\psi^{s,v}_{dr,pu}(k) = -K_8 i^{s}_{ds,pu}(k) + K_7 \psi^{s,v}_{ds,pu}(k) \qquad (4\text{-}47)$$

$$K_8 = \frac{L_s L_r - L_m^2}{L_m L_m}$$
$$K_7 = \frac{L_r}{L_m} \qquad (4\text{-}48)$$

The rotor flux angle developed by the voltage model

$$\theta_{\psi r,pu}(k) = \frac{1}{2\pi}\tan^{-1}\left[\frac{\psi^{s,v}{}_{qr,pu}(k)}{\psi^{s,v}{}_{dr,pu}(k)}\right] \quad (4\text{-}49)$$

The rotor flux angle is computed by referring to a look-up table of 0°-45° entries. The required parameters for this module are summarized as follows:

- The machine Parameters:
- Stator resistance (R_s)
- Rotor resistance (R_r)
- Stator leakage inductance (L_{sl})
- Rotor leakage inductance (L_{rl})
- Magnetizing inductance (L_m)
- The based quantities:
- Base current (I_b)
- Base phase voltage (V_b)
- The sampling period
- Sampling period (T)

The stator self inductance is $L_s=L_{sl}+L_m$ and the rotor self inductance is $L_r=L_{rl}+L_m$.

4.2 Speed Estimation

In this section a speed observer for the 3-phase induction motor based upon its mathematical model is investigated. The estimator's accuracy relies heavily on knowledge of critical motor parameters. The open loop speed estimator employed in this FOC structure is a well-known method based on stationary reference frame. The structure of this algorithm is quite easy when compared to the advanced estimation techniques. The synchronous speed, w_e, can be easily calculated from the derivative of the rotor flux angle in (4-10).

$$\omega_e = \frac{d\theta_{\psi_r}}{dt} = \frac{d\left(\tan^{-1}\left(\frac{\psi_{qr}^s}{\psi_{dr}^s} \right) \right)}{dt}) \tag{4-50}$$

Note that (4-50) can be solved as

$$\frac{d(\tan^{-1} u)}{dt} = \frac{1}{1+u}\frac{du}{dt} \tag{4-51}$$

where $u = \frac{\psi_{qr}^s}{\psi_{dr}^s}$. The solution is then

$$\omega_e = \frac{d\theta_{\psi r}}{dt} = \frac{(\psi_{dr}^s)^2}{(\psi_r^s)^2}\left[\frac{\psi_{dr}^s \frac{d\psi_{qr}^s}{dt} - \psi_{qr}^s \frac{d\psi_{dr}^s}{dt}}{(\psi_{dr}^s)^2} \right] \tag{4-52}$$

Substituting (4-1) and (4-2) into (4-52), and a suitable rearrangement of them gives the synchronous speed, w_e as;

$$\omega_e = \frac{d\theta_{\psi r}}{dt} = \omega_r + \frac{1}{(\psi_r^s)^2}\frac{L_m}{\tau_r}\left[\psi_{dr}^s i_{qs}^s - \psi_{qr}^s i_{ds}^s\right] \tag{4-53}$$

The second term of the right hand in (4-53) is known as slip that is proportional to the electromagnetic torque when the rotor flux magnitude is maintaining constant. The electromagnetic torque can be shown here as;

$$T_e = \frac{3}{2}\frac{p}{2}\frac{L_m}{L_r}\left[\psi_{dr}^s i_{qs}^s - \psi_{qr}^s i_{ds}^s\right] \tag{4-54}$$

where p is the number of poles. Thus, the rotor speed can be found as

$$w_r = w_e - \frac{1}{(\psi_r^s)^2}\frac{L_m}{\tau_r}\left[\psi_{dr}^s i_{qs}^s - \psi_{qr}^s i_{ds}^s\right] \tag{4-55}$$

4.2.2 Speed Estimation in Discrete Time and Per-Unit

If the per-unit concept setforth here is applied to (4-55), then, the equation becomes

$$w_{r,pu} = w_{e,pu} - \frac{1}{w_b\ \tau_r}\left[\frac{\psi^s_{dr,pu} i^s_{qs,pu} - \psi^s_{qr,pu} i^s_{ds,pu}}{(\psi^s_{r,pu})^2}\right] \qquad (4\text{-}56)$$

where $w_b=2\pi f_b$ is the base electrical angular velocity (rad/sec), $\psi_b=L_m I_b$ is the base flux linkage (volt.sec), and I_b is the base current (amp). Equivalently, another form for (4-56) is

$$w_{r,pu} = w_{e,pu} - K_1\left[\frac{\psi^s_{dr,pu} i^s_{qs,pu} - \psi^s_{qr,pu} i^s_{ds,pu}}{(\psi^s_{r,pu})^2}\right] \qquad (4\text{-}57)$$

where $K1 = \dfrac{1}{w_b \tau_r}$.

The per-unit synchronous speed can be calculated as

$$w_{e,pu} = \frac{1}{2\pi f_b}\frac{d\theta_{\psi_{r,pu}}}{dt} = \frac{1}{f_b} w_{e,pu}\frac{d\theta_{\psi_{r,pu}}}{dt} \qquad (4\text{-}58)$$

where f_b is the base electrical (supply) frequency (Hz) and 2π is the base angle (rad). Discretizing (4-58) by using backward approximation, yields

$$w_{e,pu}(k) = \frac{1}{f_b}\left(\frac{d\theta_{\psi_{r,pu}}(k) - d\theta_{\psi_{r,pu}}(k-1)}{T}\right) \qquad (4\text{-}59)$$

where T being the sampling period (sec). Equivalently, another form for (4-59) is

$$w_{e,pu}(k) = K_2(d\theta_{\psi_{r,pu}}(k) - d\theta_{\psi_{r,pu}}(k-1)) \qquad (4\text{-}60)$$

where $K_2=1/f_bT$ which is usually a large number.In practice, the typical waveforms of the rotor flux angle, $\theta_{\psi r,pu}$, in both directions can be seen in Figure 4-1. In order to take the discontinuity of angle from 360° to 0° (CCW) or from 0° to 360° (CW) into account, the differentiator is simply operated only within the differentiable range as seen in this figure. This differentiable range does not cause significant loss of information to compute the estimated speed.

In addition, the synchronous speed in (4-60) is necessary to be filtered out by the low-pass filter in order to reduce the amplifying noise generated by the pure differentiator in (4-60). The simple 1st –order low-pass filter is used, then the

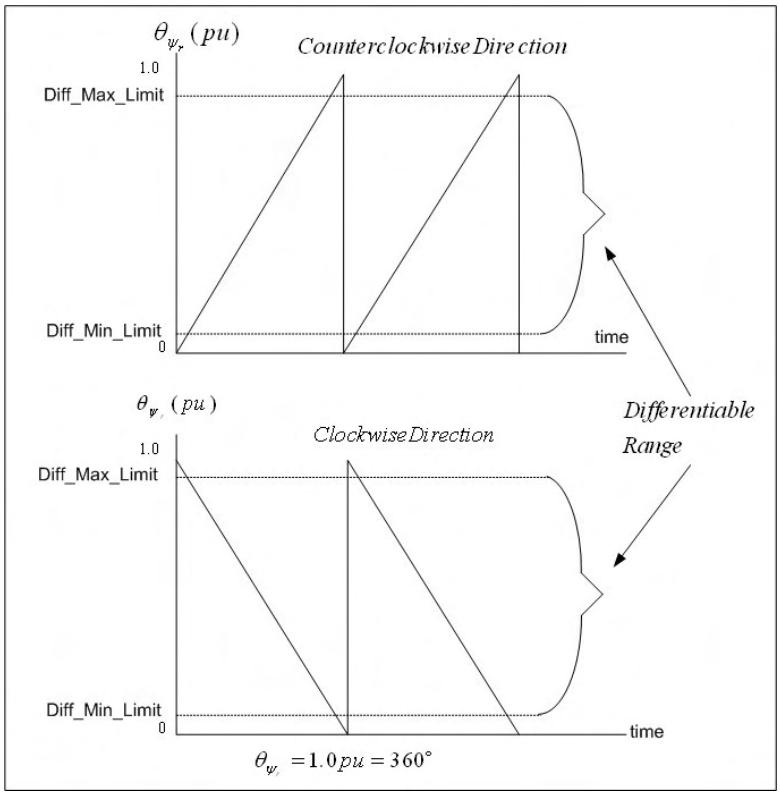

Figure 4-1 The waveforms of rotor flux angle in both directions

actual synchronous speed to be used is the output of the low-pass filter, w^*_{pu}, seen in (4-61). The continuous-time equation of 1st-order low-pass filter is as

$$\frac{dw^*_{e,pu}}{dt} = \frac{1}{\tau_c}(w_{e,pu} - w^*_{e,pu}) \qquad (4\text{-}61)$$

where $T_c=1/2\pi f_c$ is the low-pass filter time-constant (sec), and f_c is the cut-off frequency (Hz). Using backward approximation, then (4-61) becomes

$$w^*_{e,pu}\ (k) = K_3 w^*_{e,pu}\ (k-1) + K_4 w_{e,pu}(k) \qquad (4\text{-}62)$$

where $K_3=\tau_c/(\tau_c+T)$, and $K_4=T/(\tau_c+T)$.

As a result, only three equations (4-57), (4-60), and (4-62) are mainly employed to compute the estimated speed in per-unit. The required parameters for this method are summarized as follows:

- The machine parameters
- Number of poles (p)
- Rotor resistance (R_r)
- Rotor leakage resistance (L_{rl})
- Magneting inductance (L_m)
- The based quantities
- Base current (I_b)
- Base electrically angular velocity (w_b)
- The samling period (T)
- Low-pass filter
- Cut-off frequency
- Notice that the rotor self inductance is $L_{rl}+L_m$ (H)

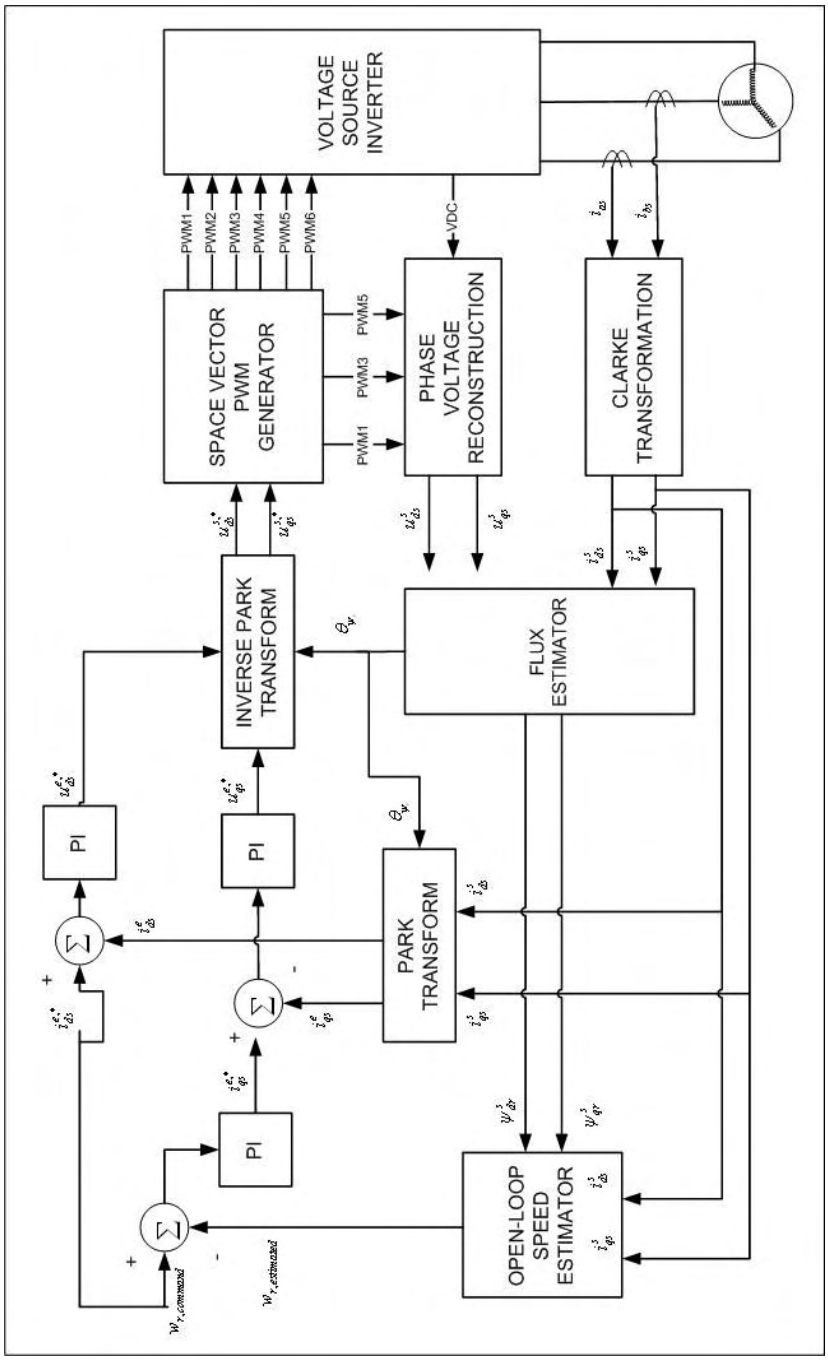

Figure 4-3 Overall algorithm of the flux and speed estimators

5 IMPLEMENTATION OF FLUX AND SPEED ESTIMATION FOR SENSORLESS DIRECT FIELD ORIENTATION

5.1 Simulation Results

Five different simulations were carried out to observe the effectiveness of the derived algorithms for the flux and speed estimation with MRAS scheme. In these simulations the PI regulators are tuned as to give a satisfactory speed response when parameter errors are absent. During the simulations all the parameters are kept constant in order to determine the bandwidth of the system. The simulation parameters used in the simulations are given in Table 5-1. The overall controller blocks are simulated in discrete-time in order to better reflect its implementation on a Digital Signal Processor.

Table 5-1 Simulation Parameters

Rotor resistance per phase	2.19 Ω
Stator resistance per phase	1.80 Ω
Stator leakage inductance per phase	0.192 H
Rotor leakage inductance per phase	0.192 H
Magnetizing inductance	0.184 H
Base line current	7.5 A
Base per phase voltage	220 V
Base torque	12.375 Nm
Base linkage flux	1.38 Vsec/rad
Base electrical angular velocity	400 rad/sec
Number of motor poles	4
Sampling frequency	0.0001 sec

5.1.1 Simulation 1- For No-Load Case

During this simulation the motor is rotated at no-load. The electrical speed command is increased to 0.4 pu that is equal to 1528 rpm (w_{base} = 400 rad/sec) from at rest. The reference rotating frame current component (i^e_d) is set to 0.6pu. The aim of this simulation is to understand the speed estimation accuracy when the torque command is zero. The Figure 5-1 shows the motor actual torque beside the commanded torque. In the first 0.1 sec the motor produces electromechanical torque nearly 1% of rated torque due to motor inertia. After that produced torque settles to its demanded value and is close to zero.

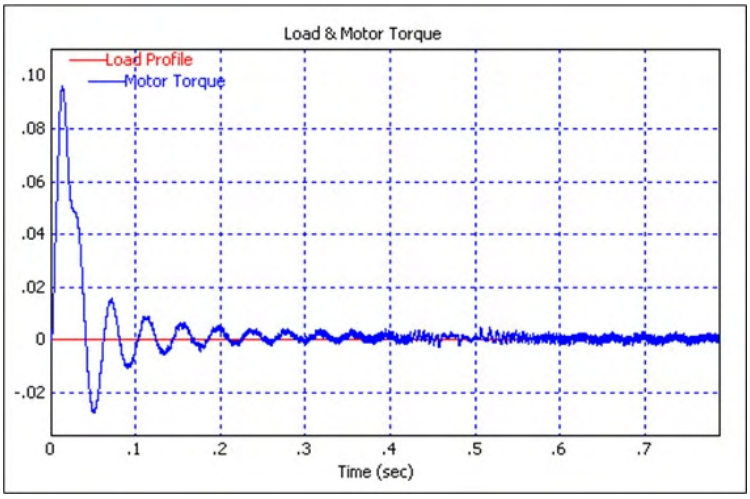

Figure 5-1 Motor torque at no-load

In

Figure 5-2 rotating frame currents, which are namely torque producing current component (i^e_q) and constant flux producing current component (i^e_d), are seen. As seen in the figure q^e-axis current component is proportional to the torque produced while the motor is accelerating. For constant flux operation, d^e-axis current remains constant as expected and therefore torque has no oscillations.

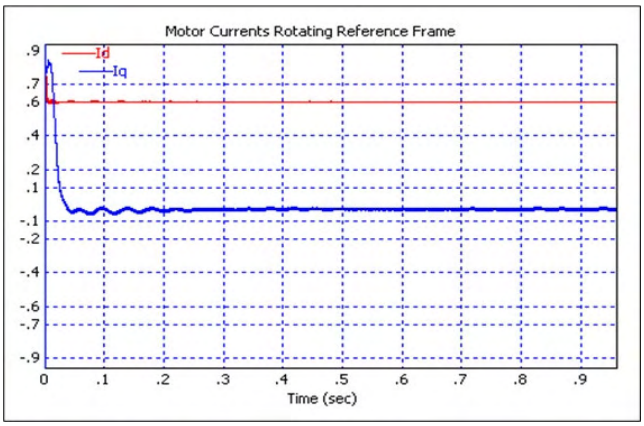

Figure 5-2 Motor currents (I_d, I_q) in rotating reference frame at no-load

The angle of rotor flux with respect to the stationary frame d^s-axis is estimated with the proposed flux observer. In the estimation process as a first step rotor flux linkages in rotating reference frame are found then the rotor flux angle estimation follows the calculation method given in section 4.1.1.1. Figure 5-3 shows the rotor flux angle in pu. One pu here means 2π rad/sec. Note on the graph that the time elapsed from zero angle to 1.0 pu angle is 0.041 sec. This valuable information gives us the synchronous speed. Because it says that rotor flux rotates at this speed with respect to the stationary d^s-axis. By this knowledge the rotating reference frame current components (for example i^e_d and i^e_q) can easily be transformed to stationary reference frame components (for example i^s_d and i^s_q) or vice versa.

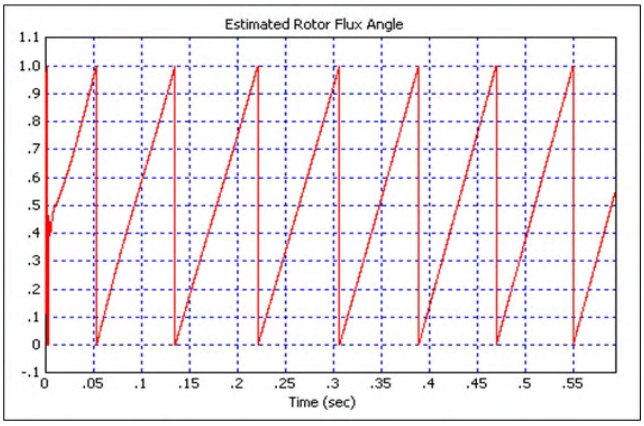

Figure 5-3 Estimated rotor flux angle at no-load

When the rotor flux angle is estimated once, synchronous speed and rotor speed can easily be calculated as given in section 4.2. Figure 5-4 shows the estimated and actual speed response of the system in the simulation against the set speed value. As it is seen here MRAS estimates the speed very close to the actual motor speed. The speed command in this simulation is 0.4 pu which corresponds to 160 rad/sec and 1528 rpm. The actual and estimated motor speeds are measured as 0.415 pu, 0.407 pu, respectively. This means that the speed error accuracy is less than 2.5%. Since there is no mechanical loading, there does not exist load disturbances and speed response is therefore quite smooth in time. In this simulation it can be seen that the settling time for the motor speed is nearly 1.4 seconds. The settling time may change for different systems according to system performance requirements. For sensorless algorithms and wide speed ranges it is acceptable in this study.

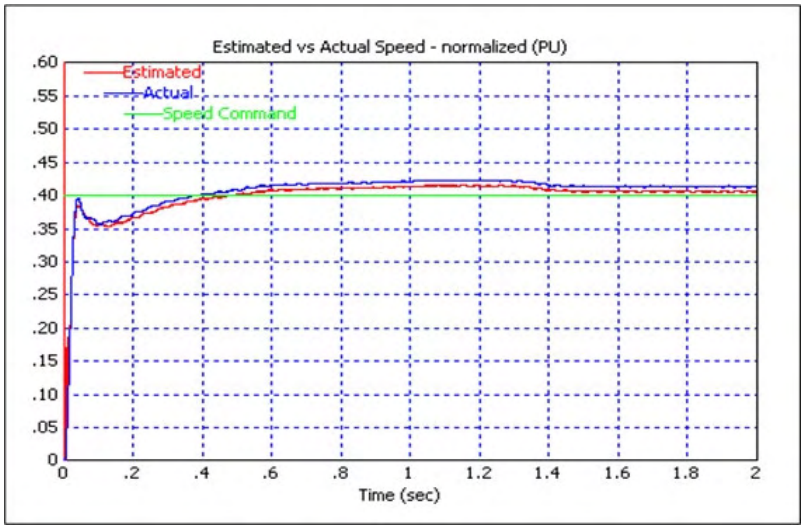

Figure 5-4 Speed command, motor estimated and actual speeds at no-load

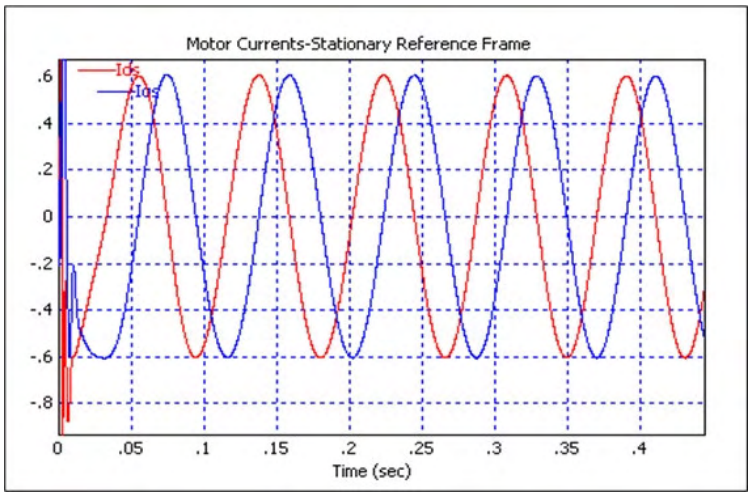

Figure 5-5 Currents (i^s_d and i^s_q) in stationary reference frame at no-load

Motor three-phase currents are transformed to two phase equivalents in orthogonal system in the machine model and they are shown in Figure 5-5. One can see from the figure frequency of the stationary frame currents (i^s_d and i^s_q) are the same as the rotor flux angle frequency. The amplitudes of the currents are equal to square root of the sum of squared values of i^e_d and i^e_q. Since the current i^e_q is equal to zero and the i^e_d is equal to 0.6 pu, the magnitude of the resultant current vector is also 0.6 pu. The phase angle between i^s_d and i^s_q is 90° as expected.

5.1.2 Simulation 2-For 0.5pu Loading

In this simulation the set speed value is the same as the first simulation (i.e. 0.4 pu.), but a step load torque of 0.5 pu is applied to the shaft of the motor 0.05 seconds later the simulation starts. The aim of this simulation is to see the motor performance when a mechanical torque is applied. At the beginning of the simulation, as in simulation 1, there is an electromechanical torque produced by the motor due to inertia of the motor. When the motor torque produced decays to zero, a load torque of 0.5 pu (Base Torque=12,375Nm) is applied to the shaft of the motor as a command. In Figure 5-6 it is shown that the motor torque settles to its stable point in 0.4 seconds following the loading and makes an overshoot of 1%, which is usually acceptable for many systems.

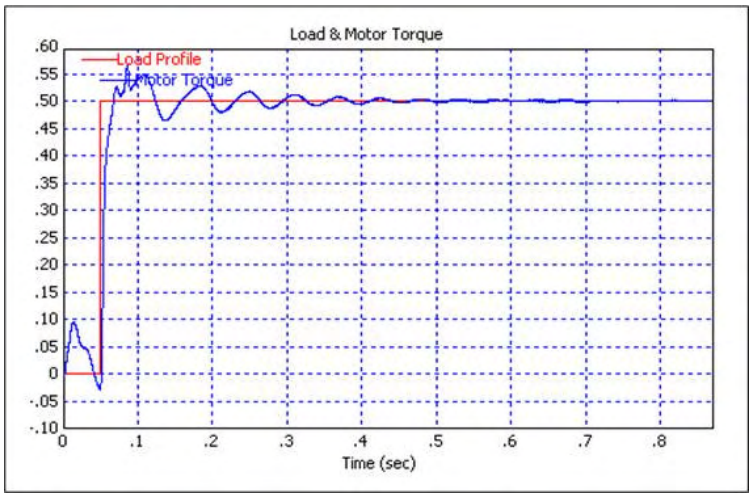

Figure 5-6 Motor torque at 0.5pu.loading

Upon application of the load torque to the shaft of the motor, PI controller just regulates the torque component of rotating frame current i^e_q in order to increase the motor produced torque so that the motor continues to run at the preset speed. Figure 5-7 shows the rotating current torque component i^e_q response for such a loading case. PI regulator regulates q^e-axis current i^e_q component of the rotating frame such that it settles to the value 0.5pu in 0.4 seconds. There is no difference in rotating flux component current of i^e_d, which is set to 0.6pu, for both of the simulations related to no-load and 0.5 pu torque loading cases. The graphs of the motor electromechanical torque and the current i^e_q are similar in nature. This shows us the controlling ac motor is just like a dc motor control. The constant flux component and the torque component of the currents can therefore be decoupled in ac motor control as well.

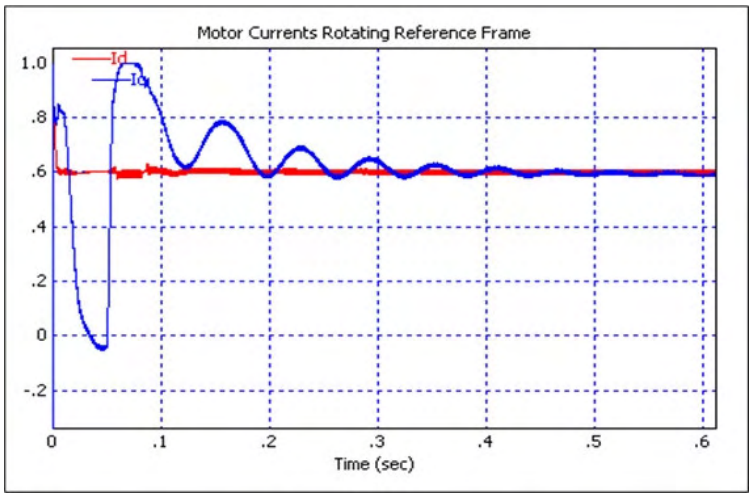

Figure 5-7 Motor currents i^e_d and i^e_q in rotating reference frame at 0.5pu loading

Figure 5-8 shows the estimated rotor flux angle at 0.5 pu loading. It is expected that the estimated rotor flux angle would come out very similar to one shown in simulation 1 (Figure 5-3), because the speed command is kept constant. But in Figure 5-8 the graph for the estimated rotor angle is distorted a little bit at the point where the torque command is applied to the shaft. It is due to the fact that sudden changes in torque component current i^e_q affect the other parameters given in rotor flux linkage dynamics. But the controller response is very fast that the estimated rotor flux angle settles to its value in 0.15 seconds.

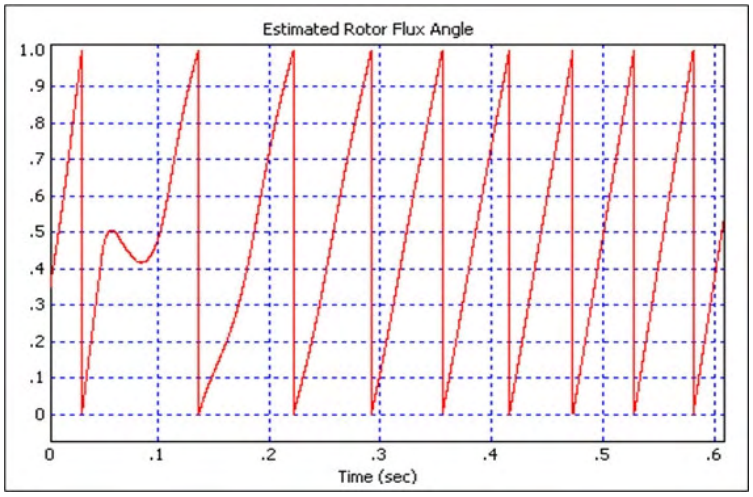

Figure 5-8 Estimated rotor flux angle at 0.5pu loading

Speed command, estimated and actual speeds are all shown in Figure 5-9. The settling time to the desired value for the motor speed increased with respect to that obtained in simulation 1 (Figure 5-4) due to applied torque. Due to the decrease in net torque needed for the acceleration, it takes more time for the motor to arrive at the same speed, as expected. To the contrary of difference resulting in the acceleration time, the error between the estimated and the actual speeds is the same with those came out in simulation 1.

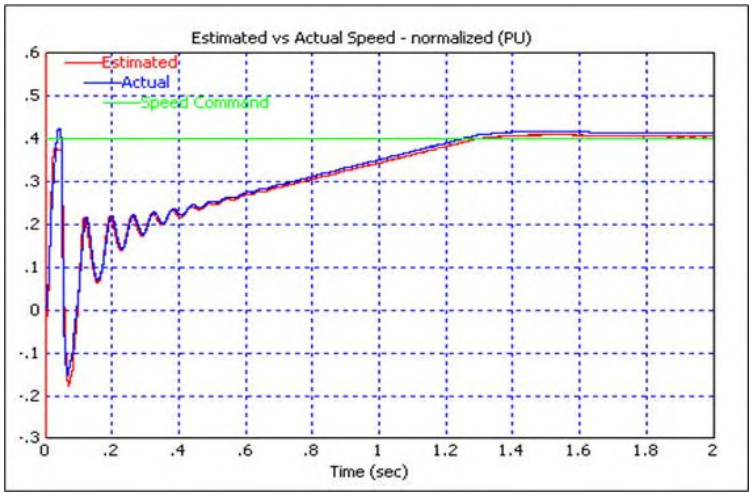

Figure 5-9 Speed command, motor estimated and actual speeds at 0.5pu. loading

5.1.3 Simulation 3-For 0.2pu and 0.3 pu Loading

In this simulation the set speed is also 0.4 pu. Torque command is increased from 0 to 0.2 pu. 0.5 seconds later from the instant of departure from the rest. Another 0.5 seconds later the torque command is further increased by 0.3 pu again. Thus, the torque command reached to a total value of 0.5 pu at the end. In this simulation rotating frame flux component current i^e_d is kept also constant. This simulation is done for understanding the controller and the motor behaviour when the torque command is increased in steps. The durations taken while accelerating to the desired speed value are investigated. Figure 5-10 shows the electromagnetic torque produced by the motor and the torque demand from it. Up to 0.5 sec the response of the motor is the same as that obtained in the first simulation (Figure 5-1). The motor

responds immediately to setting the torque to 0.2 pu and sets its developed torque to 0.2 pu in return. It complies to another step rise of the torque applied 0.5 seconds later as well.

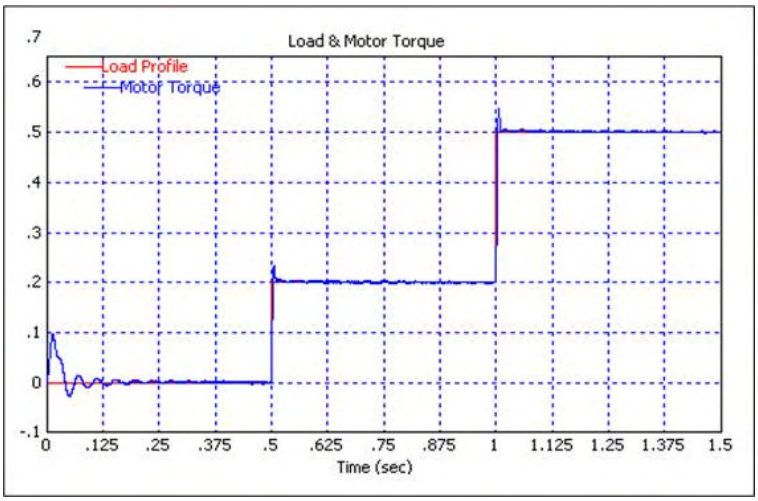

Figure 5-10 Motor torque at 0, 0.2 and 0.3 pu. loading

When a torque command is applied to the motor, it is expected that controller responds this demand by increasing the rotating frame torque component current i^e_q in proportion. The expected value for the flux component current i^e_d is the same as the previous value (0.6pu). The graphs of these currents are shown in Figure5-11. The value of the torque component current i^e_q following the application of both torque commands is equal to the one obtained in simulation 2 (Figure 5-7). This is an expected behaviour. The only but a minor difference noted in the figure is oscillations in i^e_q. These are transients left from the operation of the system prior to the application of the first torque command. The motor has not reached by then to steady-state yet, and it was still trying to overcome the effect of motor inertia.

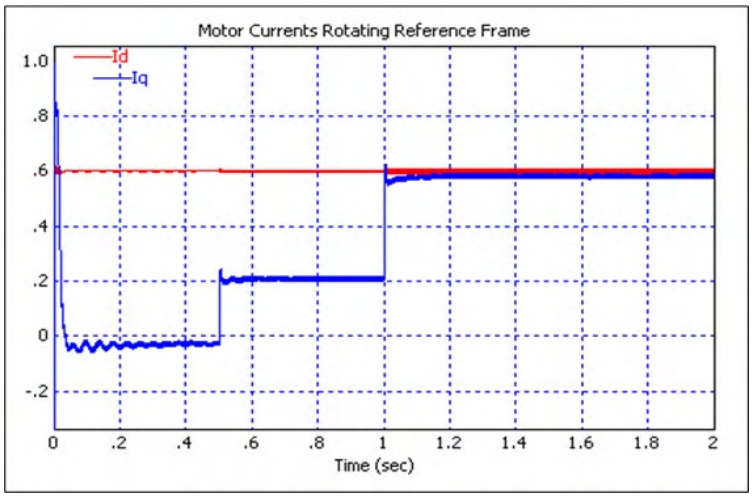

Figure 5-11 Motor currents i^e_d and i^e_q in rotating reference frame at 0.2 and 0.3 pu loading

As expected the rotor flux angle has not changed because, the speed command is being kept constant as previous. There are minor distortions at the points where the torque is being applied, but it does not affect over all system response and is skipped here.

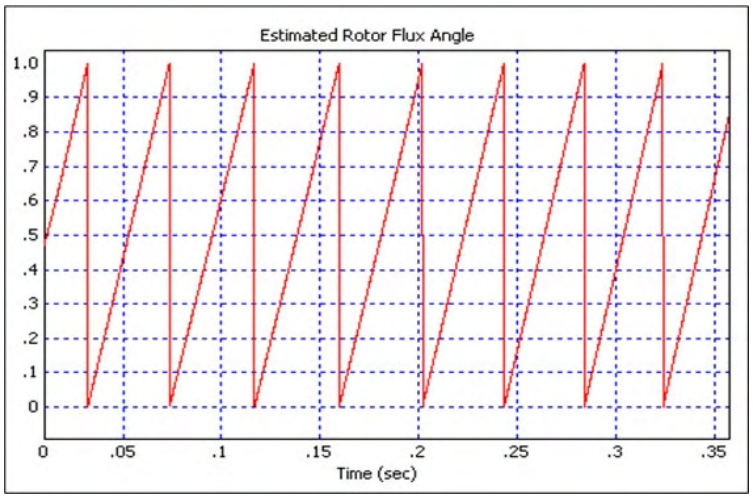

Figure 5-12 Estimated rotor flux angle at 0.2 and 0.3pu loading

From the estimated rotor flux angle the speed is estimated and shown together with the actual motor speed in Figure 5-13. At the point where the 0.2 pu torque is applied the actual and the estimated speeds deviate from the set point by approximately 15%,

and it takes them 0.2 seconds to settle to the set value. When the second torque command (0.3 pu) is applied to the motor the same kind of behaviour with the previous one is observed. The deviation this time is larger than the first one because of the presence of higher torque demand. This deviation reaches to 20% and 0.3 seconds is needed for settling. These deviations are normal should the motor dynamical model be considered. When a positive torque (in the same sense with the motor's own electromagnetic torque) is commanded at any time while the motor is rotating at a constant speed then the net torque will become negative. This forces the motor to decelerate immediately, but at that time the controller increases the torque component current i^e_q and the speed once again returns to its previous value.

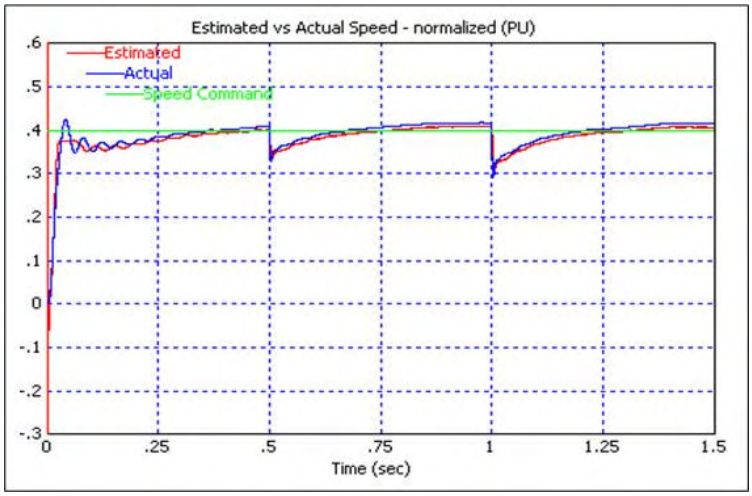

Figure 5-13 Speed command, motor estimated and actual speeds at 0, 0.2 and 0.3pu. loading

5.1.4 Simulation 4-Trapezoidal Loading

In this simulation the torque command is increased from 0.2 pu. to 0.4 pu in 0.5 seconds with a slope of 0.4 pu. The torque command is kept at that value for 0.5 seconds, and then it is decreased from 0.4 pu. to 0.2 pu again 0.5 seconds with a slope of -0.4 pu and kept at that value. The speed command is kept as 0.2 pu all the while. In this simulation the performance of the motor and the controller is investigated against the trapezoidal load profile. At the beginning of the simulation electromagnetic torque produced by the motor makes an overshoot due to the loading

and the motor inertia, then it tracks the torque command quite close as it is shown in Figure 5-14.

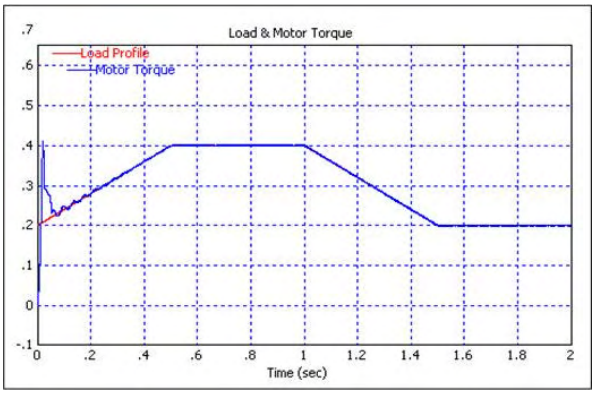

Figure 5-14 Motor torque at trapezoidal loading

As it is stated in the previous simulations motor rotating reference frame torque component current i^e_q is expected to behave similar to the one shown in torque graph. This current can be seen in Figure 5-15. The flux component current i^e_d is kept constant as before.

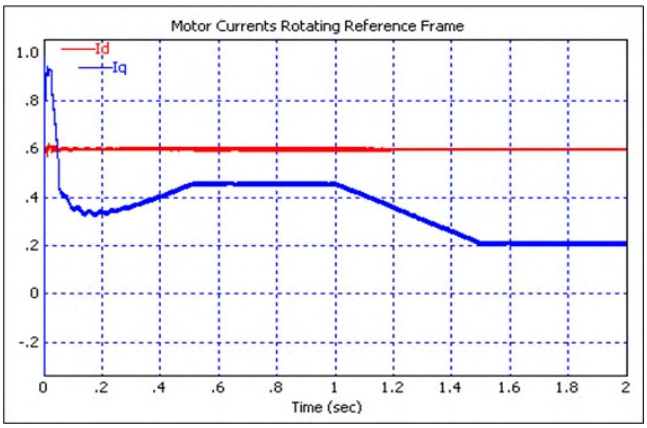

Figure 5-15 Motor currents (i^e_d and i^e_q) in rotating reference frame at trapezoidal loading

Estimated rotor flux should not show a different behaviour than those obtained in last 3 simulations, because the speed command is same for all of them. This is seen clearly at first sight in Figure 5-16.

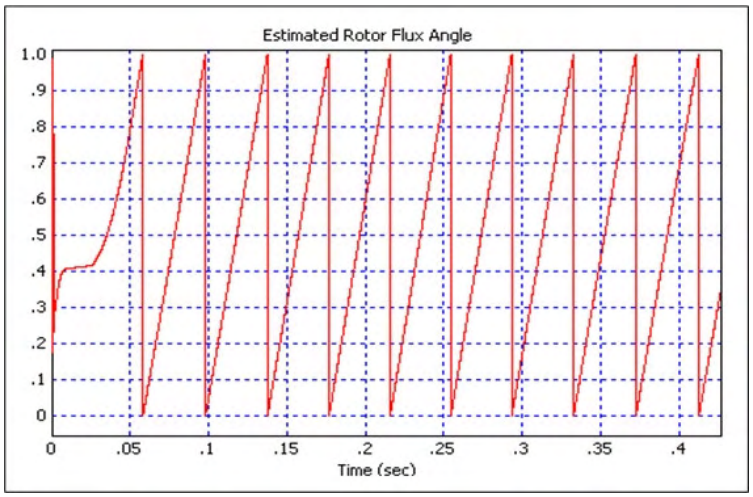

Figure 5-16 Estimated rotor flux angle at trapezoidal loading

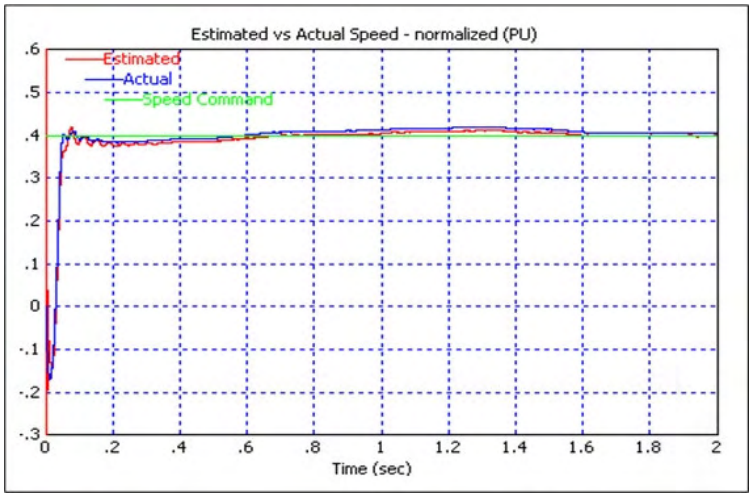

Figure 5-17 Speed command, motor estimated and actual speeds at trapezoidal loading

The estimated rotor flux angle having been determined, then the motor speed is estimated (Section 4.2) and it is shown in Figure 5-17. The motor performance is quite satisfactory during the load changes especially in regions where torque either increases or decreases. The speed remains almost constant as the torque varies.

5.1.5 Simulation 5-Trapezoidal Speed Command

In this simulation the speed command is increased from 0.2 pu. to 0.4 pu in 0.5 seconds with a slope of 0.4 pu. The speed command is kept at 0.4 pu for 0.5 seconds. Then it is decreased. to 0.2 pu in again 0.5 seconds with a slope of -0.4 and kept at that value. The torque command is kept as 0.3 pu all the while. There is a torque command at the beginning of the simulation and the motor tracks this command very nicely as shown in Figure 5-18. The motor rotating reference frame currents i^e_d and i^e_d behave similarly as the old ones and are not shown here to refrain from repetition.

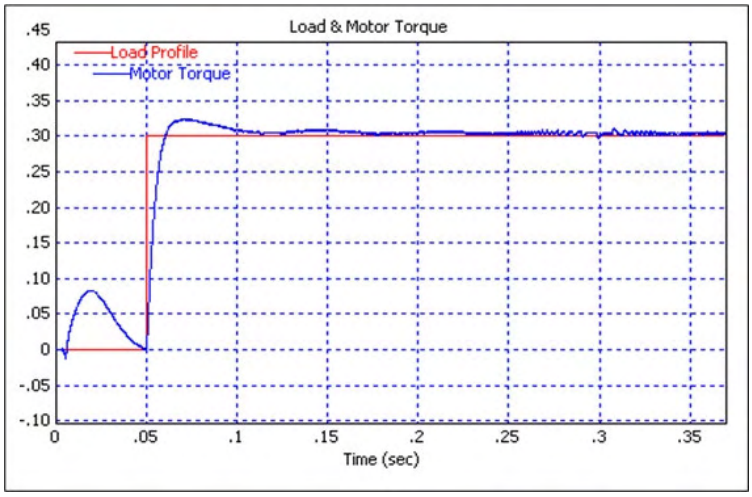

Figure 5-18 Motor torque at trapezoidal speed command

Estimated rotor flux angle has different characteristics than the earlier simulations. It is expected that with the changing speed commands the frequency of the applied voltages to motor should change together with the induced rotor flux linkage. This is shown in Figure 5-19. From the starting point to 0.5 seconds the frequency of the rotor flux angle increases linearly the frequency, however, does not change up to 1 seconds. After that it starts and continues to decrease linearly for a period of 0.5 seconds. The frequency is then kept constant.

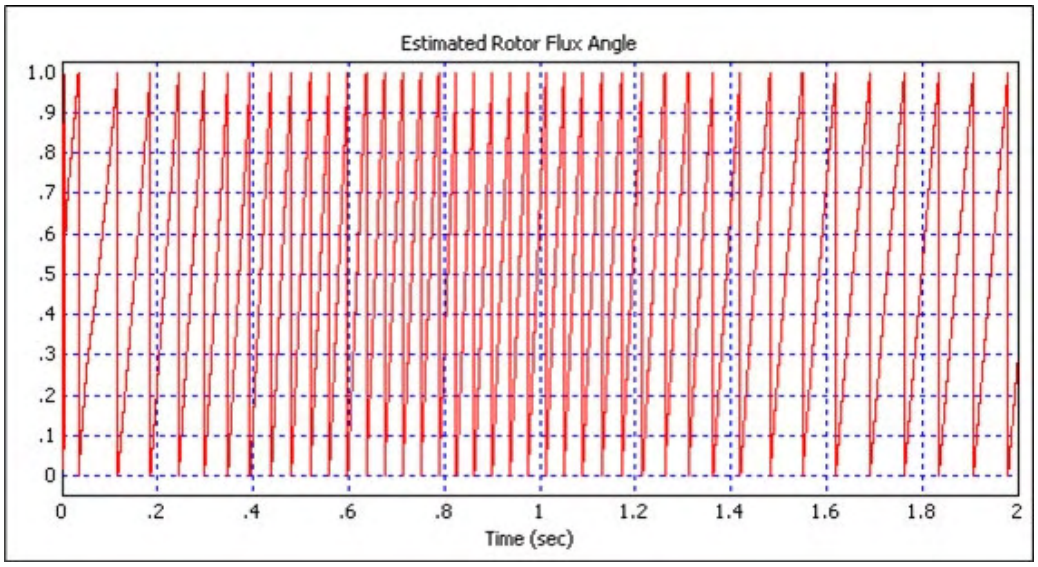

Figure 5-19 Estimated rotor flux angle at trapezoidal speed command

Once the rotor flux angle is estimated it is easy to estimate the speed. The set speed, the actual motor speed, and the estimated speed are altogether shown in Figure 5-20. Note that, the envelope of the motor actual speed and the estimated speed follow the speed command, the performance of the controller is not good. This is obviously due to the poorly selected PI parameters. In case the PI parameters and the constant flux component of rotating frame current i^e_d are still re-tuned for the case, the response of the motor speed can be improved. These parameters, however, are kept constant for all simulations and therefore such a tuning has not been done here in order not to change bases of comparison for the system behaviours under different loading conditions. The important point here we are after is the accuracy level achieved for the speed estimation. We note that the speed estimation error is less than 2%. The parameters can be re-tuned according to different system requirements.

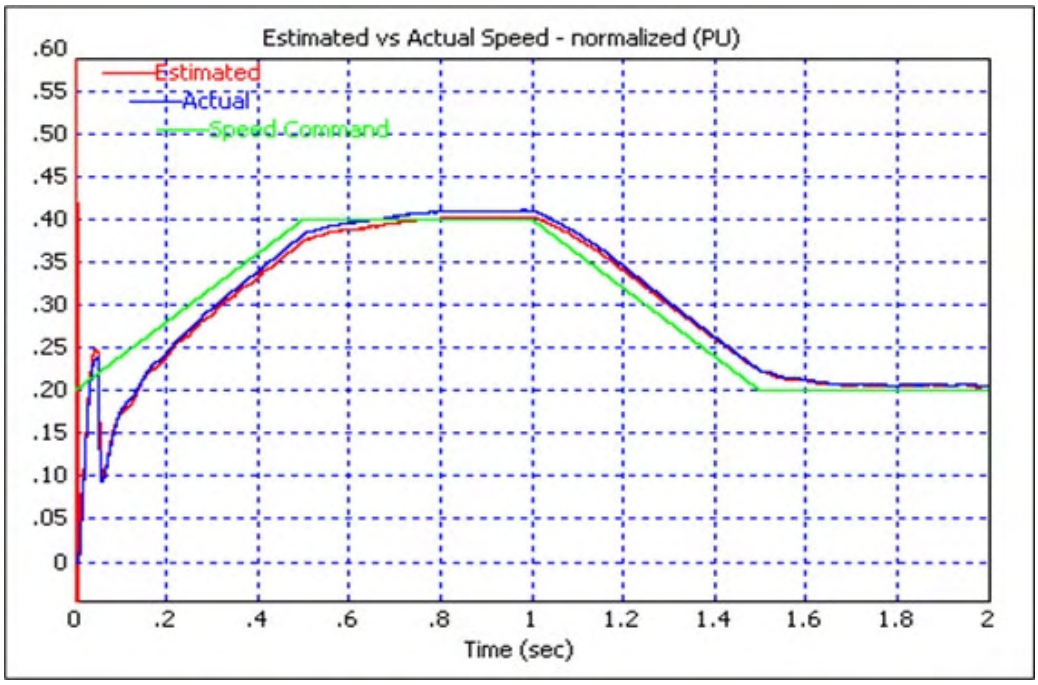

Figure 5-20 Speed command, motor estimated and actual speeds

at trapezoidal speed command

5.2 Experimental Results

5.2.1 Experimental Results-For no-load

The state estimator designed and implemented by using MRAS has been tested experimentally on the test setup following the simulations. The experimental data obtained in the tests involve the real time stator voltages and currents. These data are obtained through digital to analog converter block (LF2407 EVM) in the test setup. The stator currents and voltages come out quite close to pure sinusoidal waveform. This indicates that SVPWM approximates them quite precisely. Thus, the outputs of the flux estimator are expected to be sufficiently close to sinusoidal and the flux estimation results to be similarly precise enough for torque control operations. During the experiments in order to determine the flux and the speed estimator performance, the motor is operated in open-loop and the motor speed is measured with an additional hardware. Measured speeds are compared with the

estimated ones. Tests proved that the estimated speed and the supply frequency are linearly related. Estimated rotor flux angle is used in DSP algorithm for determining the speed. Estimated rotor flux angle is shown by the DAC of DSP evaluation board. The line currents together with the stationary axis currents i^s_d and i^s_q are also investigated during the tests.

The motor is first run at 10Hz and the estimated and actual rotor flux angles are recorded together. Trace 1(estimated) and trace 2 (actual) shown in Figure 5-21 represent the rotor flux angles with reference to the stator d^s-axis position. They change from 0 to 1pu (2π) as seen in the figure. The time taken for the rotor angle from zero to 1 shows the full period for the synchronous frequency as 100 msec. The figure shows clearly the close similarity between the estimated rotor flux angle and the actual angle. The line current recorded in the test as trace 4 is close to sinusoidal in shape at 10Hz.

The motor is next run at 20Hz. The results are shown in Figure 5-22. Note on the figure that trace 1(estimated rotor flux angle) is almost the same as trace 2 (actual rotor flux angle) indicating that the rotor flux angle is estimated correctly. The frequencies of both graphs are 20Hz as seen. The line current shown as trace 4 is close to sinusoidal in shape.

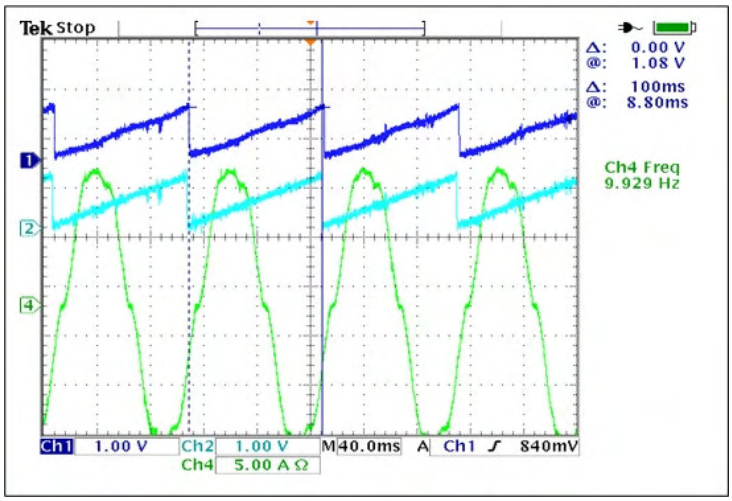

Figure 5-21 Ch1 Estimated rotor flux angle, ch2 actual rotor flux angle, ch4 line current at 10Hz supply frequency

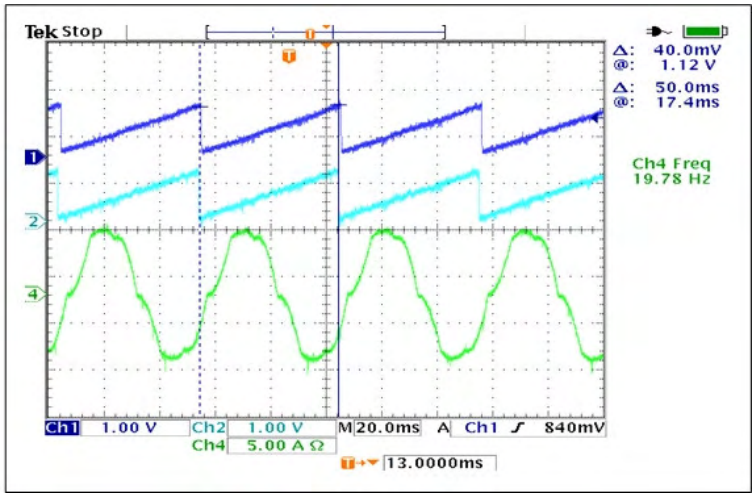

Figure 5-22 Ch1 Estimated rotor flux angle, ch2 actual rotor flux angle, ch4 line current at 20Hz supply frequency

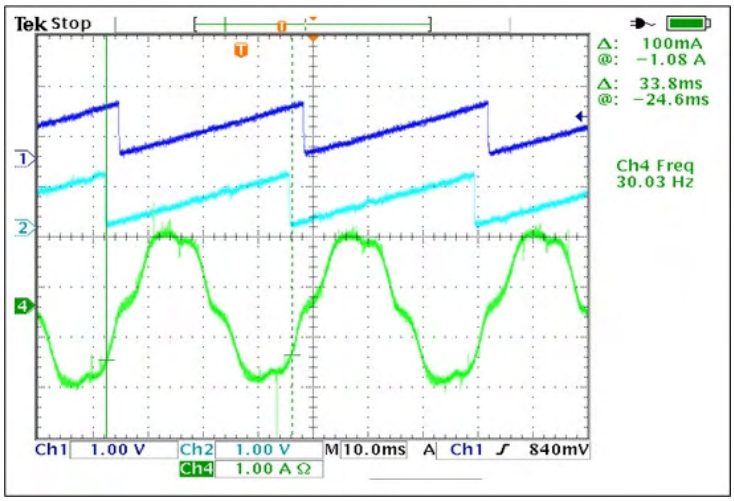

Figure 5-23 Ch1 Estimated rotor flux angle, ch2 actual rotor flux angle, ch4 line current at 30Hz supply frequency

In the third test the supply frequency is increased to 30Hz. This time the rotor flux angle is estimated with a delay of 2 msec. This delay is due to the time taken by the calculations running in DSP (i.e. the sampling time of DSP), and the hardware itself such as the delays caused by the sallen-key filters etc. This time delay can be decreased by using faster hardware and increasing DSP sampling rate. As seen in Figure 5-23 the line current of the motor as trace 4 is again close to sinusoidal.

The motor is tested under the supply frequency of 40Hz as a last case. The same problem met in case three arises in estimating the rotor flux angle. Figure 5-24 shows the estimated and actual rotor flux angles with the line current waveform at the same frequency with the supply.

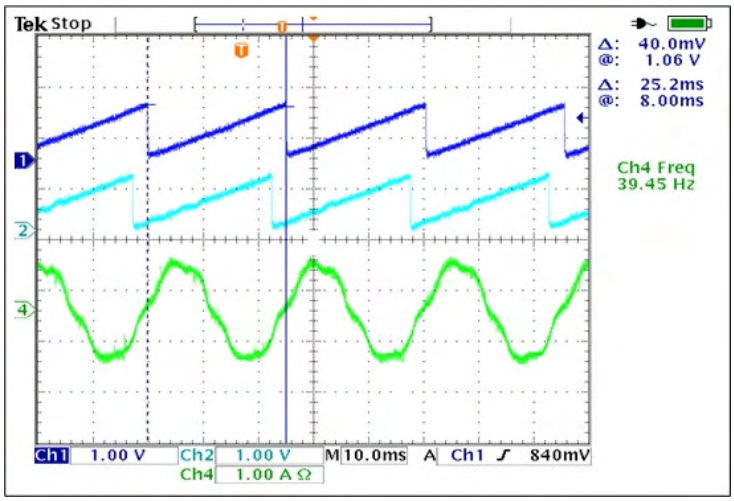

Figure 5-24 Ch1 Estimated rotor flux angle, ch2 actual rotor flux angle, ch4 line current at 40Hz supply frequency

During the experimental tests stationary frame currents $I^s_{d\ and}$ I^s_q are considered as well. These currents are observed from the DSP evaluation board's digital to analog channels, since the calculations are carried out by DSP in pu. Base current is taken as 7.5 A for the calculations. DAC of the evaluation board can give an output between 0-3.3 V range, and since the currents swing in positive and negative directions equally this range is to cover this swing in both directions therefore an offset of 1.65 V is added in order to bring zero level of the currents to the midpoint of the output range. After the currents are sampled with analog to digital converter of DSP EVM (Evaluation Module) 1.65V is subtracted from and halved in order to prevent overflow, then they are used in calculations. Therefore, in order to compare the line current with the stationary reference frame currents these should be considered. In Figure 5-25 the amplitude of the line current is 14A. First it is transformed into pu as 1.87 A (I_{base}=7.5A). Half of it (0.94 A) is the amplitude of the stationary frame currents. The reason for distortions seen in the peak of the currents seems to be poor hardware design for current measurement. Specifically, the operational amplifiers used in the hardware enter into saturation for large currents. Because the current measurement circuit is designed for rated 12 A, these circuits should be redesigned according to the real requirements as a future work.

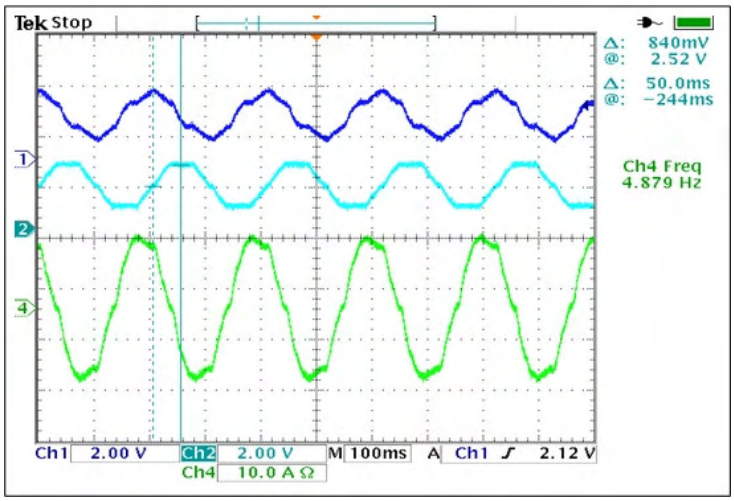

Figure 5-25 Stationary frame currents (I^s_d , channel 1and I^s_q , channel 2), line current at 5 Hz

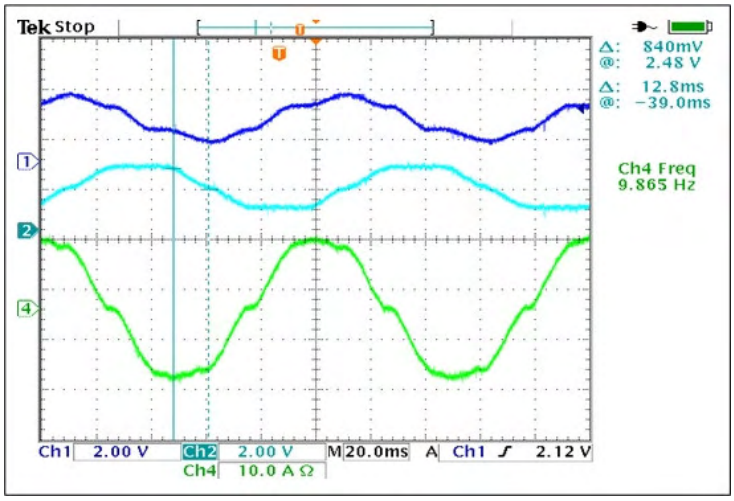

Figure 5-26 Stationary frame currents (I^s_d , channel 1and I^s_q , channel 2), line current at 10 Hz

Figure 5-26 shows the stationary reference frame currents at 10Hz supply frequency. As stated before the relation between the line current and the stationary reference frame currents can be easily determined but will not be repeated here again. The same electrical entities are recorded for two different operating frequencies of 30 and 40 Hz. These graphs are shown in Figure 5-27, Figure 5-28, respectively. Note that current magnitudes decrease as the supply frequency increases due to the induction

motor dynamics. At low frequencies back emf of the motor decreases and therefore the line current increases. Throughout all tests currents come out close to sinusoidal in shape. This is important for true estimation of rotor flux angle and the speed.

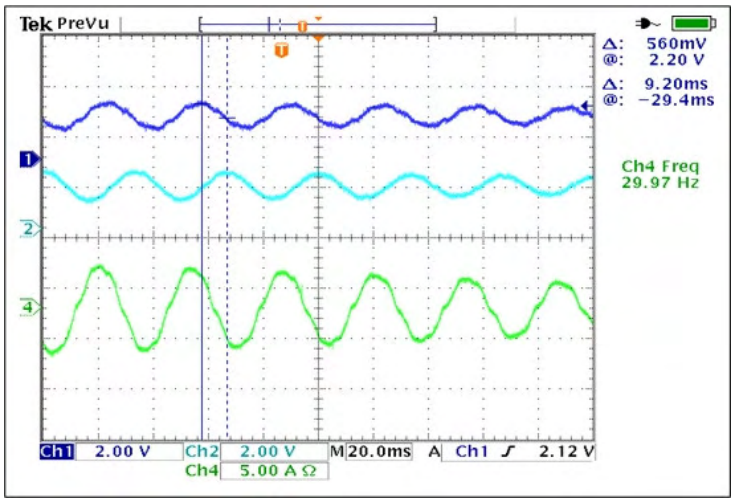

Figure 5-27 Stationary frame currents (I^s_d , channel 1and I^s_q , channel 2), line the current at 30Hz

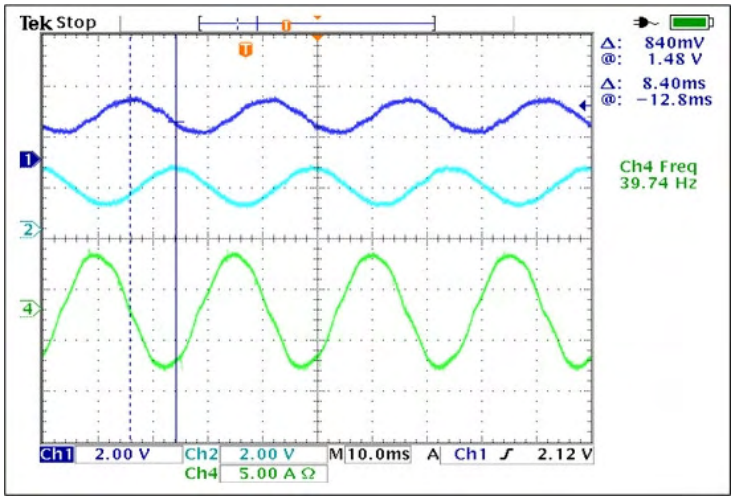

Figure 5-28 Stationary frame currents (I^s_d , channel 1and I^s_q , channel 2), line current at 40Hz

Table 5-2 shows the estimated speeds measured through the digital to analog converter channels of EVM at 5, 10, 15, 20, 25, 30, 35, 40, 45, and 50 Hz supply frequencies with an offset of 1.5 V. For each supply frequency expected speeds

(rad/sec) are calculated first. Then their pu representations are shown. If the offset is subtracted from the measured estimated speeds it is obviously seen that the expected values are similar to estimated ones. The linearity between the estimated speeds and the supply frequency can easily be seen in Figure 5-29. There are some points where the linearity is lost, but this may be due to measurement error made in noisy environment. Also there may be some errors when these data are interpolated.

Table 5-2 Estimated speeds (pu) for different supply frequencies

f(Hz)	Speed (rad/sec)	Speed (pu) Base speed=400rad/sec	Estimated Speed (pu) with an offset 1.5
50	157	0,39	1,88
45	141,3	0,35	1,84
40	125,6	0,31	1,81
35	109,9	0,27	1,77
30	94,2	0,24	1,74
25	78,5	0,20	1,71
20	62,8	0,16	1,67
15	47,1	0,12	1,64
10	31,4	0,08	1,61
5	15,7	0,04	1,55

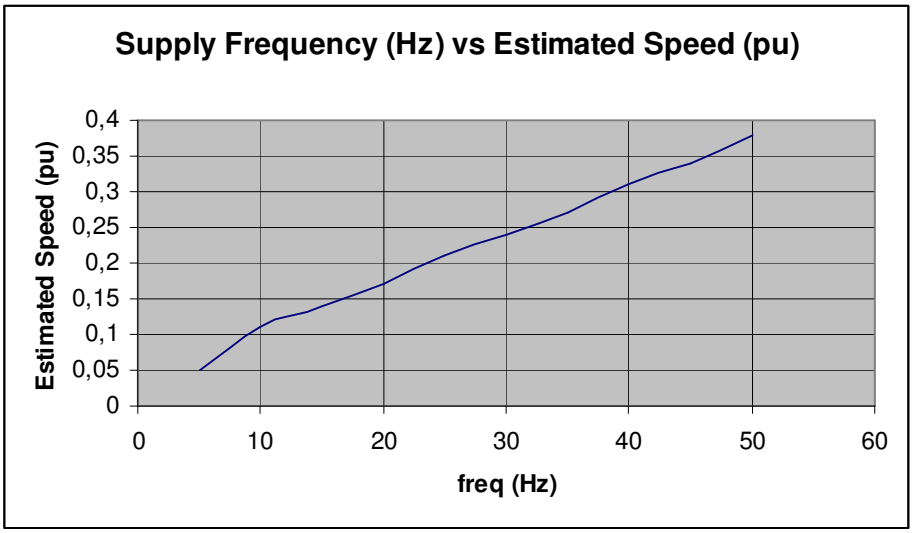

Figure 5-29 Estimated speed versus supply frequency

5.2.2 Experimental Results- For 0.1pu torque loading

The state estimator designed and implemented by using MRAS has been tested experimentally on the test setup when 0.1 pu load is applied. For this purpose a dc machine is coupled to the motor and used in generator mode. An electronic load, which draws a constant current of 10 A continuously, is connected to the armature terminals of the dc generator. For different speeds the voltages at the terminals of the dc machine are measured. From the voltages and currents and known value of the armature resistance the power dissipated on the dc machine is calculated by using well-known dc machine model. By considering the efficiency of dc machine, the mechanical power applied at the shaft of the dc machine, identically the mechanical power output from the induction machine, is determined. This power is divided by the measured speed in rad/sec then the torque developed by the induction motor is calculated. Theoretically dc machine electromechanical torque is dependent on the armature current when the field mmf is kept constant. For that reason in order to keep the torque applied to the motor shaft at different speeds, the load current is kept constant also.

The ac motor is operated in open-loop at different speeds, by applying 10, 20, 30, 40, 50 Hz supply frequencies with the applied torque. The actual and the estimated rotor flux angles and one of the line current of the motor are recorded. The

stationary reference frame currents i^s_d and i^s_q have pure sinusoidal waveforms but they are not shown here. The exact results of the estimated the rotor flux angle prove that these currents are pure sinusoidal.

The motor is first run at 10Hz. In Figure 5-30 estimated rotor flux angle is shown together with the actual one. Trace 1(actual) and trace 2 (estimated) represent the rotor flux angles with reference to the stator d^s-axis position. They change from 0 to 1 pu (2π) as seen in the figure. The time elapsed from zero value of the rotor angle to 1 show the full period for the synchronous frequency as 100 msec. The figure shows clearly the close similarity between the estimated rotor flux angle and the actual angle. The line current recorded in the test as trace 4 is close to sinusoidal in shape at 10Hz.

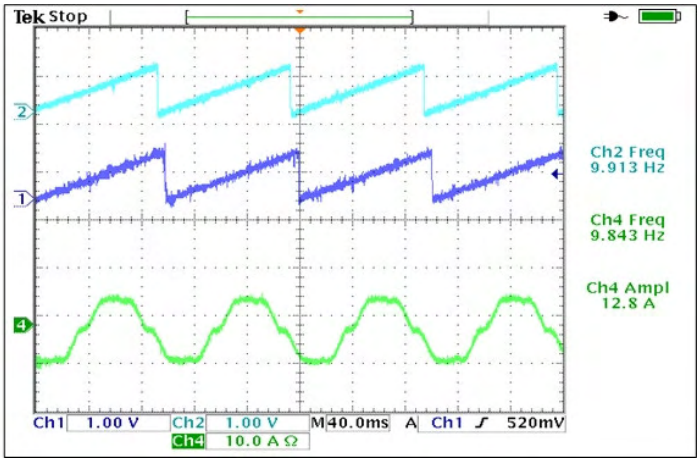

Figure 5-30 Ch1 actual rotor flux angle, ch2 estimated rotor flux angle, ch4 line current at 10Hz supply frequency for 0.1 pu loading

The motor is next run at 20Hz. The results are shown in Figure 5-31. Note that trace 1(estimated rotor flux angle) is almost the same as trace 2 (actual rotor flux angle) indicating that the rotor flux angle is estimated correctly. The frequencies in both graphs are 20 Hz as seen. The line current shown in Figure 5-31 as trace 4 is close to sinusoidal in shape.

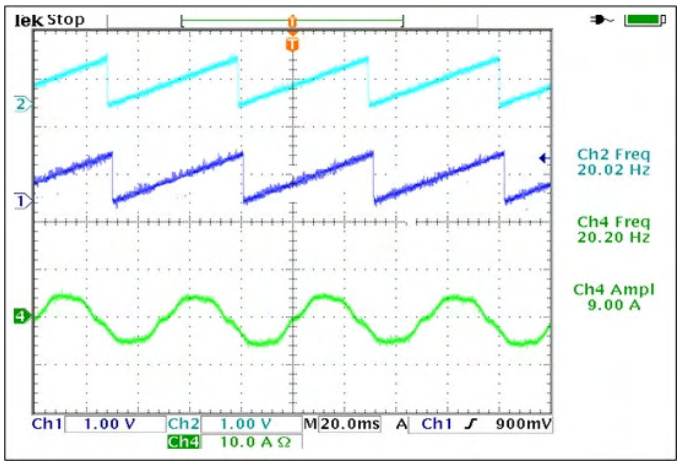

Figure 5-31 Ch1 actual rotor flux angle, ch2 estimated rotor flux angle, ch4 line current at 20Hz supply frequency for 0.1 pu loading

After that the supply frequency is increased to 30Hz. This time the rotor flux angle is estimated with a delay of 2 msec because of the same reason defined for the no-load operation at 30 Hz before. As seen in Figure 5-32 the line current of the motor as trace 4 is again close to sinusoidal.

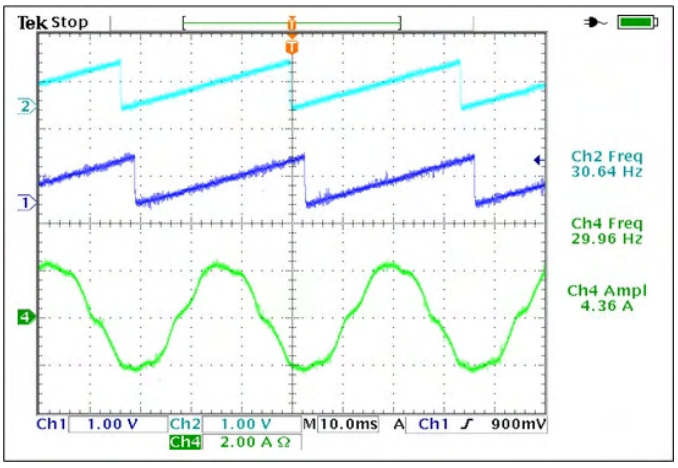

Figure 5-32 Ch1 actual rotor flux angle, ch2 estimated rotor flux angle, ch4 line current at 30Hz supply frequency for 0.1 pu loading

Figure 5-33 shows the estimated and actual rotor flux angles with the line current waveform at the same frequency with the supply.

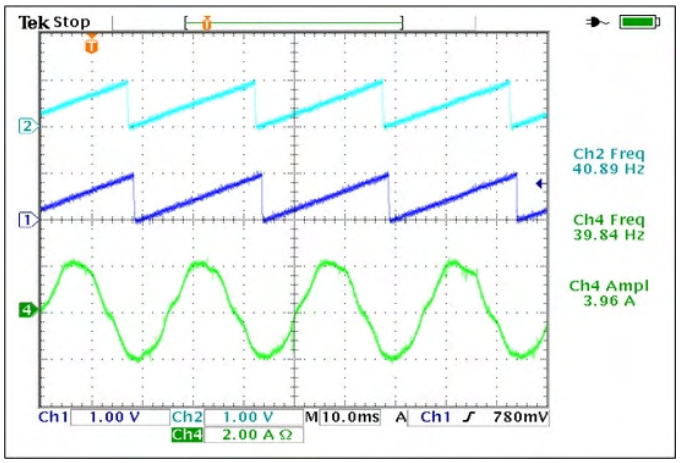

Figure 5-33 Ch1 actual rotor flux angle, ch2 estimated rotor flux angle, ch4 line current at 40Hz supply frequency for 0.1 pu loading

5.3 Conclusion of the Simulations and Experiments

From the simulations and the experimental results it is obvious that there are not considerable differences between the actual and the estimated values of the speed. Estimated waveforms, obtained at both the high speed and low speed, confirm that flux and speed estimation performance from MRAS scheme is quite satisfactory and not causing instability. Heavy loading, however, may lead to increase of transient speed errors to some extent resulting from high instantaneous speed changes. Also as expected, the line currents increase according to the applied load. Under all circumstances, the performance of MRAS in the transient speed tracking at start, and the steady-state speed estimation is quite high. The performance of the speed observer under no-load condition is quite impressive even at very low speeds. Since the speed cannot change very fast due to mechanical loading, very smooth speed outputs are obtained with negligible speed errors.

Simulation and experimental studies show that there usually exists a small steady-state error between the estimated and actual speed values but this seems to be at negligible levels.

The steady state accuracy of MRAS meets the expectations and the performance of MRAS may be considered as quite successful. Both speed and flux estimators work properly.

6 THE HARDWARE & SOFTWARE

In this chapter, the hardware configuration of experimental setup and the software organization is summarized. The hardware configuration of the project is basically the combination of an asynchronous motor, a motor drive and a microprocessor. The software of the project involves assembly code of the FOC and state observers in modular strategy.

6.1 The Motor

The experimental setup of this thesis is as shown in Figure 6-1. While testing the setup, different motor sizes are used, but in the actual experimental stage 3kW squirrel cage induction motor (Siemens make) is used. In order to obtain motor parameters, classical no-load and locked-rotor tests are carried out on the motor. For the initial guess to the parameters used in the FOC algorithm is obtained from the steady-state equivalent model of the induction motor shown in Figure 6-1. In the real time applications, motor drives are expected to derive motor parameters during the initialization of the system by means of properly injected signals and then estimate on-line by the FOC algorithm embedded in the system during normal running. These methods are skipped in this work and considered as future work. In this thesis, different from on-line parameter estimation, closed-loop observer (e.g. MRAS) is expected to compensate the effects of parameter deviations regarding the parameter errors as system noise. Referring to the equivalent circuit of the machine in Figure 6-2.

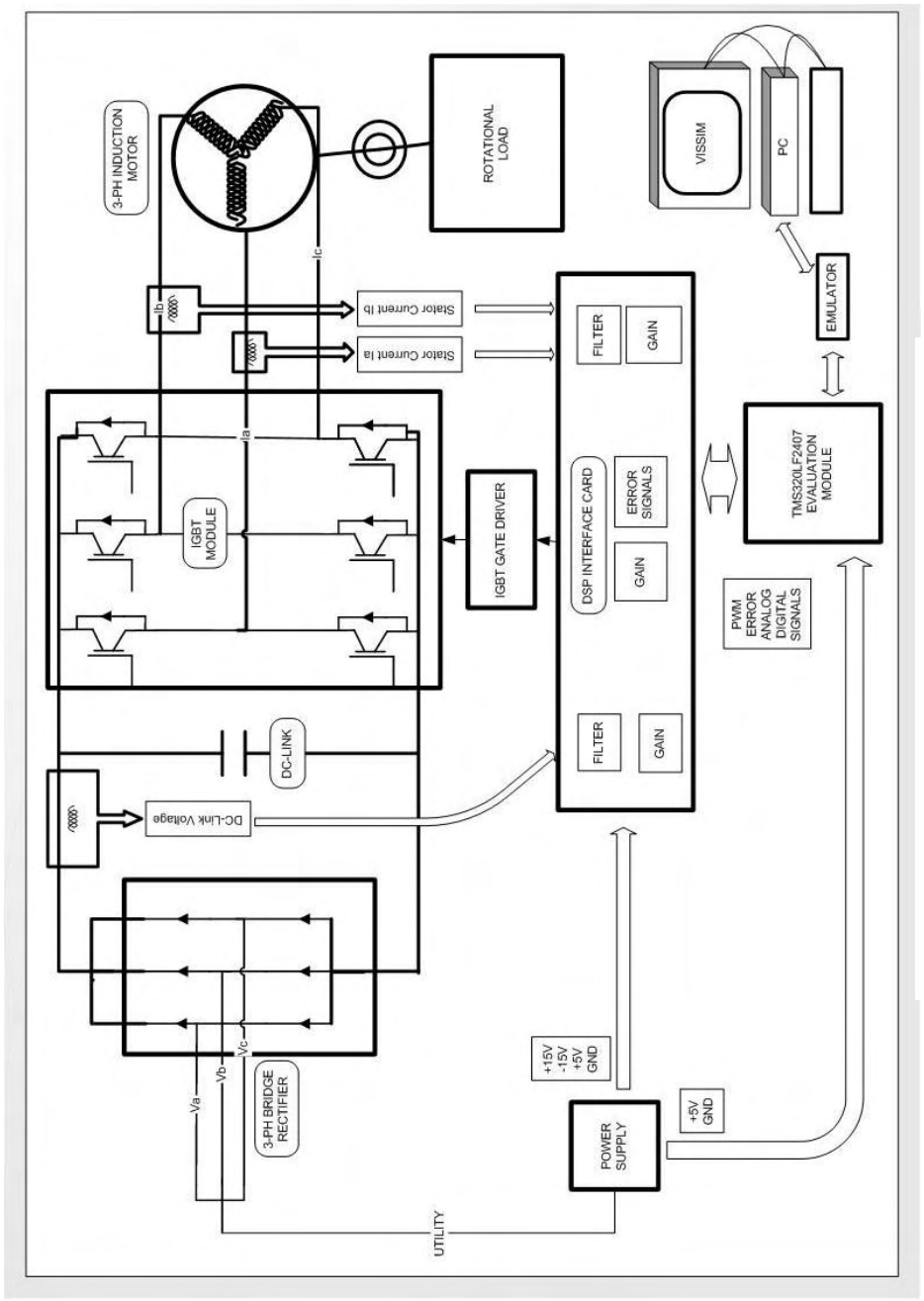

Figure 6-1 Overall hardware configuration of the setup

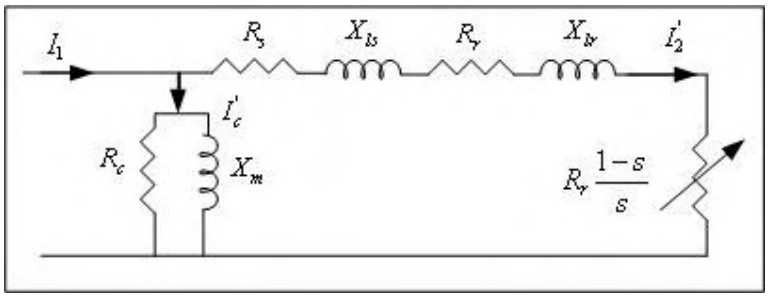

Figure 6-2 Approximate per phase equivalent circuit for an induction machine

R_s is obtained by dc-test, R_c and X_m are determined by no-load and the rest of the parameters are determined by locked-rotor test. The stator resistance of each stator winding can be measured independently by applying a dc-current to one phase as shown in Figure 6-3.

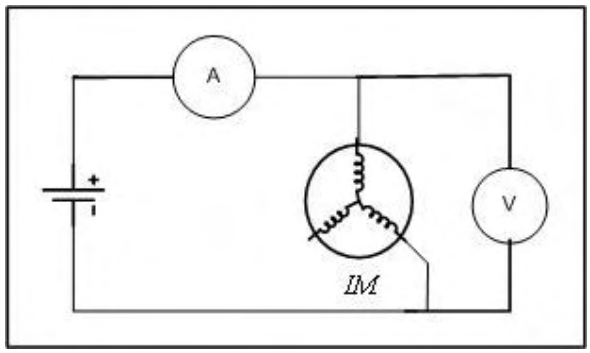

Figure 6-3 Diagram of dc measurement

The stator resistance is measured on the motor terminals by applying a current through a resistor and measuring the corresponding voltage, or without a resistor applying low-level dc voltage. To obtain a more accurate measurement result, one must get several numbers of measured data and take the average of these data for each phase.

The leakage-reactances x_{ls}, x_{lr} and the rotor resistance are determined when the motor speed is set to zero, i.e. s=1. Since the magnetizing branch elements are large enough compared to the rest of the equivalent components, these are neglected in this test. It is further assumed that leakage reactances are equal to each other according to IEEE test standards. Since stator resistance is measured and leakage

reactances are assumed to be equal, rotor resistance can easily be calculated from the measured data. The measurements are done around the rated current of the motor and than the average of the measurements are computed to obtain more approximate parameters.

When the motor is running without load, the slip will be close to zero. Thus, the variable slip resistance will be very large. Therefore, in the no-load test one may consider the magnetizing branch as the approximate circuit of the motor model. The no-load data are measured around the rated voltage, and magnetizing branch elements are calculated around the rated voltage of the motor. The calculated motor parameters and ratings of the motor are given in Table 6-1.

Table 6-1 Motor Parameters per phase

Rs (stator resistance)	1.8Ω
Rr (referred rotor resistance)	2.18Ω
Rc	522 ohm
Xm (magnetizing reactance)	63.7Ω
Xls,Xlr (leakage reactances)	2,69Ω
Ls,Lr (stator & rotor induc.)	0,192H
Lls,Llr (leakage induc.)	0,00084H
Lm (magnetizing induc.)	0,184H

6.2 The Motor Drive

The drive circuit used here has been developed in another work but modified to suit to the requirements of this work [25]. The drive mainly includes a rectifier, dc-link circuit and an inverter. The rectifier used in this drive is Semikron-SKD28 that consists of six uncontrolled diodes. The rated output current of the rectifier is 28 A and the rated operating voltage is 1300 V. During the tests, the three-phase voltage is supplied over an autotransformer to the rectifier.

In the dc-link circuit, the rectified voltage is a smooth dc filtered by two dc-link capacitors each being 1000μF and connected in series. In addition to them a resistor of 30KΩ, 1W, is connected across each capacitor to equalize their voltage sharing. The dc link voltage is impressed on the capacitors through a relay system as shown in the Figure 6-4.

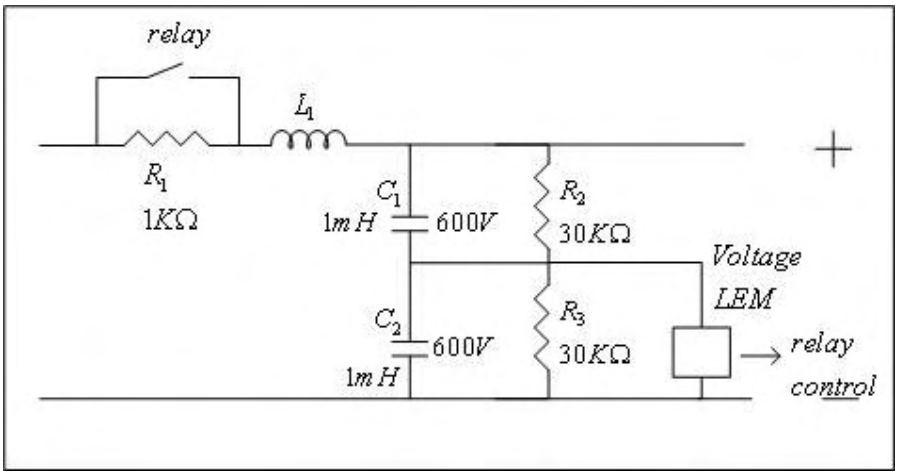

Figure 6-4 Dc-link circuit

At the beginning, the capacitors are charged to a certain level through a 15 W resistor to limit the inrush current at starting. When the capacitors are charged to predefined level, the relay disconnects the resistor. One can change the relay on-off voltage level by adjusting the control potentiometer on the interface card. Furthermore, by adding a manual switch, on-off state of the relay can be controlled manually. As a future work at this point, a dynamic braking circuit (freewheeling path controlled by a switch) may be added to avoid over-charging of the capacitors while the motor is slowing down rapidly.

The inverter on the drive is Semikron_Semitrans IGBT module (SKM 40 GD 123 D). The rated value of V_{ce} in this IGBT package is 1200V and I_c is 40/30 A depending on the case temperature. The switching rise time of the IGBT switches is 55 ns and the switching fall time of the switches is 40 ns. This package may be used for applications at switching frequencies above 15 kHz. IGBTs in this module are triggered by a gate drive card, Semikron six IGBT driver (SKHI 60 H4). The gate drive card provides short-circuit protection for all six IGBTs in the full bridge. Short circuit protection scheme is based on the real-time tracking of the collector-emitter voltage of the devices. In case a fault is detected, it switches off all IGBTs at once and gives an alarm. In our setup, these error outputs of the gate-drive card are used for fast hardware interrupt so that the interlock circuit blocks simultaneous turning on of IGBTs of the same arm. One further constraint in the operation of the bridge is

that no IGBT is turned on unless the gate charge of the other IGBT is completely removed.

The output of the inverter is connected to the motor through current sensors to acquire information about currents in real-time. Overall diagram of the inverter is shown in Figure 6-5.

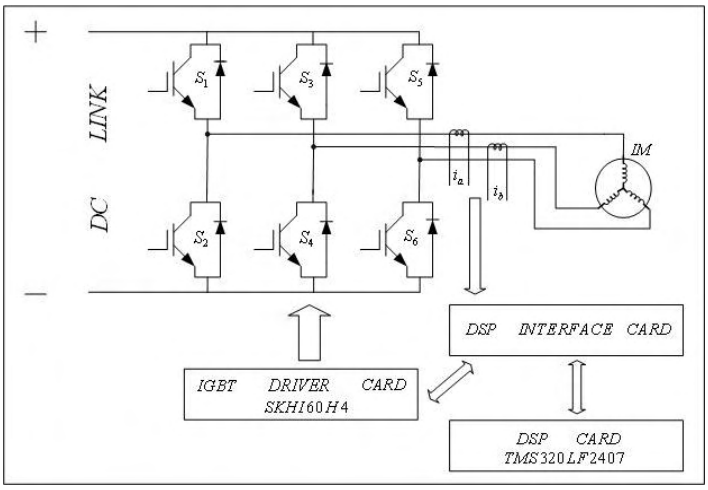

Figure 6-5 Inverter circuit

6.3 The DSP

In order to run the real-time control algorithm and create PWM signals, Texas Instruments' (TI) TMS320 processor is used in this work. Texas Instruments' TMS320 family consists of fixed-point, floating-point, multiprocessor digital signal processors (DSPs). TMS320 DSPs have an architecture designed specifically for real-time signal processing. The LF2407 is a member of the "C2000 DSP" platform, and is optimized specifically for control applications. The "C24x series" of DSP controllers combine this real-time processing capability with controller peripherals to create a suitable solution for vast majority of control system applications. The following characteristics make the TMS320 family a suitable choice for a wide range of processing applications:

- Flexible instruction set,
- Inherent operational flexibility,

- High-speed performance,
- Innovative parallel architecture,
- Cost effectiveness.

TMS320F2407 version of this family is the one used in this application. It uses a 16-bit word length along with 32-bit registers for storing intermediate results, and has two hardware shifters available to scale numbers independent of the CPU.

The C24x DSP controllers take advantage of an existing set of peripheral functions which includes:

- Timers,
- Serial communications ports (SCI, SPI),
- Analog-to-digital converters (ADC),
- Event manager,
- System protection, such as low-voltage detection and watchdog timers.

To function as a system manager, a DSP must have robust on-chip I/O and other peripherals. The event manager of the LF2407 is application-optimized peripheral unit, coupled with the high-performance DSP core, enables the use of advanced control techniques for high-precision and high-efficiency full variable-speed control of motors. Included in the event manager are special pulse-width modulation (PWM) generation functions, such as a programmable dead-band function and a space-vector PWM state machine for 3-phase motors that provides quite a high efficiency in the switching of power transistors. Three independent up/down timers, each with it's own compare register, support the generation of asymmetric (non-centered) as well as symmetric (centered) PWM waveforms.

6.4 Interface Card

In order to convey information back and forth between the power stage and DSP an interface card has been designed. Moreover, suitable signal amplification, signal filtering and hardware protection properties are added to this interface card (see Appendix A).

The dc-link voltage is sensed with a voltage sensor (LV25_P) on the interface card. The insulation property of the voltage sensor is quite sufficient to protect the

digital circuit and low voltage analog circuit from high voltage part. The magnitude of the dc-link voltage is sensed to re-build the phase voltages (V^s_d & V^s_q) in the control software with the information of duty-cycles of the IGBTs (Appendix B). Another aim of the voltage sensor is to sense the overcharge on the dc-link capacitors. If the voltage level exceeds the predefined limit that is determined by the user, a comparator gives an error signal. This error signal is used for immediate hardware interrupt and all the IGBTs are set to off-state. Finally, to take the power resistance used in the dc link line to limit the in-rush current at starting out, the dc link voltage level information is needed to operate the relay across this resistance. The voltage sensor also provides this voltage information whether it exceeds the adjusted voltage level or not. If this mechanism is employed then the relay will operate automatically after the start command in a very short time.

In addition, the PWM signals generated by DSP are amplified to make them compatible with the gate drive card inputs. For this purpose, six PWM signals are adjusted to 15V individually without any other change. Finally, all the errors, gate drive card errors, over-voltage error, over-current error, and an external error are *OR* gated. The single error output from this gate is assigned to control PWM-OFF circuit to set the all IGBTs to off-state in case of any fault. Figure 6-6 shows the DSP interface card.

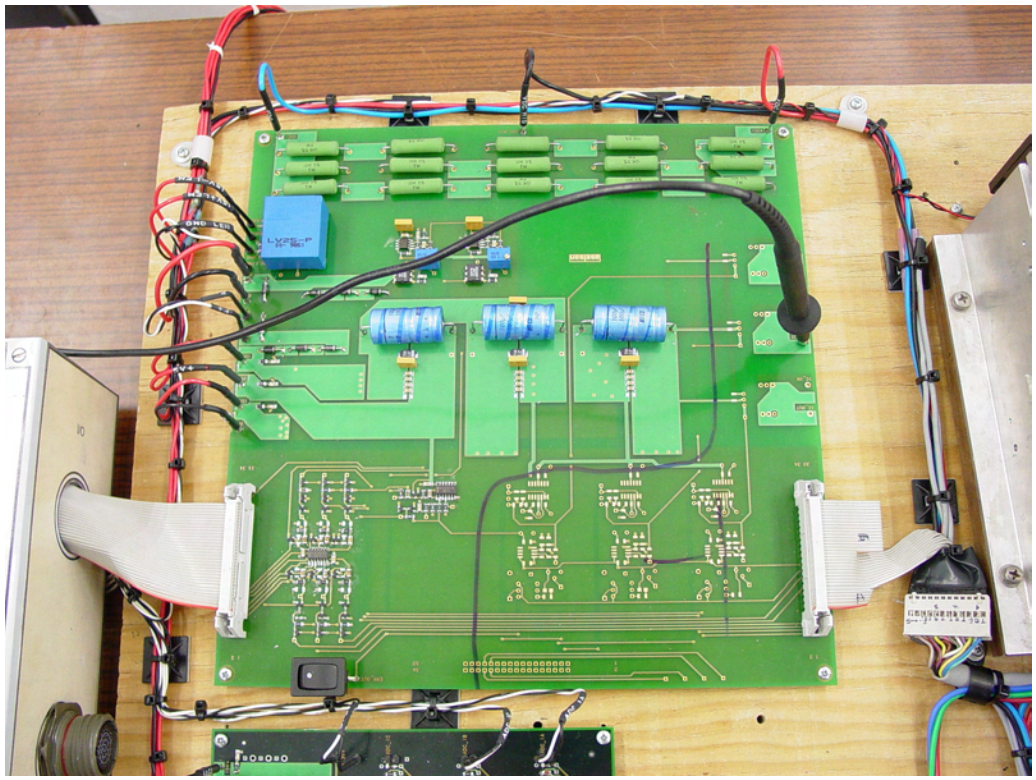

Figure 6-6 Dsp interface card

6.5 Current Interface Card

The other sensed variables are stator currents using current-sensor on the interface card. For this purpose LA 25-NP current transducers are used. These sensors are capable of sensing AC, DC and mixed current waveforms. The sensor has multi-range current sensing options depending on the pin connections. The sensors use hall-effect phenomena to sense the current. They have excellent accuracy and very good linearity in the operating range. The output of these sensors is between ±15V and unipolar. Since the ADCs on the DSP board cannot sense the negative voltage and requires signal between 0-3.3V, our current sensors are used with current interface card. Normally, one must add offset to the AC current signals to compensate the negative parts and then subtract this amount in the software. Furthermore, the current signals must be normalized between the 0-3.3V range using amplifiers before the ADCs. All of these procedures cause extra uncertainty that affects the accuracy of the sensed information.

In case of noisy phase currents, optional low-pass filters are placed on the interface card with 1kHz cut-off frequency. However, at high frequency range above 50Hz these filters may cause serious phase lagging problem. The outputs of the current transducers are also used to provide over-current protection. After determining the over-current limit, the potentiometers in the protection circuit are set to this critical limit. In case of over-current problems a comparator gives error signal to set the IGBTs into off-state.

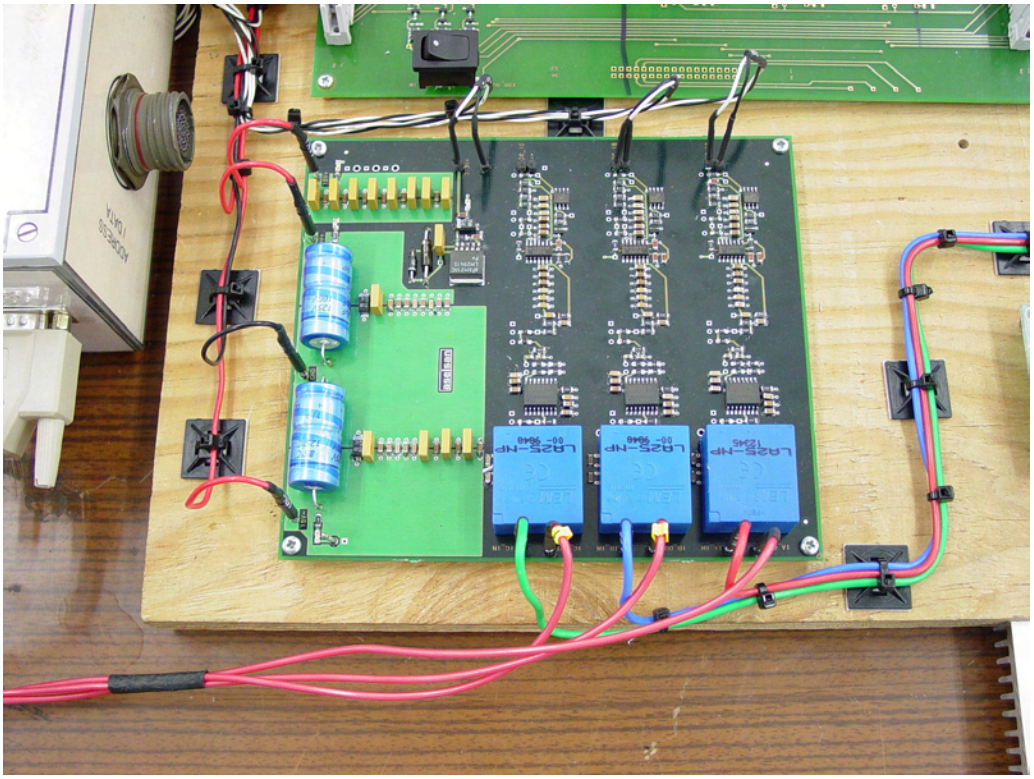

Figure 6-7 Current interface card

6.6 Software Overview

In this part the reason of using pu method and how to calculate the pu unit values are stated. Also the algorithm for specific fixed-point numerical methods will be analyzed.

6.6.1 Base Values and PU model

Since the TMS320LF2407 is a fixed point DSP, PU (per unit) model of the motor is used to increase the accuracy and simplify the overall system. In a fixed point system, 16 bit words are assigned to variables and some of the bits are used for integer part of the number and some for floating part. To increase the accuracy, one must reserve as many bits as possible to floating part. This is also possible with pu system. If the pu parameters and variables are properly chosen, the integer part will expected to be at most ± 1 and the number of the bits reserved for the floating part will be maximized.

While choosing the pu values, one may select ratings of the motor or multiple of the nominal values as base depending on the operating conditions. One must be careful about the transient regions, since the amount of the states may exceed the unity in transient state. Thus, the multiple of the nominal values may be adjusted according to the transient state peak values to limit the base values. However, this will give harm to the accuracy of the steady-state computations. Due to this reason, while testing the performance of the observers, we run the system under light-load conditions. The base quantities are calculated as shown below:

$$\begin{aligned} I_b &= K_1 * I_n \\ V_b &= K_1 * V_n \\ w_b &= 2\pi f_n \\ \psi_b &= \frac{V_b}{w_b} \end{aligned} \qquad (6.1)$$

where I_b, V_b, are the maximum values of the phase nominal current and voltage; w_b is the electrical nominal rotor flux speed; ψ_b is the base flux and subscript n is expresses the nominal quantities of the same variable. The real time quantities are implemented in to the control thanks to the pu quantities, which are defined as follows:

$$i = \frac{I}{I_b}$$
$$v = \frac{V}{V_b} \qquad (6.2)$$
$$\psi = \frac{\psi}{\psi_b}$$

6.6.2 Fixed-Point Arithmetic

In binary format, a number can be represented in signed magnitude, where the left-most bit represents the sign and the remaining bits represent the magnitude. Two's complement is an alternative form of representation used in most processors, including the TMS320. The representation of a positive number is the same in two's complement and in signed magnitude. Thus the first bit gives idea whether the number represented in signed magnitude is positive or negative.

In fixed-point operations Q_k format is used to represent the floating numbers. For example, in Q_{12} format, first bit is assigned for sign and three bits are assigned to represent the integer part and the rest of the 16 bits is assigned for floating part of the number. In Q_{15}, one bit is assigned for sign and the rest is assigned for floating part. Thus one can represent the number in the range of -1 to 1 excluding these to integers. So if the variables are normalized in a proper way those never exceed unity, Q_{15} format provides the best accuracy. If one uses numbers greater than unity then, the Q_k format must be rearranged to represent those numbers. For example, using Q_{12} format the numbers between the –7.999 to +7.999 with a less accuracy in the floating part since the floating part may be represented with fewer numbers when compared to the Q_{15} format. The resolution of the Q_{15} format is 0.0000305 ($1/2^{15}$) where Q_{12} format is 0.000244 ($1/2^{12}$). If the selected base values are in nominal values, than drive control quantities will not be greater than four times the nominal values (for the most part). In this case one may use Q_{12} format. On the other hand, if the value of the variables are guaranteed to be less than unity by choosing proper base quantities, Q_{15} format is preferred . The generalized representation of Q_k is given below:

$$Z = -b_{15-k} * 2^{15-k} + b_{14-k} * 2^{14-k} + ...b_0 + b_{-1} * 2^{-1} + b_{-2} * 2^{-2} + ... + b_{-k} * 2^{-k} \quad (6.3)$$

where k represent the number of bits representing floating part and b is the binary (0,1) quantities. Here are some examples to clarify the concept:

pi=3.14159265= 0011.0010 0100 0011 in Q_{12} format (3243H)

= 011.0 0100 1000 0111 in Q_{13} format (6486H)

0.0045 = 0000. 0000 0001 0010 in Q_{12} format

= 0.000 0000 1001 0110 in Q_{15} format

The summation of the numbers in Q_k format is the same as binary system summation. However, the multiplication has some tricks. In the multiplication of the Q_k format, the result is in the form of: $Q_n * Q_m = Q_{n+m}$. Since the multiplication operation is done in the 32 bit accumulator, Q_{n+m} may exceed to Q_{30} without any problem.

For example, $Q_{12} * Q_{12} = Q_{24}$

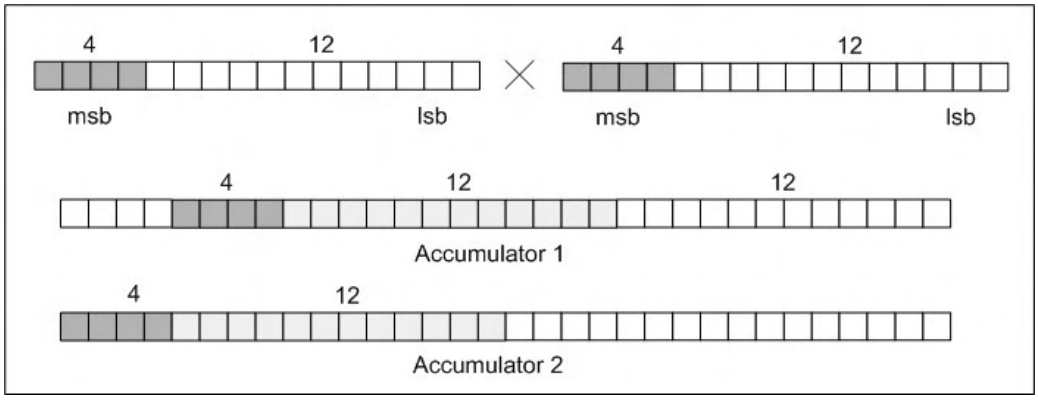

Figure 6-8 Multiplication in dsp accumulators

After the multiplication Q_{24} is stored to the accumulator as shown in accumulator_I (Figure 6-8). The right bits of the shaded part are neglected in accumulator_I. Before storing to a 16-bit microprocessor word, the number in the accumulator must be left shifted as in the case of accumulator_II and than the high word in the accumulator must be stored the associated word. In the multiplication of Q_k format n and m above may be any number between 0-15. However, 16-bit result must be aligned to either high or low word of the accumulator in the form of any Q_{15} format.

7 CONCLUSION and FUTURE WORK

7.1 Conclusion

The focus of this thesis has been the Direct Field Control of induction machine. Modified direct torque and flux control strategy based on two PI controllers and a voltage space-vector modulator module are used in order to observe rotor flux, stator flux, synchronous speed and rotor flux angle.

First, generalized dynamic mathematical model of the induction machine is studied in different reference frames. Induction machine mathematical model in stationary frame is investigated.

Next, Model reference adaptive system based closed-loop direct torque control of induction machines is simulated. A flux observer with voltage model-current model combination is implemented. The outputs of this observer were fed to an open-loop speed estimator. Also an experimental drive system was build and tested at high and low speeds using the same technique. It was shown that DTC-SVM strategy realizes almost ripple-free operation for the entire speed range. The flux, speed, and torque estimations are improved.

It can be stated that, using the DTC-SVM topology, the overall system performance is increased.

7.1 Future Work

This simulations and experimental works show the benefits of closed-loop full-order flux and speed observer models using MRAS technique. Due to experimental limitations the algorithm could not tested over a wide speed and torque ranges. In the future this work can be implemented.

Other MRAS algorithms based on reactive power regulation may be used for speed prediction.

Other sensorless techniques can be tested and the advantages and the disadvantages of the model can be clarified after the tests.

The machine parameters and the rotor time-constant can be estimated and used in the flux observer module and the closed-loop control can be improved.

REFERENCES

[1] B.K.Bose, “Power Electronics and AC Drives”, Prentice Hall, 1986

[2] P.Vas "Sensorless Vector and Direct Torque Control" New York: O. University Press, (1998)

[3] I.Boldea and S.A.Nasar, “Vector Control of AC Drives”, CRC Press, 1992.

[4] D.W.Novotny and T.A.Lipo, “Vector Control and Dynamics of AC Drives”, Oxford University Press Inc., Oxford, New York, 1997.

[5] R.D.Doncker and D.W.Novotny “The universal field oriented controller”, IEEE Tran. IA, vol. 30 no .1, pp. 92-100, January, 1994

[6] R.Lorenz “Tuning of the field oriented induction motor controller for high performance applications”, IEEE Tran. IA, vol. 22, pp. 293-297, 1986

[7] K.B.Nordinand D.W. Novotny “The influence of motor parameter deviations in feed forward field oriented drive systems” IEEE Tran. IA, vol. 21, pp.1009-1015, July 1985

[8] R.Krishman, F.C.Doran “Study of parameter sensitivity in high performance inverter-fed induction motor drive systems”, IEEE Tran. IA, vol. 23, pp.623-635, 1987

[9] P.L.Jansen and R.D.Lorenz “Transducer less position and velocity estimation in induction an salient ac machines”, IEEE Tran. IA, vol. 31, no.2, pp.240-247, Mar/April, 1995

[10] R.Gabriel, W.Leonhard and C.Nordby " Field oriented control of standard AC motor using microprocessor", IEEE Tran. IA, vol.16, no.2, pp.186.192, 1980

[11] H.Jun and W.Bin "New integration Algorithms for Estimating Motor Flux over a Wide Speed Range" IEEE Tran. IE, vol. 13, no.5, pp.969-977, 1998

[12] P.L.Jansen and R.D.Lorenz "Observer based direct field orientation: Analysis and comparison of alternative methods", IEEE Tran. IA, vol. 30, no.4, pp.945-953, Jul/Aug, 1994

[13] G.C.Vershese and S.R.Sanders "Observers for flux estimation in the induction machine" IEEE Tran. IE, vol. 35, no.1, pp.85-94, 1998

[14] Lennart Harneffors "Design and analysis of general rotor-flux oriented vector control system" IEEE Tran. IE, vol. 48, no.2, pp.383-390, 2001

[15] G.Yang and T.Chin "Adaptive-Speed identification scheme for a vector controlled speed sensorless inverter induction motor drive" ,IEEE Tran. IA, vol. 29, no.4, pp.820-825, 1993

[16] B.Robyns, B.Frederique, "A methodology to determine gains of induction motor flux observers based on a theoretical parameter sensitivity analysis", IEEE Tran. PE, vol. 15, no.6, pp.983-995, 2000

[17] A.M.Trzynadlowski, "The Field Oriented Principle in Control of induction Motors", Kluwer Academic Publisher, Norwell, MA, 1994

[18] M.Elbuluk, N.Langovsky and D.Kankam “Design and Implementation of a Closed Loop Observer and Adaptive Controller for Induction Motor Drives” IEEE Tran. IA vol. 34 no. 3 pp. 435-443, May/June 1998

[19] H.Tajima, Y.Hori “Speed Sensorless Field Orientation Control of the Induction Machine” IEEE Tran. IA vol. 29, no. 1, pp. 175-180, Feb.1993

[20] C.Schauder “Adaptive Speed Identification for Vector Control of Induction Motor without Rotational Transducers” IEEE Tran. IA vol. 28, no. 5, pp. 1054-1061, Oct.1992

[21] F.Z.Peng, T.Fukao “Robust Speed Identification for Speed Sensorless Vector Control of Induction Motors” IEEE Tran. IA vol. 30, no. 5, pp.1234-1239, Oct.1994

[22] L.Zhen and L. Xu “Sensorless Field Orientation Control of Induction Machines Based on Mutual MRAS Scheme” IEEE Tran. IE vol. 45 no. 5, pp. 824-831, October 1998

[23] C.Lascu, I.Boldea, F.Blaabjerg “A Modified Direct Torque Control for Induction Motor Sensorless Drive” IEEE Tran. IA vol. 36, no. 1, pp. 122-130, Jan 2000

[24] B. Akın, “State Estimation Techniques for Speed Sensorless Field Oriented Control of Induction Machines” M.S Thesis EE Dept. Metu Aug. 2003

[25] B. Mutluer, “Vector Control of Asynchronous Motors” M.S Thesis EE Dept. Metu Dec. 1999

[26] Texas Instruments, “Digital Motor Control Software Library”, Literature number: SPRU 485A Oct. 2003

[27] Texas Instruments, “ACI3-4 3-Phase Induction Motor Control”, App. Note, 15 Nov. 2000

A APPENDIX

ELECTRONIC CARDS

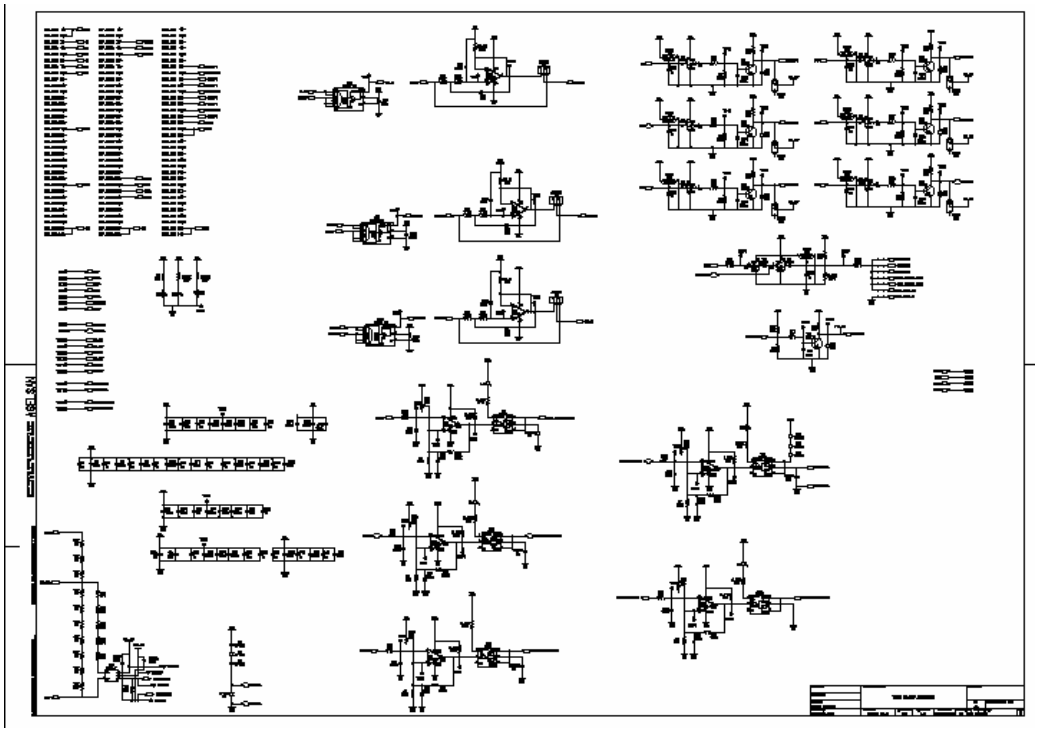

Figure A-1 DSP interface card

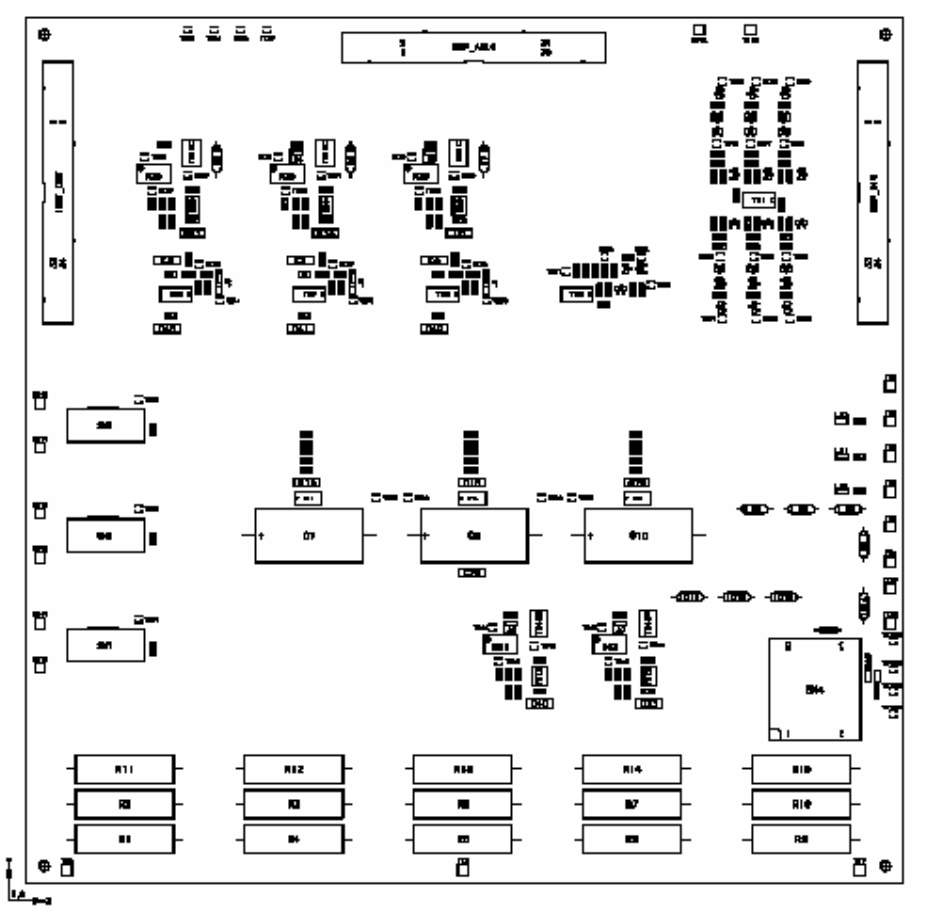

Figure A-2 Layout of DSP interface card

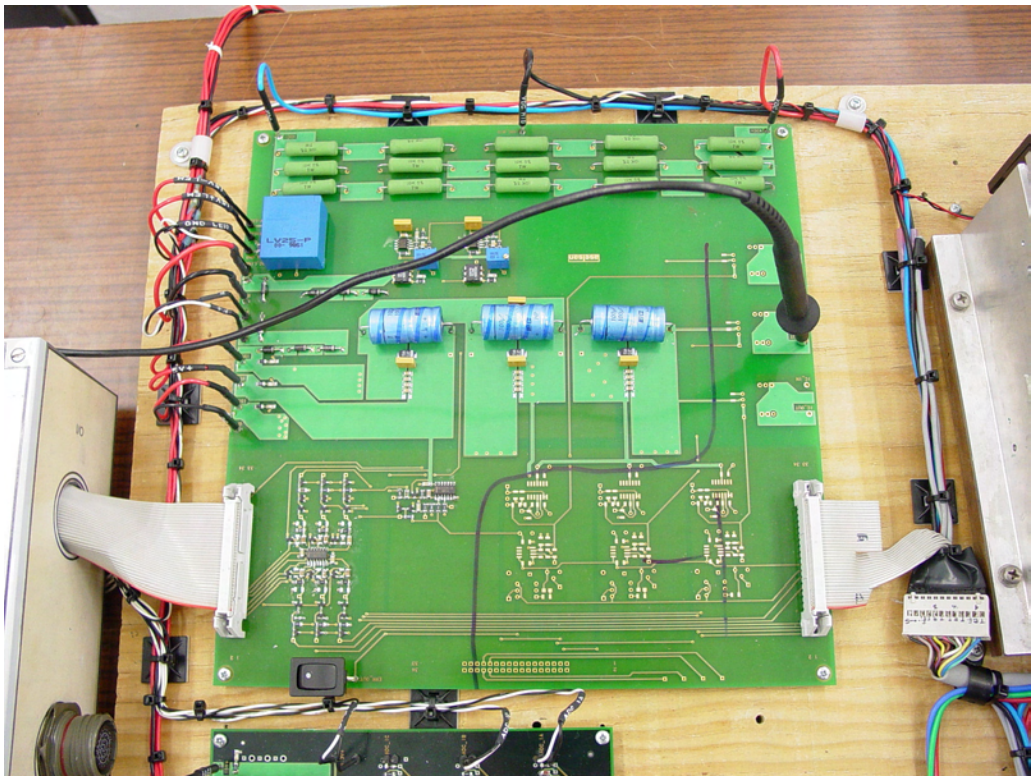

Figure A-3 View of DSP Interface Card

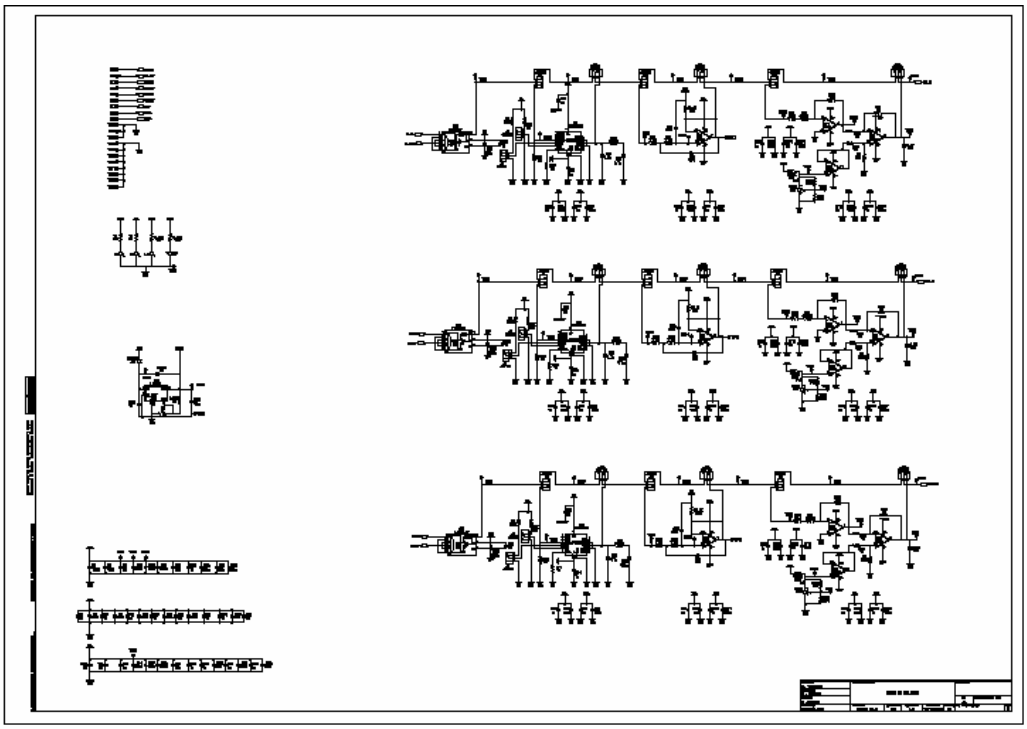

Figure A-4 Current interface card

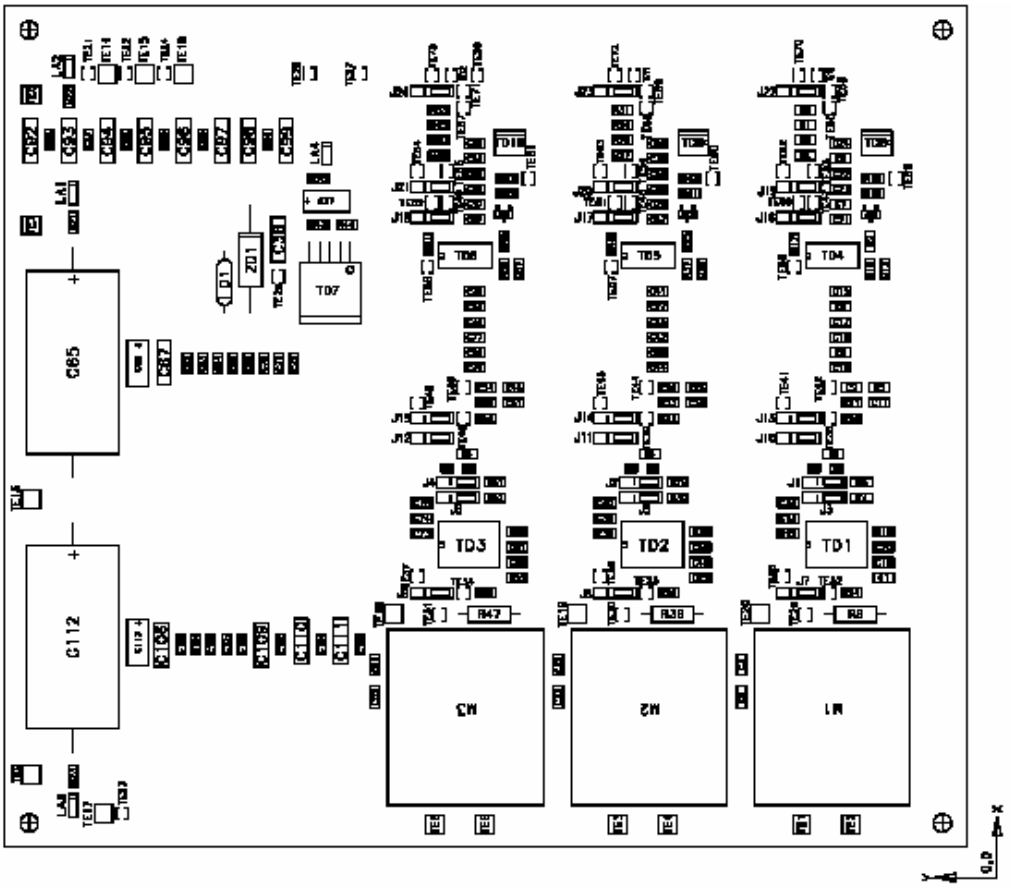

Figure A-5 Layout of current interface card

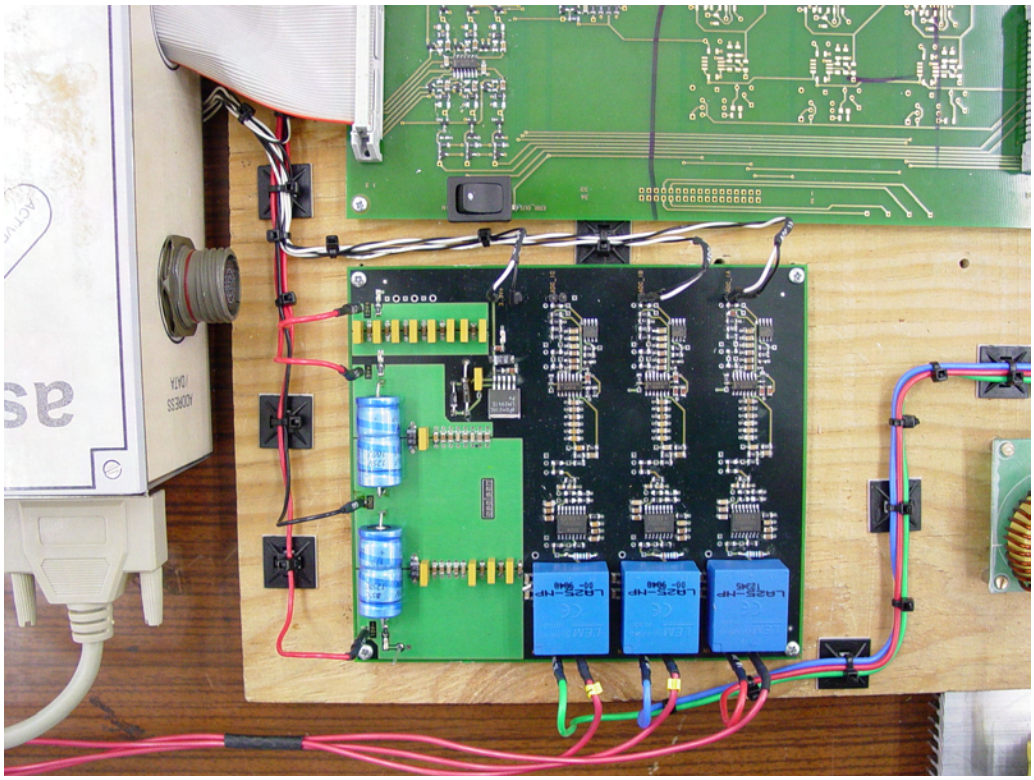

Figure A-6 View of current interface card

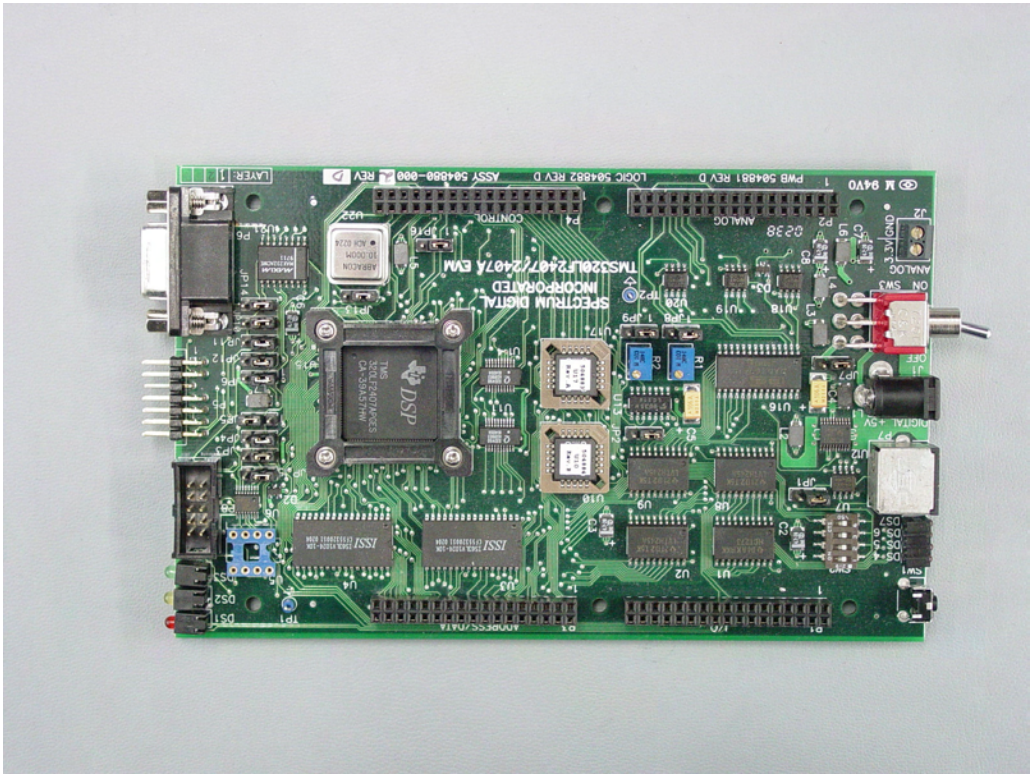

Figure A-7 View of DSP card

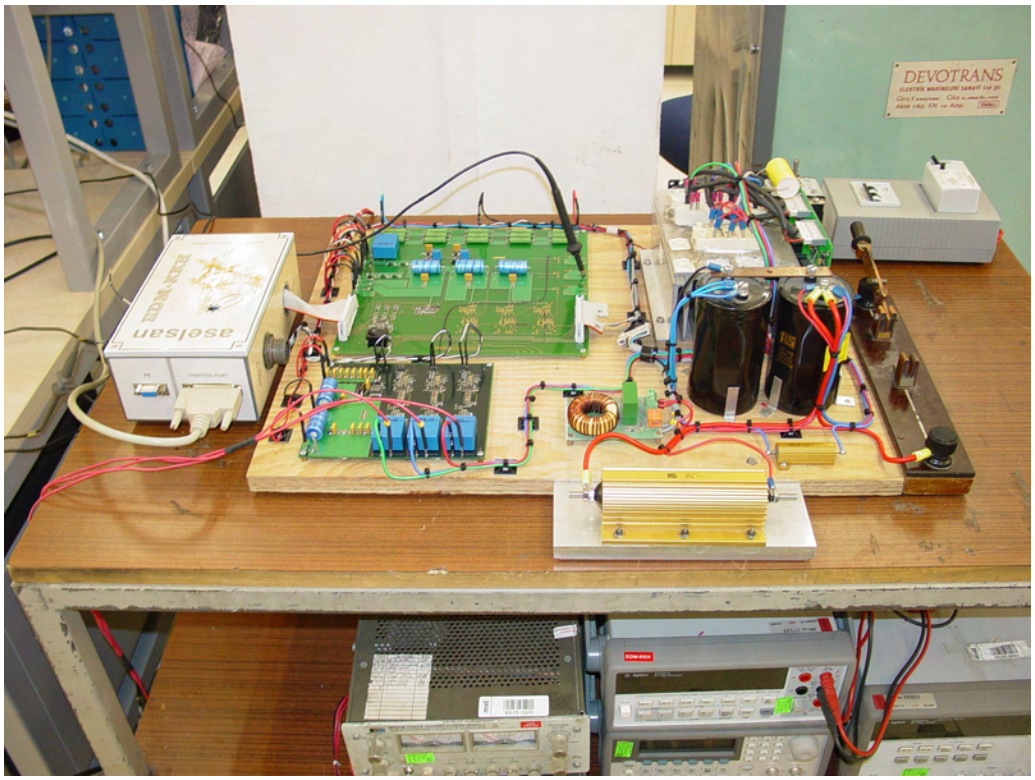

Figure A-8 View of the overall setup

B APPENDIX

ACQUISITION of the STATOR VOLTAGES

The induced voltage, which is the signal to be integrated for flux vector estimation, is obtained as the difference between the stator voltage and the resistive voltage drop across the machine windings. When a voltage source inverter (VSI) is used to feed the machine, the stator voltages are formed by pulse trains having a typical rise time 2-10kV/μs. These are digitally acquired at a high, though limiting sampling rate. The limited bandwith of such sampling process may fail to establish the exact volt-second equivalent between the actual and the acquired signals, and hence produce an error. To avoid this complication, some people use current source inverter or a linear power amplifier.

To avoid this problem in a switched VSI drive, it is preferred to replace the actual stator voltages by the reference voltage vector that controls the pulsewidth modulator.

The phase voltage of a general 3-phaase motor (V_{an}, V_{bn}, V_{cn}) can be calculated from the DC-bus voltage (V_{dc}), and three upper switching functions of inverter (S_1, S_2, and S_3). The 3-ph windings of motor are connected either Δ or Y without a neutral return path (or 3-ph, 3-wire system). The overall system is shown in Figure 2.

Each phase of the motor is simply modeled as a series impedance of resistance and inductance (r, L) and back emf (e_a, e_b, e_c). Thus, three phase voltages can be computed as

$$V_{an} = V_a - V_n = i_a r + L\frac{di_a}{dt} + e_a \quad \text{(B-1)}$$

$$V_{bn} = V_b - V_n = i_b r + L\frac{di_b}{dt} + e_b \quad \text{(B-2)}$$

$$V_{cn} = V_c - V_n = i_c r + L\frac{di_c}{dt} + e_c \quad \text{(B-3)}$$

Summing these three phase voltages, yields

$$V_a + V_b + V_c - 3V_n = (i_a + i_b + i_c)r + L\frac{d(i_a + i_b + i_c)}{dt} + e_a + e_b + e_c \quad \text{(B-4)}$$

For a 3-phase system with no neutral path and balanced back emfs, $i_a+i_b+i_c=0$, and $e_a+e_b+e_c,=0$. Therefore, equation,

$$V_a + V_b + V_c - 3V_n = (i_a + i_b + i_c)r + L\frac{d(i_a + i_b + i_c)}{dt} + e_a + e_b + e_c \quad \text{(B-4} \quad \text{(B-5)}$$

becomes, $V_{an}+V_{bn}+V_{cn},=0$. Furthermore, the neutral voltage can be simply derived from (B-5) as

$$V_n = \frac{1}{3}(V_a + V_b + V_c) \quad \text{(B-6)}$$

Now three phase voltages can be calculated as

$$V_{an} = V_a - \frac{1}{3}(V_a + V_b + V_c) = \frac{2}{3}V_a - \frac{1}{3}V_b - \frac{1}{3}V_c \quad \text{(B-7)}$$

$$V_{bn} = V_b - \frac{1}{3}(V_a + V_b + V_c) = \frac{2}{3}V_b - \frac{1}{3}V_a - \frac{1}{3}V_c \quad \text{(B-8)}$$

$$V_{cn} = V_c - \frac{1}{3}(V_a + V_b + V_c) = \frac{2}{3}V_c - \frac{1}{3}V_a - \frac{1}{3}V_b \quad \text{(B-9)}$$

Three voltages V_a, V_b, V_c are related to the DC-bus voltage (V_{dc}) and three upper switching functions (S_1, S_2, S_3) as:

$$V_a = S_1 V_{dc} \tag{B-10}$$

$$V_b = S_2 V_{dc} \tag{B-11}$$

$$V_c = S_3 V_{dc} \tag{B-12}$$

where S1, S2, and S3 =either 0 or 1, and S4=1-S1, S5=1-S2, and S6=1-S3.
As a result, three phase voltages in (B-7)-(B-9) can also be expressed in terms of DC-bus voltage and three upper switching functions as:

$$V_{an} = V_{dc}(\frac{2}{3}S_1 - \frac{1}{3}S_2 - \frac{1}{3}S_3) \tag{B-13}$$

$$V_{bn} = V_{dc}(\frac{2}{3}S_2 - \frac{1}{3}S_1 - \frac{1}{3}S_3) \tag{B-14}$$

$$V_{cn} = V_{dc}(\frac{2}{3}S_3 - \frac{1}{3}S_1 - \frac{1}{3}S_2) \tag{B-55}$$

It is emphasized that the S1, S2, S3 are defined as the upper switching functions. If the lower switching functions are available instead, then the out-of-phase correction of switching function is required in order to get the upper switching functions as easily computed from equation (S4=1-S1, S5=1-S2, and S6=1-S3).Next the clarke transformation is used to convert the three phase voltages (V_{an}, V_{bn}, and V_{cn}) to the stationary dq-axis phase voltages (V^{s}_{ds}, V^{s}_{qs}). Because of the balanced system ($V_{an} + V_{bn} + V_{cn}=0$) V_{cn} is not used in Clarke transformation.

C APPENDIX

HYPERSTABILITY THEORY

As with Lyapunov's method, an adaptive law designed using hyperstability theory is guaranteed to be stable. In the hyperstability approach the designer has to propose an adaptive law, and with the aid of hyperstability theory one can check whether this law gives a stable result. In general, a model reference adaptive speed estimator system can be represented by an equivalent non-linear feedback system which comprises a feed-forward time invariant linear subsystem and a feedback non-linear time varying subsystem. The first part normally contains the reference model, and its output is the error signal to be used in the adaptation. The second part contains the adaptive laws and has an output W. This division is illustrated in Figure C-1.

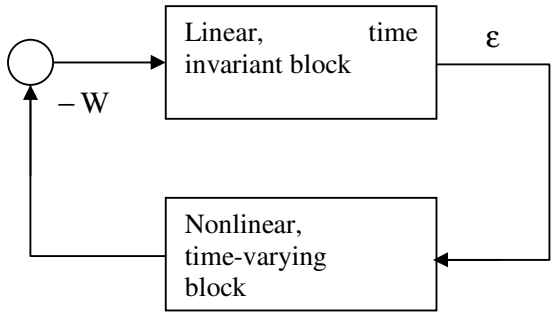

Figure C-1 Division of error equation into time invariant linear part and a time varying nonlinear part

Usually, the input -W of the linear block equals the multiplication of the parameter error θ and the signal vector ξ used in the adaptation: $-W=\theta^T\xi$. Hyperstability theory guarantees an asymptotically stable system if both the linear and nonlinear parts satisfy a positivity condition. A controllable, linear system with input u and output y:

$$\dot{x} = Ax + Bu$$
$$y = C^T x$$

with a transfer function :

$$H(s) = \frac{Y(s)}{U(s)} = C^T (sI - A)^{-1} B$$

is said to be *positive real* (PR) if Re[H(s)] equal or greater than zero. Hence the real part of the transfer function can never become negative as long as the real part of *s* is larger than or equal to zero. According to hyperstability theory the linear part H must be strictly positive real (SPR) which means that the real part of H(jw) is larger than zero for all W>0 thus Nyquist diagram of H(jw) must lie in the right half of the complex plane, including the imaginary axis. This implies that the number of poles and zeros in H(s) differs at most by 1, and the phase shift is never larger than 90^o.
The nonlinear part must satisfy Popov's integral inequality, which states that a positive constant γ_0^2 exists such that:

$$\int_0^{t_1} \varepsilon \bullet W \, dt \geq -\gamma_0^2 \quad \text{for all } t_1 \geq 0$$

This requirement is also denoted the passivity requirement. Observing nonlinear part as an electrical network, the inequality can be shown to state that the amount of energy output by the nonlinear system is never larger than the sum of the incoming energy and the energy stored in the system. The energy in the system depends on the external input of power and on the power generation in the system

$$\frac{d}{dt} \text{[stored energy]=[ext. power input] + [int. power generation]}$$

Considering ε, the input, as voltage and W as output, current, the external power input equals εW. If the internal power generation is negative, the system is said to

be dissipative or strictly passive. If the internal power generation is less than or equal to zero, the system is passive. Strict passivity is equivalent to SPR and asymptotic stability. The main result using positivity and passivity concepts is that any parallel combination of passive blocks is also passive. A feedback combination of two passive blocks in which at least one is strictly passive. This is of great interest in hyperstability theory, in which an SPR (and hence strictly passive) linear block is connected to a passive nonlinear block in a feed back configuration. This combination is strictly passive (and hence asymptotically stable).